



# UNIVERSIDAD DE GRANADA

TESIS DOCTORAL

**STATISTICAL NEUROIMAGE MODELING, PROCESSING  
AND SYNTHESIS BASED ON TEXTURE AND  
COMPONENT ANALYSIS: TACKLING THE SMALL  
SAMPLE SIZE PROBLEM.**

Presented by:  
**Francisco Jesús Martínez Murcia**

Advisors:  
**Juan Manuel Górriz Sáez**  
**Javier Ramírez Pérez de Inestrosa**

To apply for the:  
**International PhD Degree in Information and Communication  
Technologies.**

Junio 2017

Francisco Jesus Martinez Murcia

*Statistical Neuroimage Modeling, Processing and Synthesis based on Texture and Component Analysis: Tackling the Small Sample Size Problem.*

Copyright © 2017

## Titleback

This document was written with L<sup>A</sup>T<sub>E</sub>X on Linux using a modified ArsClassica, a reworking of the ClassicThesis style designed by André Miede, inspired to the masterpiece *The Elements of Typographic Style* by Robert Bringhurst.

## Contacts

 [fjesusmartinez@ugr.es](mailto:fjesusmartinez@ugr.es)

## ABSTRACT

The rise of neuroimaging in the last years has provided physicians and radiologist with the ability to study the brain with unprecedented ease. This led to a new biological perspective in the study of neurodegenerative diseases, allowing the characterization of different anatomical and functional patterns associated with them. Computer Aided Diagnostic (CAD) systems use statistical techniques for preparing, processing and extracting information from neuroimaging data pursuing a major goal: optimize the process of analysis and diagnosis of neurodegenerative diseases and mental conditions.

With this thesis we focus on three different stages of the CAD pipeline: pre-processing, feature extraction and validation. For preprocessing, we have developed a method that target a relatively recent concern: the confounding effect of false positives due to differences in the acquisition at multiple sites. Our method can effectively merge datasets while reducing the acquisition site effects. Regarding feature extraction, we have studied decomposition algorithms (independent component analysis, factor analysis), texture features and a complete framework called Spherical Brain Mapping, that reduces the 3-dimensional brain images to two-dimensional statistical maps. This allowed us to improve the performance of automatic systems for detecting Alzheimer's and Parkinson's diseases. Finally, we developed a brain simulation technique that can be used to validate new functional datasets as well as for educational purposes.

Guide:

<https://plg.uwaterloo.ca/~migod/research/beck00PSLA.html>

## RESUMEN

Resumen de la tesis en español.



## DECLARACIÓN

D. Juan Manuel Górriz Sáez, Doctor por la Universidad de Cádiz y la Universidad de Granada y Catedrático del Departamento de Teoría de la Señal, Telemática y Comunicaciones de la Universidad de Granada y

D. Javier Ramírez Pérez de Inestrosa, Doctor por la Universidad de Granada y Catedrático del Departamento de Teoría de la Señal, Telemática y Comunicaciones de la Universidad de Granada,

### MANIFIESTAN:

Que la presente Memoria titulada “Statistical Neuroimage Modeling, Processing and Synthesis based on Texture and Component Analysis: Tackling the Small Sample Size Problem. ”, presentada por Francisco Jesús Martínez Murcia para optar al grado de Doctor por la Universidad de Granada, ha sido realizada bajo nuestra dirección. Con esta fecha, autorizamos la presentación de la misma.

*Granada, Junio 2017*

Fdo: Juan Manuel Górriz Sáez

Fdo: Javier Ramírez Pérez de Inestrosa

Memoria presentada por Francisco Jesús Martínez Murcia para optar al Grado de Doctor por la Universidad de Granada.

---

Francisco Jesús Martínez Murcia



## DECLARACIÓN

El doctorando Francisco Jesús Martínez Murcia y los directores de la tesis Juan Manuel Górriz Sáez y Javier Ramírez Pérez de Inestrosa garantizamos, al firmar esta tesis doctoral, que el trabajo ha sido realizado por el doctorando bajo la dirección de los directores de la tesis y hasta donde nuestro conocimiento alcanza, en la realización del trabajo, se han respetado los derechos de otros autores a ser citados, cuando se han utilizado sus resultados o publicaciones.

*Granada, Junio 2017*

Directores de la Tesis:



Juan Manuel Górriz Sáez

Doctorando:



Francisco Jesús Martínez Murcia



Javier Ramírez Pérez de Inestrosa



## ACKNOWLEDGEMENTS

*We have seen that computer programming is an art,  
because it applies accumulated knowledge to the world,  
because it requires skill and ingenuity,  
and especially because it produces objects of beauty.*

— Donald Ervin Knuth

I wish first  
thank the members  
 $\text{\LaTeX}$  User Group, in partic-  
ular Claudio Beccari, Marco  
Brunero, Fabiano Busdraghi, Gustavo Cevolani, Rosaria  
D'Addazio, Massimiliano Dominici, Gloria Faccanoni, Daniele  
Ferone, Tommaso Gordini, Gianluca Gorni, Enrico Gregorio, Mau-  
rizio Himmelmann, Jerónimo Leal, Paride Legovini, Lapo Filippo  
Mori, Andrea Tonelli, Ivan Valbusa, Emiliano Giovanni Vavassori  
and Emanuele Vicentini, for their invaluable aid during the writ-  
ing of this work, the detailed explanations, the patience and the  
precision in the suggestions, the supplied solutions, the com-  
petence and the kindness: thank you, guys! Thanks also  
to all the people who have discussed with me on the  
forum of the Group, prodigal of precious observa-  
tions and good advices. Finally, thanks to An-  
dré Miede, for his wonderful ClassicThe-  
sis style, and to Daniel Gottschlag,  
who gave to me the hint  
for this original re-  
working.  
♡

Gracias también a todos los participantes en la encuesta del mapa de color.



# CONTENTS

1	Introduction	1
1	Introduction	3
1.1	Motivation	3
1.2	The Small Sample Size Problem	4
1.3	Aims and Objectives	5
1.4	Organization of this Thesis	6
1.5	Contributions	7
1.5.1	Articles	7
1.5.2	Conferences	8
1.5.3	Books	9
2	State of the Art	11
2.1	Introduction to Neuroimaging	11
2.1.1	Magnetic Resonance Imaging	11
2.1.2	Single Photon Emission Computed Tomography	13
2.1.3	Positron Emission Tomography	14
2.2	Medical Background	15
2.2.1	Alzheimer's Disease	15
2.2.2	Parkinsonism	16
2.2.3	Autism Spectrum Disorder	17
2.3	Voxelwise Analyses	17
2.3.1	Statistical Parametric Mapping	18
2.3.2	Voxel Based Morphometry	20
2.3.3	The Multiple Comparisons Problem	20
2.4	Machine Learning in Neuroimaging	23
2.4.1	Voxels as Features	24
2.4.2	Multivariate Analyses	24
3	General Methodology	27
3.1	Spatial Preprocessing	27
3.1.1	Spatial Normalization or Registration	28
3.1.2	Segmentation	31
3.2	Intensity Normalization	31
3.3	Evaluation Parameters and Methodology	33
3.3.1	Cross-validation	33
3.3.2	Classification Performance	35

II Reducing the Feature Space	37
4 Image Decomposition	39
4.1 Feature Selection	40
4.1.1 t-test	41
4.1.2 Kullback-Leibler Divergence	41
4.1.3 Mann-Whitney-Wilcoxon	41
4.2 Decomposition Algorithms	42
4.2.1 Factor Analysis	42
4.2.2 Independent Component Analysis	45
4.3 Results	47
4.3.1 Alzheimer's Disease	48
4.3.2 Parkinson's Disease	53
4.4 Discussion	61
5 Texture Features	67
5.1 Introduction	67
5.2 Methodology	68
5.2.1 Volume selection	68
5.2.2 Haralick Texture Analysis	69
5.2.3 Experiments	71
5.3 Results	72
5.3.1 Experiment 1	72
5.3.2 Experiment 2	76
5.4 Discussion	81
6 Spherical Brain Mapping	85
6.1 Introduction	85
6.2 Spherical Brain Mapping	86
6.2.1 Layered Extension	88
6.2.2 Volumetric Radial LBP	88
6.2.3 Anatomical Reference	91
6.3 Sampling Paths via Hidden Markov Models	93
6.3.1 Radial Texture Features	98
6.3.2 Experiments	99
6.4 Results	100
6.4.1 Experiment 1: Original and VRLBP Spherical Brain Mapping	100
6.4.2 Experiment 2: Layered Extension	104
6.4.3 Experiment 4: HMM on Synthetic Datasets	108
6.4.4 Experiment 5: Feature Selection using HMM Paths	109
6.4.5 Experiment 6: Texture SBM Maps based on HMM Paths	112

6.4.6	Classification Analysis	113
6.5	Discussion	113
6.5.1	Spherical Brain Mapping	113
6.5.2	Paths via Hidden Markov Model (HMM)	117
<b>III</b>	<b>Increasing the Sample Size</b>	<b>123</b>
7	Significance Weighted Principal Component Analysis	125
7.1	Significance Weighted Principal Component Analysis	126
7.1.1	Principal Component Analysis	126
7.1.2	One-Way Analysis of Variance	128
7.1.3	Weighting Function	128
7.2	Results for AIMS-MRI Dataset	130
7.2.1	Experiment 1: Effect of Acquisition Site	131
7.2.2	Experiment 2: Within-site Between-Group Differences	133
7.2.3	Experiment 3: Effect of SWPCA on Group Differences	133
7.2.4	Discussion	137
7.3	Results for DaTSCAN Datasets	143
8	Simulation of Functional Brain Images	145
8.1	Simulation Procedure	145
8.1.1	Decomposition via PCA	145
8.1.2	Probability Density Modelling using Kernel Density Estimation	145
8.1.3	Probability Density Modelling using Multivariate Gaussian	146
8.1.4	Random Number Generation	146
8.1.5	Brain Image Synthesis	146
8.2	Experimental Setup	146
8.3	Results for ADNI-PET Dataset	147
8.3.1	Experiment 1	147
8.4	Results for DaTSCAN Datasets	148
<b>IV</b>	<b>General Discussion and Conclusions</b>	<b>149</b>
9	General Discussion and Conclusions	151
9.1	General Discussion	151
9.1.1	Discussion on the algorithms	151
9.1.2	Discussion on the diseases	151
9.2	Conclusions	151
9.3	Future Work	151

v	Appendix	153
A	Datasets	155
A.1	Magnetic Resonance Imaging	155
A.1.1	ADNI-MRI, Alzheimer's Disease Neuroimaging Initiative	155
A.1.2	AIMS-MRI, MRC-AIMS Consortium	155
A.2	Positron Emission Tomography	157
A.2.1	ADNI-PET, Alzheimer's Disease Neuroimaging Initiative	157
A.3	Single Photon Emission Computed Tomography	158
A.3.1	VDLN-HMPAO, Virgen de las Nieves	158
A.3.2	VDLN-DAT, Virgen de las Nieves	158
A.3.3	VDLV-DAT, Virgen de la Victoria Hospital	159
A.3.4	PPMI-DAT, Parkinson's Progression Markers Initiative	160
B	Background on Support Vector Machines	161
	Bibliography	163

## LIST OF FIGURES

Figure 1.1	Illustration of one and two-dimensional spaces.	4
Figure 1.2	Structure of the thesis.	6
Figure 2.1	Example of T1 and T2-weighted MRI images.	12
Figure 2.2	Example of SPECT images.	14
Figure 2.3	Example of a PET-FDG image.	15
Figure 2.4	Example of a SPM analysis on a PET dataset.	19
Figure 2.5	Illustration of a typical neuroimaging CAD system.	23
Figure 2.6	Example of the cortical thickness of a subject.	25
Figure 3.1	Typical pre-processing pipeline in MRI	28
Figure 3.2	Comparison of the affine registration and the application of non-linear transformations to the images	30
Figure 3.3	Comparison between different types of intensity normalization.	33
Figure 3.4	Evolution of bias and variance in CV.	34
Figure 4.1	Illustration of how decomposition algorithms work.	39
Figure 4.2	Illustration of the system used in Chapter 4 .	40
Figure 4.3	Original PET image and its reconstruction using FA or ICA.	43
Figure 4.4	Variance of reconstruction error in Factor Analysis (FA).	44
Figure 4.5	Average performance of the AD datasets in FA.	49
Figure 4.6	Average performance of the AD datasets in ICA.	50
Figure 4.7	Performance at the operation point for the AD datasets, over the number of selected voxels.	51
Figure 4.8	Performance at the operation point for the AD datasets, over the number of components.	52
Figure 4.9	Average performance of the PKS datasets in FA.	55
Figure 4.10	Average performance of the PKS datasets in ICA.	56
Figure 4.11	Performance at the operation point for the PKS datasets, over the number of selected voxels.	58
Figure 4.12	Performance at the operation point for the PKS datasets, over the number of components.	59
Figure 4.13	Comparison between the different filtering methods in ADNI-PET.	61

Figure 4.14	Comparison between the different filtering methods in ADNI-PET.	63
Figure 4.15	Comparison between the different filtering methods in PPMI-DAT.	65
Figure 5.1	Schema of the proposed Texture-based CAD system.	67
Figure 5.2	Comparison of the different $I_{th}$ values.	69
Figure 5.3	Evolution of the average accuracy with the intensity threshold.	73
Figure 5.4	Violin plot of all accuracy values, grouped by database.	75
Figure 5.5	Accuracy obtained by averaging all accuracy values using a given volume selection threshold $I_{th}$ .	77
Figure 5.6	Average accuracy computed for each selection criteria over N in Experiment 2.	78
Figure 5.7	Distribution of the 100 first selected features by means of the different selection methods (using the $I_{th} = 0.35I_{max}$ ) for PPMI-DAT, VDNL-DAT, VDLV-DAT database.	82
Figure 6.1	Flow diagram of the procedure used in the textural analysis of projected MR brain images.	85
Figure 6.2	Illustration of the computation of the mapping vector $v_{\theta,\varphi}$ , the angles $\theta$ and $\varphi$ and the r-neighbourhood of $v$ (see Section 6.2.2).	86
Figure 6.3	Resulting GM and WM maps of the same control subject using the six proposed measures: Surface, Thickness, Number of Folds, Average, Entropy and Kurtosis.	89
Figure 6.4	Example of the layered approach using the average measure on GM maps.	90
Figure 6.5	Example of how the basic LBP is computed.	90
Figure 6.6	An example of the VRLBP projection for GM and WM Tissues.	92
Figure 6.7	SBM mapping of different cortical regions.	92
Figure 6.8	SBM mapping of some subcortical regions and organs.	93
Figure 6.9	Set of HMM based paths over the MRI DARTEL template.	97
Figure 6.10	SBM t-maps under the AD vs CTL for GM and WM images.	101
Figure 6.11	Maps that present the level of the t statistic in the Alzheimer's Disease (AD) vs. Control Subject (CTL) paradigm, for the VRLBP projections mapping over a) grey matter (GM) and b) white matter (WM).	102

Figure 6.12	Performance for the different Spherical Brain Mapping ( <b>SBM</b> ) approaches over the: a) Grey Matter and b) White Matter. <a href="#">105</a>
Figure 6.13	Performance of the four-layered mappings. <a href="#">106</a>
Figure 6.14	t-maps that present the level of statistical relevance in the AD vs. NC paradigm, for a four-layered average mapping over a) <b>GM</b> and b) <b>WM</b> . <a href="#">107</a>
Figure 6.15	Path traced over a gaussian mixture distribution of 4 isotropic gaussian kernels. <a href="#">108</a>
Figure 6.16	<b>HMM</b> path computed inside a density distribution defined by an helix. <a href="#">109</a>
Figure 6.17	Simulation of the <b>HMM</b> -based path tracing over an Iberian Peninsula height map, interconecting different cities. <a href="#">110</a>
Figure 6.18	DARTEL paths computed in each direction ( $\theta, \varphi$ ). Each path's colour represent the accuracy in a differential diagnosis. Only one in every five paths are shown for clarity purposes. <a href="#">111</a>
Figure 6.19	Performance at the operation point for the different mappings over the Grey Matter and White Matter, compared with the performance of Voxels As Features ( <b>VAF</b> ). <a href="#">114</a>
Figure 6.20	ROC curves of the different mappings for the <b>GM</b> and <b>WM</b> tissues. <a href="#">116</a>
Figure 6.21	Paths that obtain more than 75% accuracy, and a three-dimensional representation of the structures crossed by them. <a href="#">118</a>
Figure 7.1	Summary of the <b>SWPCA</b> algorithm, along with its context in the pipeline used in this article. <a href="#">127</a>
Figure 7.2	Weighting function $\Lambda_c(p_c, p_{th})$ used in <b>SWPCA</b> . <a href="#">129</a>
Figure 7.3	Box-plot of the distribution of the component scores at each site of the AIMS-MRI dataset (see Sections <a href="#">7.2</a> and <a href="#">A.1.2</a> ) in the four first components. <a href="#">129</a>
Figure 7.4	Brain t-map ( <b>VBM</b> ) of significant ( $p < 0.01,  t  > 2.57$ ) <b>GM</b> and <b>WM</b> between-group differences using <b>qT<sub>1</sub></b> , <b>qT<sub>2</sub></b> , <b>synT<sub>1</sub></b> , <b>GM</b> and <b>WM</b> modalities after applying <b>SWPCA</b> to remove site effects. <a href="#">132</a>
Figure 7.5	Brain t-map ( <b>VBM</b> ) of significant ( $p < 0.01,  t  > 2.57$ ) <b>GM</b> and <b>WM</b> differences in <b>ASD</b> using <b>qT<sub>1</sub></b> , <b>qT<sub>2</sub></b> , <b>synT<sub>1</sub></b> , <b>GM</b> and <b>WM</b> maps before and after applying <b>SWPCA</b> to remove site effects. <a href="#">136</a>

- Figure 7.6 Brain Z-map (**CBM**) of significant ( $p < 0.01$ ,  $|t| > 2.57$ ) **GM** and **WM** differences using **qT<sub>1</sub>**, **qT<sub>2</sub>**, **synT<sub>1</sub>**, **GM** and **WM** maps before and after applying **SWPCA** to remove site effects. **138**
- Figure 8.1 Schema of the brain image synthesis algorithm. **145**
- Figure 8.2 Comparison between simulated and original images from **AD** and **CTL** classes. **146**

## LIST OF TABLES

Table 3.1	Confusion matrix and its parts	<b>35</b>
Table 4.1	Performance values for the Alzheimer's datasets	<b>53</b>
Table 4.2	Performance values for the Parkinson's datasets	<b>60</b>
Table 4.3	Percentage of overlap between the selected areas by each method and the AAL atlas regions.	<b>62</b>
Table 5.1	Maximum scoring feature (single approach).	<b>74</b>
Table 5.2	Maximum scoring feature (cumulative approach).	<b>76</b>
Table 5.3	Best results of the experiment 2 per database, normalization and selection criteria.	<b>80</b>
Table 5.4	Comparison between our proposed system and other Parkinson's Disease ( <b>PD</b> ) diagnosis systems in the literature.	<b>84</b>
Table 6.1	Performance values (Average $\pm$ Standard Deviation) for the different <b>SBM</b> approaches.	<b>103</b>
Table 6.2	Performance values ( $\pm SD$ ) for the selected paths as features, and using t-test to select the voxels.	<b>111</b>
Table 6.3	Performance values ( $\pm SD$ ) for each of the measures used in the <b>SBM</b> article.	<b>112</b>
Table 6.4	Performance values ( $\pm SD$ ) for each of the 10 texture features.	<b>112</b>
Table 6.5	Performance values (Average $\pm$ Standard Deviation) for the Voxels as Features approach in both <b>GM</b> and <b>WM</b> tissues.	<b>113</b>
Table 6.6	Comparison between our algorithm performance values (best values for selected voxels in all paths and texture features) ( $\pm SD$ ) and other methods in the bibliography	<b>120</b>

Table 7.1	Between-site classification accuracy ( $\pm$ standard deviation) for different modalities and masks without and with <b>SWPCA</b> correction.	<a href="#">134</a>
Table 7.2	Classification accuracy (Acc), sensitivity (Sen) and specificity (Spec) $\pm$ standard deviation for each modality and mask using the participants acquired at the LON and CAM sites.	<a href="#">135</a>
Table 7.3	Classification accuracy (Acc), sensitivity (Sen), and specificity (Spec) $\pm$ STD for the different modalities and masks using ALL, before and after applying <b>SWPCA</b> .	<a href="#">139</a>
Table 7.4	Performance measures for the combined DaTSCAN dataset	<a href="#">143</a>
Table 8.1	Baseline performance of the set, using the original dataset.	<a href="#">147</a>
Table 8.2	Performance of Exp 1, demonstrating the predictive ability of the simulated images over the real dataset.	<a href="#">147</a>
Table 8.3	Performance of the Exp 3 proves the independence of the simulated images with respect to the originals.	<a href="#">148</a>
Table A.1	Summary of the datasets used in this thesis.	<a href="#">155</a>
Table A.2	Demographics of the AIMS-MRI dataset.	<a href="#">156</a>
Table A.3	Demographic details of the ADNI-PET dataset.	<a href="#">159</a>

## ACRONYMS

PCA	Principal Component Analysis
ICA	Independent Component Analysis
FA	Factor Analysis
SPECT	Single Photon Emission Computed Tomography
CT	Computed Tomography
PET	Positron Emission Tomography
AD	Alzheimer's Disease
PD	Parkinson's Disease
PKS	Parkinsonism

ASD	Autism Spectrum Disorder
MRI	Magnetic Resonance Imaging
fMRI	functional MRI
PLS	Partial Least Squares
SWPCA	Significance Weighted Principal Component Analysis
SBM	Spherical Brain Mapping
VBM	Voxel Based Morphometry
SPM	Statistical Parametric Mapping
SPM8	Statistical Parametric Mapping Software, version 8
CTL	Control Subject
VAF	Voxels As Features
CAD	Computer Aided Diagnosis
ADNI	Alzheimer's Disease Neuroimaging Initiative
PPMI	Parkinson's Progression Markers Initiative
VDLN	Virgen de las Nieves Hospital
VDLV	Virgen de la Victoria Hospital
MRC-AIMS	Medical Research Council Autism Imaging Multicentre Study
MNI	Montreal Neurological Institute
synT <sub>1</sub>	simulated T <sub>1</sub> - weighted Inversion Recovery
qT <sub>1</sub>	quantitative T <sub>1</sub> - weighted
qT <sub>2</sub>	quantitative T <sub>2</sub> - weighted
GM	grey matter
GLM	General Linear Model
WM	white matter
CSF	cerebro-spinal fluid

ANOVA	Analysis Of Variance
SVD	Singular Value Decomposition
SVM	Support Vector Machine
SVC	Support Vector Classifier
CBM	Component Based Morphometry
KDE	Kernel Density Estimation
MCI	Mild Cognitive Impairment
EM	Expectation-Maximization
PDF	Probability Density Function
FWE	Family Wise Error rate
RF	radiofrequency
SNR	Signal-To-Noise Ratio
rCBF	regional Cerebral Blood Flow
DAT	Dopamine Transporters
FBP	Filtered Back Projection
FDR	False Discovery Rate
ROI	Region of Interest
HMM	Hidden Markov Model
AC	Anterior Commissure
LBP	Local Binary Patterns
VRLBP	Volumetric Radial LBP
CV	Cross-validation
LOO	Leave-One-Out
TP	True Positive
FP	False Positive

TN	True Negative
FN	False Negative
KL	Kullback-Leibler
MWW	Mann-Whitney-Wilcoxon
EVD	eigen-value decomposition
SWEDD	subjects without evidence of dopaminergic deficit
GLCM	Grey Level Co-occurrence Matrix
RBF	Radial Basis Function

**Part I**

**INTRODUCTION**



# 1

## INTRODUCTION

### 1.1 Motivation

In recent years, there has been a rise in the use of neuroimaging in the clinical practice. It has improved and speeded the procedure of diagnostic, providing unprecedented insight into the brain. Neuroimaging is very extended in research as well. Different fields such as psychiatry, neurology, psychology, behavioural science or biology make extensive use of brain imaging in their studies.

The basis of these studies are common: a selection procedure by which a representative set of subjects is recruited, the fulfilment of an experiment on (or by) each subject and a statistical analysis of the acquired data. Particularly, when studying a certain disease, it is common to recruit subjects affected by the disease and non-affected, healthy subjects, usually known as **CTLs**. Then, in this typical example, both affected and **CTLs** are scanned, and brain anatomy or function is analysed using statistical tools. The result of this analysis is a list of significant differences between structure or function that could be linked to the disease.

Computer Aided Diagnosis (**CAD**) systems provide a set of tools to help setting up and performing these studies. It is currently a thriving area of research involving multidisciplinary teams, combining computer science, mathematics, medicine, artificial intelligence, statistics, machine learning, and many others [66]. The main aim is to assist clinicians in the procedure of diagnosis and study of the diseases by providing software that can effectively recognize disease patterns, characterize differences and make predictions.

One fundamental issue often found in this studies is the sample size. The number of subjects frequently ranges from tens to hundreds, whereas the number of features (namely voxels) to be analysed can add up to millions. This causes the so-called *Small Sample Size Problem* [26] which negatively affects the statistical power of any experiment performed using these datasets [12].

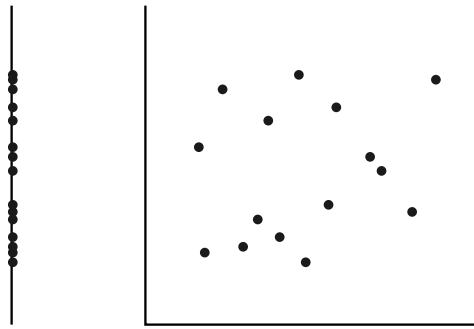


**Figure 1.1:** Illustration of the separation between points in one-dimensional and two-dimensional spaces.

## 1.2 The Small Sample Size Problem

The *Small Sample Size Problem* refers to a problem that arises when the proportion between number of subjects and number of features is large. Think of, e.g., 15 points in a one-dimensional line, as in Figure 1.1. If we think of a subject as a vector, we would have 15 subjects in a one-dimensional space. Now, imagine that we add a second dimension. It is easy to see that our subjects would be farther than in the two-dimensional world. And the same would happen if we move to four, ten or thousands of dimensions. The farther our points are, the more difficult it is for a statistical tool to extract information. That is what we call *almost empty spaces* [26, 97], in contrast to *dense spaces*, where points are closer.

Neuroimaging provides hundreds of thousands, or even millions of voxels, in what could mean millions of features. That implies that any calculation performed in those almost empty spaces will eventually lack information. This implies a loss of statistical power of the methods used, usually producing false negatives (the system is unable to detect real signal) and false positives (the system detects signal where there is not). These are known in statistics as Type I and Type II errors respectively.

In differential diagnosis studies, the small sample size problem leads to wrong conclusions about where real differences are located. This, in addition to untracked confounding variables are one of the fundamental sources of non-reproducibility in current neuroimaging studies [12].

The solution might seem straightforward: increase sample size. But this is not always possible, since neuroimaging studies do their best at recruiting as many people as they can with a limited budget. Many efforts have been put into

establishing multi-centre collaborations that allow the recruitment of a larger population, but despite offering a higher statistical power, these studies still suffer from a number of confounding variables such as population bias or scanner differences [38]. In Chapters 7 and 8 we explore different approaches to this solution.

Another option involves reducing the number of features, via feature selection or feature extraction. This has been widely used in computed-aided methodology for neuroimaging [xu2009source, 22, 36, 48, 66] with great success, and solutions using this approach will be treated in Chapters 4, 5 and 6.

The Small Sample Size problem is directly related to the *Curse of Dimensionality* [56], which proves that, in contrast to what could be expected, once a certain classifier performance has been achieved, it holds or even decreases when feeding more features to the classifier. The problem also affects statistical hypothesis testing, a tool widely used for inference in neuroimaging, in what is known as the *Multiple Comparisons* problem [8], a particular field that is still being studied.

## 1.3 Aims and Objectives

This thesis aims to contribute new approaches to overcome the small sample size problem in neuroimaging. This can provide more accurate CAD systems by reducing the number of false positives, increasing the reliability of their results.

We will take two different approaches, as commented in previous sections: increasing the sample size and reducing the feature space. Therefore, we can define the following objectives:

- Develop and evaluate algorithms that reduce the feature space, in which is usually known in the field as feature extraction and feature selection strategies.
- Develop and evaluate new strategies to increase the sample size in neuroimaging studies.

Most of the studies in the literature focus on the first objective. Feature extraction algorithms that use Principal Component Analysis (PCA) [52, 102] or Partial Least Squares [89], among others, are widely studied. We have developed three different approaches to those:

- A combination of image decomposition algorithms and feature selection. In this approach we have used three criteria to select the most significant voxels from the images, and then applied Factor Analysis (FA) and



**Figure 1.2:** Structure and connexions between the different strategies proposed in this thesis, organized by chapters and parts.

Independent Component Analysis ([ICA](#)) to decompose the data and significantly reduce their feature space.

- A feature extraction based on texture analysis.
- A novel strategy called Spherical Brain Mapping ([SBM](#)). This feature extraction technique uses a spherical coordinate system to map statistical measures to a bidimensional plane. It builds paths used as feature selection vectors where several measures are computed.

On the other hand, we have evaluated newer ways to increase sample size in neuroimaging studies. We have developed:

- A system to reduce undesired variance in structural multicentre studies, called Significance Weighted Principal Component Analysis ([SWPCA](#)). This system is intended to reduce the amount of false positives in large collaborations, providing more homogeneous images and improving their statistical analysis.
- An algorithm to simulate functional brain images using existing data, and therefore, increase sample size.

## 1.4 Organization of this Thesis

This thesis work is organized in four parts plus appendices, each of which is subdivided in several chapters. In the first part, we introduce the motivations

and main aims of this work (Chapter 1), examine the state of the art in medicine, neuroimaging and CAD systems (Chapter 2) and present a general methodology that will be followed throughout this thesis, including preprocessing and evaluation (Chapter 3).

Parts ii and iii refers to each of the solutions outlined in the previous section, and disaggregated in Figure 1.2. In part ii we focus on the feature reduction techniques, including decomposition methods (Chapter 4), texture analysis (Chapter 5), and the novel algorithm Spherical Brain Mapping (Chapter 6). On the other hand, Part iii is focused on two different strategies used to increase the sample size: the Significance Weighted Principal Component Analysis algorithm (Chapter 7), used to safely merge structural images acquired at different centres, and a neuroimage simulation algorithm (Chapter 8) that can be used to extend existing functional datasets.

Finally, in Part iv we provide a general discussion of the results presented in this thesis, conclusions about the methods and prospective work that could be performed with this basis.

## 1.5 Contributions

Some ideas and figures have appeared previously in the following publications, that we divide here in articles and conference presentations.

### 1.5.1 Articles

F.J. Martínez-Murcia et al. "On the Brain Structure Heterogeneity of Autism: Parsing out Acquisition Site Effects With Significance-Weighted Principal Component Analysis". In: *Human Brain Mapping* 38.3 (Mar. 2017), pp. 1208–1223.  
DOI: [10.1002/hbm.23449](https://doi.org/10.1002/hbm.23449).

F.J. Martinez-Murcia, J.M. Górriz, J. Ramírez, and A. Ortiz. "A Spherical Brain Mapping of MR Images for the Detection of Alzheimer's Disease". In: *Current Alzheimer Research* 13.5 (Mar. 2016), pp. 575–588.  
DOI: [10.2174/1567205013666160314145158](https://doi.org/10.2174/1567205013666160314145158).

F.J. Martinez-Murcia, J.M. Górriz, J. Ramírez, and A. Ortiz. "A Structural Parametrization of the Brain Using Hidden Markov Models-Based Paths in Alzheimer's Disease". In: *International Journal of Neural Systems* 26.7 (Nov. 2016), p. 1650024.  
DOI: [10.1142/S0129065716500246](https://doi.org/10.1142/S0129065716500246).

F.J. Martínez-Murcia, J.M. Górriz, J. Ramírez, I.A. Illán, and A. Ortiz. "Automatic detection of Parkinsonism using significance measures and component analysis in DaTSCAN imaging". In: *Neurocomputing* 126 (Feb. 2014), pp. 58–70.  
 DOI: [10.1016/j.neucom.2013.01.054](https://doi.org/10.1016/j.neucom.2013.01.054).

F.J. Martínez-Murcia, J.M. Górriz, J. Ramírez, M. Moreno-Caballero, and M. Gómez-Río. "Parametrization of textural patterns in  $^{123}\text{I}$ -ioflupane imaging for the automatic detection of Parkinsonism". In: *Medical Physics* 41.1 (2014), p. 012502.  
 DOI: [10.1118/1.4845115](https://doi.org/10.1118/1.4845115).

F.J. Martínez-Murcia, J.M. Górriz, J. Ramírez, C.G. Puntonet, and I.A. Illán. "Functional activity maps based on significance measures and Independent Component Analysis". In: *Computer Methods and Programs in Biomedicine* 111.1 (July 2013), pp. 255–268.

DOI: [10.1016/j.cmpb.2013.03.015](https://doi.org/10.1016/j.cmpb.2013.03.015).

F.J. Martínez-Murcia, J.M. Górriz, J. Ramírez, C.G. Puntonet, and D. Salas-González. "Computer Aided Diagnosis tool for Alzheimer's Disease based on Mann-Whitney-Wilcoxon U-Test". In: *Expert Systems with Applications* 39.10 (Aug. 2012), pp. 9676–9685.

DOI: [10.1016/j.eswa.2012.02.153](https://doi.org/10.1016/j.eswa.2012.02.153).

### 1.5.2 Conferences

F.J. Martínez-Murcia, A. Ortiz, J. Manuel Górriz, J. Ramírez, and I.A. Illán. "A volumetric radial LBP projection of MRI brain images for the diagnosis of alzheimer's disease". In: *Artificial Computation in Biology and Medicine*. Vol. 9107. Springer Science + Business Media, 2015, pp. 19–28.

DOI: [10.1007/978-3-319-18914-7\\_3](https://doi.org/10.1007/978-3-319-18914-7_3).

F.J. Martínez-Murcia, J.M. Górriz, J. Ramírez, I. Álvarez Illán, D. Salas-González, and F. Segovia. "Projecting MRI brain images for the detection of Alzheimer's Disease". In: *Studies in Health Technology and Informatics*. Vol. 207. 2014, pp. 225–233.

DOI: [10.3233/978-1-61499-474-9-225](https://doi.org/10.3233/978-1-61499-474-9-225).

F.J. Martínez-Murcia, J.M. Górriz, J. Ramírez, I.A. Illán, and C.G. Puntonet. "Texture Features Based Detection of Parkinson's Disease on DaTSCAN Images". In: *Natural and Artificial Computation in Engineering and Medical Applications*. Vol. 7931 LNCS. PART 2. Springer Science + Business Media, 2013, pp. 266–277.

DOI: [10.1007/978-3-642-38622-0\\_28](https://doi.org/10.1007/978-3-642-38622-0_28).

F.J. Martínez, D. Salas-González, J.M. Górriz, J. Ramírez, C.G. Puntonet, and M. Gómez-Río. "Analysis of Spect Brain Images Using Wilcoxon and Relative Entropy Criteria and Quadratic Multivariate Classifiers for the Diagnosis of Alzheimer's Disease". In: *New Challenges on Bioinspired Applications*. Vol. 6687. Lecture Notes in Computer Science PART 2. Springer Science + Business Media, 2011, pp. 41–48.

DOI: [10.1007/978-3-642-21326-7\\_5](https://doi.org/10.1007/978-3-642-21326-7_5).

### 1.5.3 Books

F.J. Martinez-Murcia, J. Górriz, and J. Ramírez. "Computer Aided Diagnosis in Neuroimaging". In: *Computer-aided Technologies - Applications in Engineering and Medicine*. Ed. by Razvan Udroiu. 1st ed. Intech, Dec. 2016. Chap. 7, pp. 137–160. ISBN: 978-953-51-4895-1.

DOI: [10.5772/64980](https://doi.org/10.5772/64980).

F.J. Martinez-Murcia, J.M. Górriz, and J. Ramírez. "Feature Extraction". In: *Wiley Encyclopedia of Electrical and Electronics Engineering*. Wiley, 2016, Accepted.

DOI: [10.1002/047134608X](https://doi.org/10.1002/047134608X).



# 2 | STATE OF THE ART

We have already stated the motivation and objectives of this thesis. Now, we will describe in detail some of the more relevant issues for the state of the art. First, in Section 2.1, we will make an introduction to the different neuroimaging modalities used in our experiments. Afterwards, we will provide some insights into the neurological and psychiatric disorders treated here in Section 2.2 or the most extended voxel-wise analyses used in the neuroimaging community at Section 2.3. Finally, at Section 2.4 we will explore recent contributions to the field that use Machine Learning.

## 2.1 Introduction to Neuroimaging

Medical imaging refers to all types of 2D, 3D and 4D images used in clinical practice. These involve many different modalities, among them X-rays, ultrasound, endoscopy, microscopy, etc. In neuroimaging, the most extended is by far Magnetic Resonance Imaging ([MRI](#)), which provides intensity maps that represent the internal structure of the brain. Other modalities are aimed at studying the function of the brain, by injecting radioactive ligands that, linked to a receptor, can measure its distribution. This is the case of Positron Emission Tomography ([PET](#)) and Single Photon Emission Computed Tomography ([SPECT](#)).

### 2.1.1 Magnetic Resonance Imaging

Magnetic Resonance Imaging ([MRI](#)) is perhaps the most widespread in neuroimaging, given its ability to visualize both structural and functional (in functional [MRI](#)) properties of the brain, and, in contrast to other imaging modalities, is considered non-invasive. [MRI](#) uses strong magnetic fields to excite certain atomic nuclei, that can absorb and emit this energy.

[MRI](#) combines the magnetic field with a radiofrequency ([RF](#)) emission to excite the atomic nuclei present in corporal structure, resulting in a image of the distribution of certain atoms in the body. Most [MRI](#) use hydrogen atoms, since they are present in water (which adds up to around 70% of body mass) and

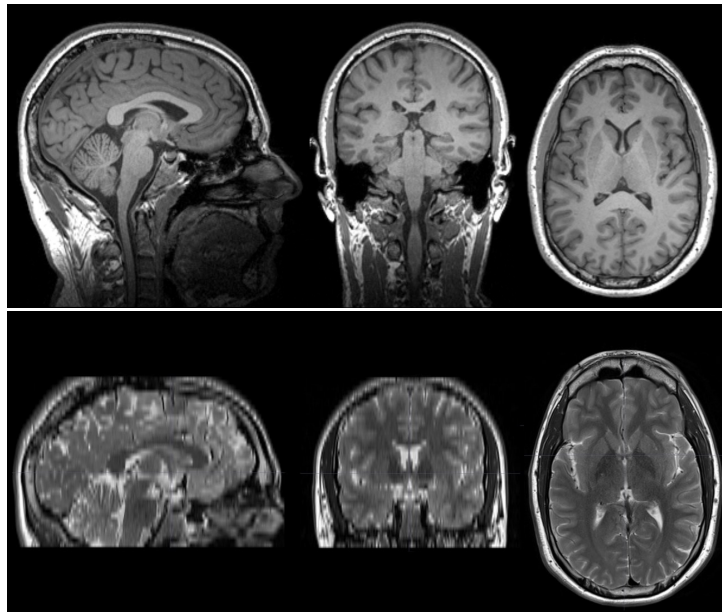


**Figure 2.1:** Example of T1 and T2-weighted MRI images of the same subject (me).

the signal derived is stronger than other atoms, increasing the Signal-To-Noise Ratio ([SNR](#)), and therefore, the image quality.

The procedure uses a strong magnetic field  $B_0$  to align the magnetic moment of the hydrogen nuclei in parallel or anti-parallel (depending of their initial spin). This way, the magnetic moment of all nuclei will increase up to a stable state, in contrast to their null value in absence of  $B_0$ . Within this magnetic field, the hydrogen atoms precess around an axis along the direction of the field.

A given nuclei has a resonance frequency which is proportional to the intensity of  $B_0$ , which, by using strong fields, allow us to resonate hydrogen far below potentially damaging frequencies. The precession frequency is determined by the Larmor equation (2.1):

$$f_0 = \frac{\gamma}{2\pi} B_0 \quad (2.1)$$

where  $\gamma$  depends on the nuclei, which in the case of hydrogen,  $\gamma = 42.6 \text{ MHz/T}$ . When a subject is introduced in the [MRI](#) scanner, it is submitted to the magnetic field  $B_0$ , so that the hydrogen nuclei are aligned to the field, with a precession frequency  $f_0$ . Then, a [RF](#) pulse of the same frequency is generated, which is then absorbed by the nuclei, forcing them to place perpendicular to the field. Once the [RF](#) emission is interrupted, the nuclei return to its equilibrium state by means of a procedure called relaxation. In this procedure, they emit part of

the absorbed energy, which is then captured by a RF receptor. Usually, position information is encoded in the RF signal by varying  $B_0$  using gradient coils.

The RF signal is measured during the relaxation time, and two different relaxation times are set: the T<sub>1</sub> (spin-lattice) relaxation time and the T<sub>2</sub> (spin-spin) relaxation time. The T<sub>1</sub> time is the time during which nuclei emit energy to the adjacent tissue and realign to the longitudinal plane (z axis), whereas the T<sub>2</sub> time refers to the time when nuclei realign to the transversal plane (y axis). These times are used to create T<sub>1</sub>-weighted and T<sub>2</sub>-weighted images (see Figure 2.1). T<sub>1</sub>-weighted images allow to distinguish between GM and WM in the cerebral cortex, to identify fatty tissue, and generally, obtain structural information. Conversely, T<sub>2</sub>-weighted images are used to assess cerebro-spinal fluid (CSF) or to visualize and identify WM lesions.

### 2.1.2 Single Photon Emission Computed Tomography

The Single Photon Emission Computed Tomography (SPECT) is based on the principles of Computed Tomography (CT), by which a series of signal acquisition at different angles can be reconstructed back into a bidimensional distribution of the signal. In SPECT, a gamma photon emitting radioisotope is linked to a pharmaceutical that binds to a given biomarker, generating a radiopharmaceutical or agent. This agent is injected into the patient, and after a certain time in which the radiopharmaceutical is distributed, the patient is introduced into the SPECT-CT scan.

Afterwards, the scanner performs a series of acquisitions at different planes and angles from the body, from which the gamma signal is measured. For each plane, all acquisitions at each angle are pooled and a single two-dimensional image is reconstructed using a Filtered Back Projection (FBP) algorithm, or Radon inversion formula [46], which derives from the Fourier's Theorem. A total of 180 projections per plane, using an angular resolution of 2 degrees, are usually taken.

There exist a number of radiopharmaceutical used in clinical practice, and therefore, we will focus on the two varieties used in this thesis. First, we use an agent called <sup>99m</sup>Tc-HMPAO, which consists of two stereoisomers of hexametazime (HMPAO) linked to the radioisotope technetium 99-metastable. This agent is usually used to assess regional Cerebral Blood Flow (rCBF), which can be used to diagnose neurological diseases or cancer.

Additionally, we use images generated using the agent Ioflupane (<sup>123</sup>I), a cocaine analog with high binding affinity for Dopamine Transporters (DAT). It is



**Figure 2.2:** Example of [SPECT](#) images, a SPECT-HMPAO and a SPECT-DaTSCAN.

used fundamentally in the assessment of [PD](#), given that the disease is associated with a loss of dopaminergic neurons in the striatal region.

### 2.1.3 Positron Emission Tomography

The Positron Emission Tomography ([PET](#)) is a technique similar to [SPECT](#), but in this case, the agent used and the equipment is designed to deal with a pair of gamma photons resulting of the annihilation of a positron with its corresponding antiparticle, the electron. The pair of photons are generated in opposite directions, and the detection depends on them being simultaneously or coincidently detected at the receptor. The receptor comprises a scintillator which emits light when the gamma photon incides, and a detector, usually a photomultiplier tube or silicon avalanche photodiodes.

It uses the same [FBP](#) algorithm as [SPECT](#) in the reconstruction of the images, and a similar strategy for acquiring the signal at different angles. However, the amount of data is smaller than in [SPECT](#), and therefore, the reconstruction procedure is harder. As a result, [PET](#) scanner operation is considered more costly than [SPECT](#) [3].

The agent used in the images that we have processed is PET-FDG, also known as Fludeoxyglucose ( $^{18}\text{F}$ ). It is a glucose analogue that allows us to measure the glucose metabolism in the brain. It is widely used in neurology [79] and cancer detection [66], since it can be correlated with cellular activity.

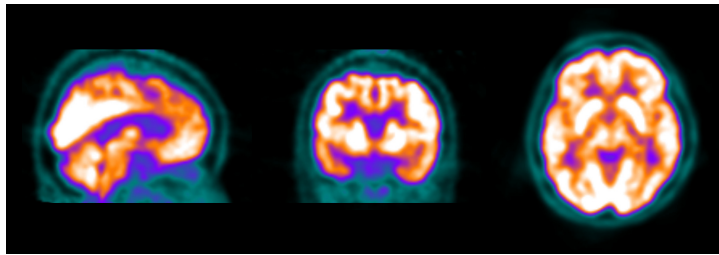


**Figure 2.3:** Example of a PET-FDG image.

## 2.2 Medical Background

### 2.2.1 Alzheimer's Disease

Alzheimer's Disease ([AD](#)) is the most common cause of dementia in the world, with more than 46 million people affected, and it is likely to increase up to 135.5 million by 2050 [[2](#)]. Its causes are still not clear, but it is characterized by deposits of high amounts of structures such as Amyloid- $\beta$  ( $A\beta$ ) plaques or neurofibrillary tangles accompanied by synaptic dysfunction and neurodegeneration that eventually lead to cell death [[9](#), [34](#)].

Diagnosis of [AD](#) is often based on the clinical history of the patient, using cognitive tests along with medical imaging and blood tests. A definite diagnosis can only be addressed post-mortem, via a direct examination of the brain tissue [[34](#)]. Cognitive tests such as *Mini Mental State Exam* or *Clinical Dementia Ratio* are widely used in clinical practice.

Initial symptoms of [AD](#) are often mistaken for normal ageing, leading to a state known as Mild Cognitive Impairment ([MCI](#)). Not all [MCI](#)-affected subjects develop [AD](#). In fact, the prediction of [MCI](#) conversion is the most urging challenge in [AD](#) research, since an early diagnosis can lead to an improvement in life expectancy and quality of life of the patients.

[MRI](#) brain images have been extensively used in the diagnosis of [AD](#) by assessing neurodegeneration on [GM](#) and [WM](#) tissues. Research has shown in [[24](#), [47](#), [57](#), [82](#)] that neurodegeneration in Alzheimer's Disease mainly occurs in the [GM](#) tissue. Particularly grey matter loss has been described in the Hippocampus and Parahippocampal lobes, according to the NINCDS-ADRDA criteria for AD diagnosis [[57](#)], with further atrophy described in the medial temporal structures, the Posterior Cingulate gyrus and adjacent Precuneus [[82](#)]. Moreover, significantly lower volumes of certain regions in [GM](#) and [WM](#) have been considered a promising biomarker and predictor of the progression of [AD](#) in a longitudinal study involving [MCI](#) patients [[47](#)], and some structures in the striatum (putamen and

caudate nucleus) have shown important volume abnormalities [24]. All these data suggest that many of the symptoms of AD can be observed in anatomical MRI images even in early stages of the disease, which could be of great help in its successful diagnosis and treatment.

Nuclear imaging, such as PET or SPECT, have also been used in clinical practice, especially to discard other diseases. In typical PET-FDG or SPECT-HMPAO, AD is characterized by reduced brain activity in bilateral regions, such as the posterior cingulate gyri and precunei, as well as the temporo-parietal region [103]. It also affects the frontal cortex and the whole brain in severe cases [89, 107].

Recently, new more specific radiopharmaceuticals have been developed, among them the Pittsburgh compound B (PiB). This drug binds to fibrillar A $\beta$  allowing *in vivo* visualization of A $\beta$  plaques in the brain [52]. However, due to their technical requirements -a relatively small half-life of the radioactive element-, they are unusual in clinical practice.

## 2.2.2 Parkinsonism

Parkinsonism (PKS) or Parkinsonian Syndrome is the second most common neurodegenerative disease in the world, with a prevalence of 1-3% in the elder population (over 65 years)[58]. It is characterized by hypokinesia, rigidity, tremor and postural instability [58]. It is not a single disease itself, but a wide range of conditions that share similar symptoms. The most common cause of PKS is Parkinson's Disease (PD), but other possible causes include toxins, a few metabolic diseases, and other extrapyramidal syndromes such as Multiple System Atrophy, Progressive Supranuclear Palsy or Cortico-Basal Degeneration [55, 68].

### 2.2.2.1 Parkinson's Disease

The etiology of Parkinson's Disease (PD) involves the progressive loss of Dopamine Transporters (DAT) of the nigrostriatal pathway. This causes a decrease in the dopamine content of the striatum, since the pathway connects the substantia nigra to the striatum.

In PD, structural imaging such as MRI has limited value, since structural abnormalities can be seen only in the latter stages. Nevertheless, in molecular imaging, a number of radiopharmaceuticals have been proposed to assess the levels of pre and post-synaptic DAT at the striatum. Among them, the  $^{123}\text{I}$ -ioflupane (better known by its tradename DaTSCAN) is perhaps the most popular. DaTSCAN binds to the DAT at the striatum [58, 61, 76], allowing the estimation of DAT density by means of a SPECT scanner. In DaTSCAN images, a

reduced uptake at the striatum is a clear indication of DAT loss, and therefore, of PD [61].

### 2.2.2.2 *Extrapyramidal Syndroms*

Among the extrapyramidal syndroms of PKS, the most relevant diagnoses are Multiple System Atrophy, Progressive Supranuclear Palsy and Cortico-Basal Degeneration [55]. An accurate diagnosis can positively impact in the health of these patients, avoiding wrong treatment decisions.

Structural imaging, as in the previous case, has little value here. To establish a differential diagnosis with PD, different drugs have been proposed. DaTSCAN is widely used to assess pre-synaptic dopaminergic loss, but in a post-synaptic level, one of the most extended is <sup>18</sup>F-DMFP-PET [8]. However, in this thesis we have focused only on the pre-synaptic level, and therefore, in the diagnosis of PD.

### 2.2.3 Autism Spectrum Disorder

Autism Spectrum Disorder (ASD) is a neurodevelopmental syndrome characterized by social and communication impairment as well as restricted, repetitive patterns of behaviour, interests or activities. Its origins are still unknown, although research suggest [93] that there exist genetic risk factors.

The evidence of either functionally or structurally affected areas in the brain is a major concern [14, 15]. In the latter years, many strategies have been explored to recruit large samples in order to detect significant differences between affected and non-affected subjects. This has been addressed by initiatives such as the Medical Research Council Autism Imaging Multicentre Study (MRC-AIMS) [21, 29] or the Autism Brain Imaging Data Exchange (ABIDE) [13].

## 2.3 Voxelwise Analyses

Traditional analysis of neuroimaging involves visual analysis by experts clinicians, or semi-quantitative analysis of Regions of Interest (ROIs). With the rise of neuroimaging in the mid-nineties, some computer-aided solutions appeared, of which the most extended are the widely known Statistical Parametric Mapping (SPM) [104] and its extension to structural imaging Voxel Based Morphometry (VBM) [86].

### 2.3.1 Statistical Parametric Mapping

Statistical Parametric Mapping ([SPM](#)) is a new methodology to automatically examine differences in brain activity in functional imaging studies involving functional [MRI](#) ([fMRI](#)) or [PET](#), firstly proposed by Friston in [104]. The technique can be applied either to static images (e.g., [PET](#)) or timeseries ([fMRI](#)), using inference techniques based on hypothesis testing, in order to construct the General Linear Model ([GLM](#)) that better describes the variability in the data.

Statistical hypothesis testing involves constructing a pair of hypotheses:  $H_0$ , or the null hypothesis, that states no relationship between variables; and  $H_1$ , the alternative hypothesis. In neuroimaging,  $H_0$  usually means that there are no relevant differences between classes (for example, between patients affected by Alzheimer's Disease ([AD](#)) and [CTL](#)), and  $H_1$  implies that there is a significant difference. Many different tests such as massive univariate t-Test or Analysis Of Variance ([ANOVA](#)) (see Chapter 4 for more information on these techniques) can be used in the [SPM](#) software [59], by using a design matrix that describes a t or F based contrast (for t-Test and [ANOVA](#) respectively). These terms are generally referred to as Z-values, namely the signed number of standard deviations an observation is above the mean.

The test are computed voxel-wise, from which a p-value can be obtained, nominally the probability of obtaining equally or more extreme Z values than the one actually found. p-values are very extended in neuroimaging, representing the probability of a Z value being equal or more extreme than the reference value given. In many studies  $p < 0.05$  is used for measuring statistical significance, which means that only a 5% of the times a experiment is repeated we would obtain that result or a more extreme one. The use of the significance threshold  $\alpha = 0.05$  implies that any voxel with a p-value smaller than 0.05 is considered sufficient to reject the null hypothesis.

[SPM](#) outputs maps like the one shown in Figure 2.4. There, significant Z-values according to a given threshold ([FWE](#) uncorrected or corrected, see Section 2.3.3) are displayed over an anatomical reference. The resulting maps allow a visual inspection of the active brain areas, which can later be related to a certain disease or task.

Although [SPM](#)'s main feature is the estimation of differences, the term has been extended to cover the whole process performed by the [SPM](#) software. That is, it generally involves registration to a template, intensity normalization, smoothing, the proper [SPM](#) difference estimation and the display of the results. An overview of these procedures is provided at Chapter 3.

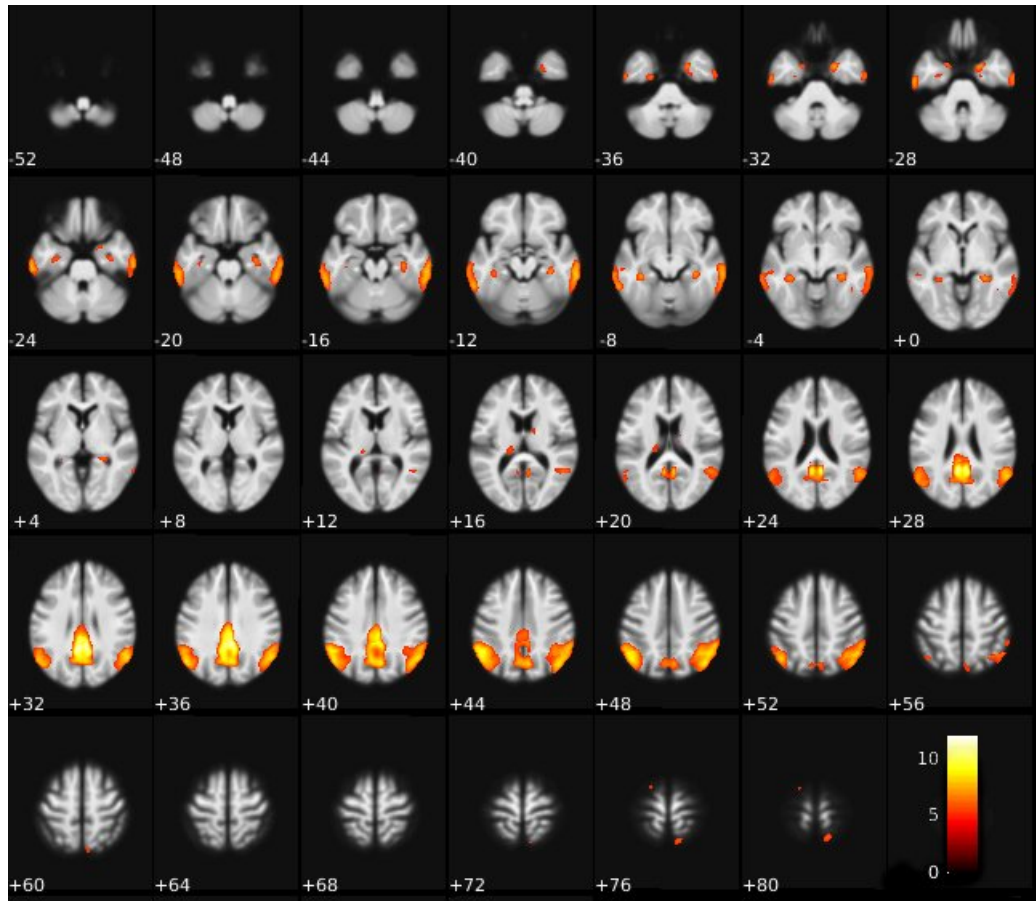


**Figure 2.4:** Example of a SPM analysis on a PET dataset displaying the differences between AD and CTL, using  $p < 0.05$  and FWE correction.

### 2.3.2 Voxel Based Morphometry

Voxel Based Morphometry ([VBM](#)) can be considered an extention of [SPM](#) applied to structural [MRI](#) images [86]. The procedure involves preprocessing (see Chapter 3), where smoothing is applied to reduce smaller anatomical differences. Afterwards, a [GLM](#) is applied to each voxel in the images, and a Z-score map similar to Figure 2.4 is produced.

Smoothing is more important in [VBM](#) than in regular [SPM](#), since [MRI](#) images have higher resolution and are less noisy than functional images. Larger smoothing kernels will miss out smaller regions, while smaller kernel can lead to artifacts in the generated Z-maps, including misalignment of brain structures, differences in folding patterns or misclassification of tissue types [4]. Therefore, the kernel size must be carefully chosen, usually using a-priori knowledge about the regions affected, and always double checking for artifacts and reproducibility.

The idea behind [VBM](#) has been extended in a number of papers, using multivariate approaches that takes into account all voxels at once, and not their individual differences. Some of them include [ICA](#) decomposition of the dataset and a posterior conversion to Z-scores in what was called Source Based Morphometry [[xu2009source](#)], or multidimensional Tensor Based Morphometry [[41](#)].

### 2.3.3 The Multiple Comparisons Problem

The Multiple Comparisons problem arises when using hypothesis testing to assess statistical significance. This is widely used in neuroimaging, where statistical tests such as the t-Test or [ANOVA](#) are used to quantify voxel-wise differences, and state their statistical significance, or p-value. The p-value, as described above, is the probability of any value being more extreme than a certain threshold under a given hypothesis. In our problem, given the t-value  $T_i$  for the  $i^{\text{th}}$  voxel ( $i = 1, \dots, N$ ) of the images, and a threshold  $T_{\text{th}}$  under the hypothesis  $H$ , the significance can be assessed by checking:

$$P(T_i > T_{\text{th}} | H_0) < \alpha \quad (2.2)$$

where  $\alpha$  is the significance level.

Choosing  $\alpha$  is not trivial in neuroimaging. The use of the significance level  $\alpha = 0.05$  implies that any voxel with a p-value smaller than 0.05 is considered sufficient to reject the null hypothesis. This does not directly imply the necessity of accepting the alternative hypothesis  $H_1$ , although it is often thought so. Neither it yields the probability of the null hypothesis [73].

If we apply  $p < 0.05$  directly to a medical image of, for example, 300,000 voxels, that could mean the possibility of almost 15,000 voxels being false positives.

Controlling the apparition of false positives when applying a massive univariate test is not trivial. It implies a balance between the true positive rate (sensitivity) or true negative rate (specificity), given that, for example, controlling the amount of false negatives will result in many false positives and vice-versa.

Usually, two options for controlling the amount of false positives are given: the Family Wise Error rate ([FWE](#)) and the False Discovery Rate ([FDR](#)). The [FWE](#) is the probability of obtaining at least one type I error. Mathematically, the null hypothesis for the  $i^{\text{th}}$  voxel  $H_{0i}$  states that there is no activation in that voxel. Therefore, the family-wise null hypothesis for our problem is:

$$H_0 = \bigcap_i H_{0i} \quad (2.3)$$

If we reject a single null hypothesis ( $T_i > T_{\text{th}}$ ), we reject  $H_0$ . Therefore, we want to control the probability of a single voxel being significant if the family-wise null hypothesis is valid:

$$P \left( \bigcup_i \{T_i > T_{\text{th}}\} | H_0 \right) < \alpha \quad (2.4)$$

In this case, we must obtain the critical value  $T_{\text{th}}$ , which is the higher t value that matches that expression. Many options have been proposed to this problem, among them the conservative Bonferroni correction, methods that use random field theory or permutation tests.

### 2.3.3.1 *The Bonferroni Correction*

The Bonferroni correction [[102](#)] rewrites eq. [2.2](#) setting  $\alpha = \frac{\alpha}{N}$  so that:

$$P(T_i > T_{\text{th}} | H_0) < \frac{\alpha}{N} \quad (2.5)$$

That way, using the Boole's inequality:

$$\text{FWE} \leq \sum_i \frac{\alpha}{N} = \alpha \quad (2.6)$$

Therefore, we can comply with the imposed restriction for a maximum [FWE](#), or in our case, a maximum rate  $\alpha$  of false positives. This is considered a rather conservative approach. In the example cited above, if we want to keep the [FWE](#) below 0.05, we should divide it by  $N$ , therefore obtaining a  $T_{\text{th}}$  that makes  $\alpha = 0.05/N = 1.67 \times 10^{-7}$ .

Other less conservative options try to compute a critical value  $T_{th}$  that minimizes the [FWE](#) using spatial information. This is the case of using an approximation of the distribution of the maximum statistic over the image, or the spatial correlation, including elements from random field theory (the approach used in [SPM](#) [59]).

### 2.3.3.2 Random Field Theory

In the random field approach, the maps of the statistic are treated, under the null hypothesis, as a lattice representation of smooth isotropic three dimensional random fields of test statistics. This approximation to the problem allow us to approximate the upper tail of the maximum distribution, the part needed for defining an event that occurs when the map exceeds the critical value  $T_{th}$ . Further information about random field theory and how it is applied to neuroimaging can be found at [59].

The other approach, based on the [FDR](#), aims at controlling the proportion of false positives in the total number of voxels declared significant. The most extended procedure for controlling the [FDR](#) is that proposed by Benjamini and Hochberg [100]. The Benjamini and Hochberg method start with calculating the p-values of all voxels and ranking them so that:

$$p_1 \leq p_2 \leq \dots \leq p_i \leq \dots \leq p_N \quad \forall i = 1 \dots N \quad (2.7)$$

### 2.3.3.3 FDR Controlling Procedures

Let  $q$  be the a maximum [FDR](#) value that we can afford, for example 0.05. For each  $i$ , we compute:

$$p_i \leq \frac{i}{N} q \quad (2.8)$$

The maximum  $i$  value that holds Eq. 2.8 is used as  $\alpha$ , the significance level, and its corresponding statistical value ( $T_i$  in the case of a t-test) is used as the critical value. This test, under the family-wise null hypothesis  $H_0$ , is equivalent to controlling the [FWE](#). However, [FDR](#) methods are less conservative than other approaches such as the Bonferroni or other [FWE](#)-based corrections, leading to a gain in statistical power.

### 2.3.3.4 Permutation Tests

An empirical way to obtain p-values without relying on any parametric assumption is permutation testing [19, 81]. Permutation tests evaluate a statistic such as the F-statistic or the t-test using randomly target variables, in our case, the classes. The procedure is applied many times (up to 10,000), and for each

permutation, only the maximum value of the computed statistic is considered. These values are used to build the null distribution, from which the family-wise corrected p-values are computed. Results obtained in permutation tests are comparable to those obtained using Random Field Theory [19], and far less conservative than when applying the Bonferroni correction.

## 2.4 Machine Learning in Neuroimaging

Machine learning is a current trend in neuroimaging. It provides computers with the ability to learn from data, using a set of statistical and computational tools. Rather than being explicitly programmed for a certain task, machine learning systems are able to find relevant data, discover patterns and predict the outcome of the input data. Its application to medicine is often known as Computer Aided Diagnosis ([CAD](#)) [7].

There are two major branches of machine learning: supervised and unsupervised learning. Th former explores the patterns that lead to a certain outcome, whereas on the other hand, unsupervised learning explores the underlying structure of the data. Most of the [CAD](#) systems rely on supervised learning, since their intention is to discover patterns that can effectively predict a disease.

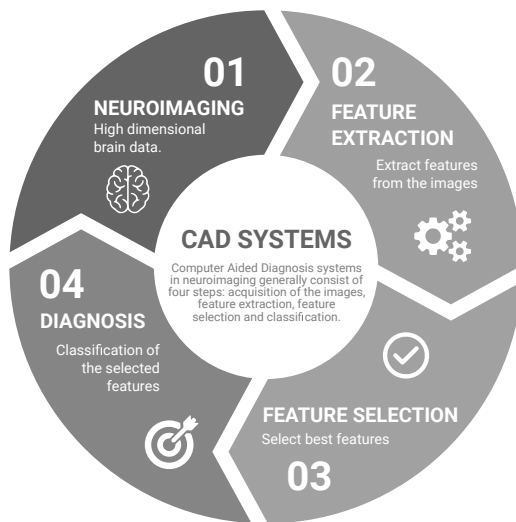


**Figure 2.5:** Illustration of a typical neuroimaging [CAD](#) system.

For simplicity, in this thesis, when talking about [CAD](#), we will always refer to automatic [CAD](#) systems. That is, those that, once trained with previously known data, can predict the outcome of new, unseen data. A typical [CAD](#) system,

like the one in Figure 2.5, consists of input data (in our case, neuroimaging), feature extraction, feature selection and a classification step. The most basic is the Voxels As Features (VAF) approach, in which all voxels are considered as features, and then used as input to the classifier [70]. However, many more advances can be made in this field by exploring different types of

#### 2.4.1 Voxels as Features

Voxels As Features (VAF) [70] is an example of the simplest CAD system. It was originally proposed for evaluating and performing automatic diagnosis of AD using functional SPECT imaging. It uses a standard preprocessing (registration, intensity normalization) and a Support Vector Classifier (SVC) (See Appendix B) to predict the class of an image using all its intensities as features. Feature extraction, here, considers all voxels, and then there is no feature selection applied.

It has been used in many works as a baseline [7, 48, 49], since it is comparable to the performance achieved by expert physicians using visual analysis [70]. The weight vector of the SVC can be inverse transformed to the dimension of the original images, and therefore provide a visual map that reflects the most influential voxels, in a similar way to the Z-maps of SPM and VBM.

#### 2.4.2 Multivariate Analyses

Many improvements can be made to VAF by adding and refining feature extraction and feature selection techniques. With this addition, we can avoid the Small Sample Size, in addition to the ability to discover higher level abstractions that can be more representative of the progression of the studied diseases.

Feature extraction algorithms often change the strategy from a massive univariate approach, where a single feature is considered at each time, to multivariate analyses, where each feature can contain information from many voxels at the same time. Measures of total uptake of a given drug in nuclear imaging are a good example of this [60, 64], but also the widespread Cortical Thickness [90] provided by *FreeSurfer*. Cortical thickness is an estimation of the amount of GM in a direction perpendicular to its surface. It first estimates the GM-WM and the WM-CSF separation surfaces, and then characterizes the thickness of the tissue, allowing a characterization of GM differences such as atrophy or hypertrophy. Other pieces of software, such as SPM, also include toolboxes to compute cortical thickness, providing outputs such as the one that can be seen in Figure 2.6.

Other more advanced algorithms are image decomposition techniques such as PCA or Partial Least Squares (PLS), which have been extensively used in neu-

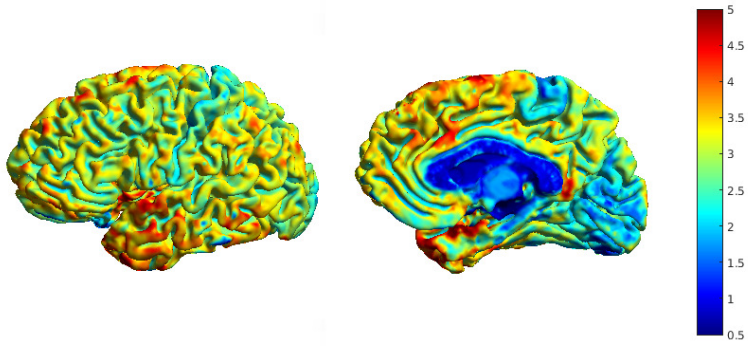


**Figure 2.6:** Example of the cortical thickness of a subject, obtained with the toolbox CAT12 in SPM12.

roimaging CAD systems [10, 27, 37, 39, 49]. In these approaches, a given image can be represented as the linear combination of different components, and while the component loadings are common to all subjects, the weights of these components are unique to each patient. This allows us to identify the patterns that better discriminate between classes, leading to a more accurate diagnosis.

For its part, feature selection refers to different strategies aimed at finding an optimal subset of the extracted features, according to a certain criterion. Irrelevant features are therefore discarded, making our models faster and more cost-effective [74]. Feature selection algorithms are often subdivided in three approaches [5]: filters, wrappers and embedded approaches.

Filters compute a feature relevance score from the data, which is then used to sort the different features. It is computed before the classification, and does not interact with it. Many scores can be derived from statistical features such as  $\chi^2$ , t-Test, Fisher's Discriminant Ratio (FDR) or others [5, 23]. The output of these tests has been already used as a tool in voxelwise analyses, as we commented in Section 2.3.

Wrappers are similar to filtering methods, given that they assign a certain score to each feature. But in contrast to filters, the score is computed by estimating the performance in a predictive model, such as classifiers [101]. The most obvious measure here is accuracy, although other techniques such as Forward selection, backward elimination [74], genetic algorithms [101], or the expectation-maximization algorithm [44] have been used in the literature. And finally, embedded approaches use the very model that is being built to construct their optimal feature subset.



# 3 | GENERAL METHODOLOGY

Throughout this thesis, we will propose many analysis techniques and [CAD](#) systems. We will apply them to many experiments, and use similar data and techniques in them. In this chapter, we will focus on the methodology that is common to most of these experiments, particularly focusing on preprocessing and evaluation of our systems.

To perform most automated analyses on neuroimaging, it is fundamental that images are comparable. Preprocessing comprises a series of algorithms that, applied after the acquisition and reconstruction of the images, produce directly comparable images in both structure and magnitude. Whether they have been used in one or all experiments, they can be classified in two major categories: spatial and intensity preprocessing. These are addressed in Section [3.1](#) and [3.2](#) respectively.

Afterwards, in Section [3.3](#), we will discuss how we evaluate our systems. Here we propose some performance measures and the procedure to obtain them by training and testing our systems.

## 3.1 Spatial Preprocessing

Spatial processing usually accounts for the differences in position, angles and structure that are commonly found between images. A common pipeline in, for example, [MRI](#) preprocessing, is the one found at Figure [3.1](#), where the images are registered (or spatially normalized) to a template, smoothed and finally segmented. The smoothing is an optional step, generally used in procedures like segmentation or [VBM](#).

In this thesis, all the experiments in all image modalities involve spatial normalization. Smoothing, as well as segmentation, is only applied in some experiments that use [MRI](#) images, such as the segmented images in Chapter [6](#) or the whole-brain analysis performed in Chapter [7](#).

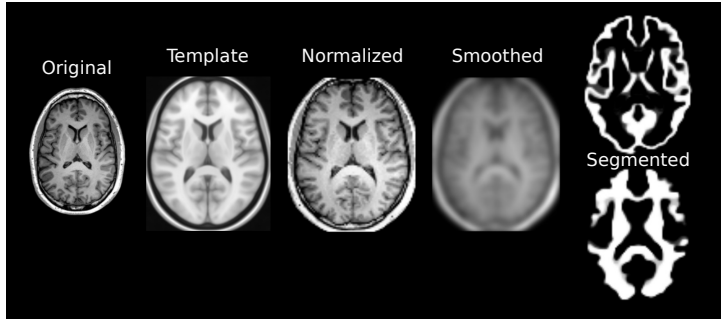


**Figure 3.1:** Typical pre-processing pipeline in [MRI](#).

### 3.1.1 Spatial Normalization or Registration

Spatial Normalization, also known as Registration, is the procedure that by which every subject's brain is mapped from their individual space to a standard reference system. Registered images allows our system to overcome the individual differences in position and anatomy by establishing a common reference space in which a given coordinate represent the same anatomical position in all brains in the dataset.

There exist a number of pieces of software widely used for registering images, such as FreeSurfer [43] or FSL (in the FLIRT and FNIRT package) [69], most of them perform linear, non-rigid and elastic transformations or a combination of these. In this work we have used the software SPM8 [59] to perform registration of all the datasets, including [MRI](#), [SPECT](#) and [PET](#) images. So, from this moment, we will focus on the registration as performed in the Statistical Parametric Mapping Software, version 8 ([SPM8](#)).

Linear registration usually refers to the affine transformation, a matrix multiplication that includes 12 parameters for translation, rotation, scale, squeeze, shear and others:

$$\begin{bmatrix} x' \\ y' \\ z' \\ 1 \end{bmatrix} = \begin{bmatrix} a_{00} & a_{01} & a_{02} & a_{03} \\ a_{10} & a_{11} & a_{12} & a_{13} \\ a_{20} & a_{21} & a_{22} & a_{23} \\ 0 & 0 & 0 & 1 \end{bmatrix} \begin{bmatrix} x \\ y \\ z \\ 1 \end{bmatrix} \quad (3.1)$$

This matrix multiplication is performed globally, as it transforms the whole image, not accounting for local geometric differences. In equations [3.2](#), [3.3](#) and [3.4](#) we give an example of the parameters that are computed for scale, translation and shear in 3D:

$$\text{scale} = \begin{bmatrix} s_x & 0 & 0 & 0 \\ 0 & s_y & 0 & 0 \\ 0 & 0 & s_z & 0 \\ 0 & 0 & 0 & 1 \end{bmatrix} \quad (3.2)$$

$$\text{translation} = \begin{bmatrix} 1 & 0 & 0 & \Delta x \\ 0 & 1 & 0 & \Delta y \\ 0 & 0 & 1 & \Delta z \\ 0 & 0 & 0 & 1 \end{bmatrix} \quad (3.3)$$

$$\text{shear} = \begin{bmatrix} 1 & h_{xy} & h_{xz} & 0 \\ h_{yx} & 1 & h_{yz} & 0 \\ h_{zx} & h_{zy} & 1 & 0 \\ 0 & 0 & 0 & 1 \end{bmatrix} \quad (3.4)$$

The combination of all these operations result in the estimation of the twelve parameters that we found in Eq. 3.1, which are the ones used in [SPM8](#). The estimation of these parameters is performed via the optimization of a cost function, that in [SPM8](#) can be the minimum squared difference between the source image and the template [59] in the case of within-modality registration, or the mutual information in between-modality registration. These functions are also used in [FLIRT](#) [83], whereas FreeSurfer uses the Tukey's biweight function (in `mri_robust_template`) [32].

After the affine transform, the software usually performs a fine-tuning step via nonrigid transformations, to account for relevant anatomical differences between subjects. Nonrigid transformations range from the use of radial basis functions, physical continuum models and the large deformation models, or diffeomorphisms, that [SPM8](#) uses. These procedures work by estimating a warp-field and then, apply it to the affine-registered images. An example of the differences of using only affine registration and applying diffeomorphisms can be found at Figure 3.2.

### 3.1.1.1 Co-registration

Sometimes we have several image modalities of the same subject, for example [MRI](#) and [PET](#) or functional [MRI](#), often acquired at the same time. In this particular case, we can use the higher resolution [MRI](#) image to calculate the affine parameters and warping, and apply those to all modalities of the same subject. To do so, we perform a first co-registration, that is, a registration of the lower-resolution images (e.g. [PET](#)) to its correspondent [MRI](#) image. Being anatomically

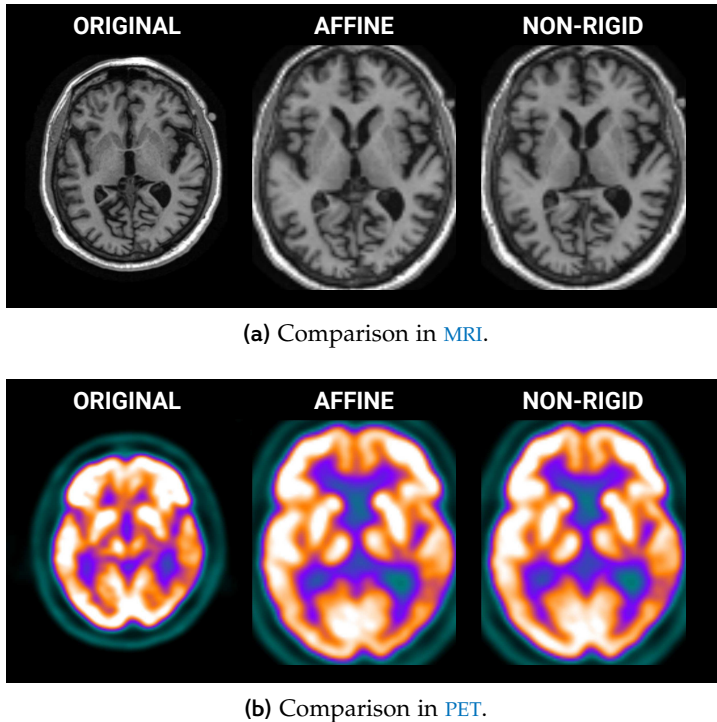


**Figure 3.2:** Comparison of the affine registration and the application of non-linear transformations to both **MRI** and **PET** images of the same **ADNI** subject.

similar, the co-registration usually comprises a single affine transformation. Afterwards, we can proceed with the registration of that **MRI** image to the template, and apply the same transformation to all its co-registered images.

### 3.1.1.2 *The MNI Space*

In this thesis, all images are coregistered to the Montreal Neurological Institute (**MNI**) space [85]. This is the most widely used coordinate system, recently adopted by the International Consortium for Brain Mapping (ICBM) as its standard template. The three-dimensional coordinate system defined in **MNI** was intended to replace the Tilarach space, a system based on a dissected brain, that was used to compose an atlas by Tilarach and Tournoux [106]. The current template is known as ICBM152, and features the average of 152 normal **MRI** scans matched to an older **MNI** template using a nine parameter affine registration.

### 3.1.2 Segmentation

When using [MRI](#) images in this thesis, we often refer to grey matter ([GM](#)) and white matter ([WM](#)) maps, which is the result of the segmentation of the original data. Segmentation aims at producing maps of the distribution of different tissues, and it generally addresses [GM](#), [WM](#) and [CSF](#) classes, although lately some software can output data for bone, soft tissue or very detailed functional regions and subregions [78].

In this thesis we have used the [VBM](#) toolbox of the [SPM8](#) software, which yields [GM](#), [WM](#) and [CSF](#) maps. It features an Expectation-Maximization ([EM](#)) algorithm to model the distribution of the tissue classes as a mixture of gaussians and, by combining this distribution-based information with tissue probability maps using a bayesian rule, the software produces joint posterior probability maps for each tissue. To clean up the segmentation maps, a series of iterative dilations and erosions are used. Finally, since brain regions are expanded or contracted at the spatial normalization step, we can scale the segmented maps using modulation, producing final maps where the total amount of grey matter is preserved.

## 3.2 Intensity Normalization

Generally, structural modalities such as T<sub>1</sub> and T<sub>2</sub>-weighted images are considered unitless, in contrast to functional imaging, in which each voxel's intensity represent the distribution of some biomarker, such as glucose metabolism, dopamine transporters, etc. These amounts are affected by many sources of variability that can affect the final values: contrast uptake, radiotracer decay time, metabolism, etc. Therefore, along with the previous spatial normalization, there is a need to normalize the intensities of the images, so that the amount they represent are comparable.

In the case of intensity normalization, the method acts as a linear transformation of the image, preserving fundamental information such as contrast between regions. This approximation estimates the new intensity values  $I'$  as:

$$I' = I/I_p \quad (3.5)$$

where  $I_p$  is a constant parameter that is unique for each image. After this division, the new intensities would be directly comparable. The technique used to compute the normalization parameter varies, ranging from the simplest normalization to the maximum [31, 48] to complex methodologies that use assumptions about the image's Probability Density Function ([PDF](#)).

The *normalization to the maximum* strategy computes  $I_p$  as the average value of the 95th bin of the histogram of the image. In other words, this mean averaging the 5% higher intensity values and use this mean as  $I_p$ . Another useful approach is the so-called *integral normalization*, which computes  $I_p$  as the sum of all values in the image.

Other approaches involves some a-priori knowledge about the intensity distribution of normal subjects in a certain modality. This is the case of setting  $I_p$  to the Binding Potential (BP), a ratio between the intensities at specific and non-specific areas [67].

Finally, more advanced approaches use a general linear transformation of the image:

$$I' = aI + b \quad (3.6)$$

The parameters  $a$  and  $b$  are so that the [PDF](#) of a given matches a reference [PDF](#). There exist methods that use the histogram [98], the gaussian distribution or the alpha-stable distribution [26]. In this latter case, the parameters  $a$  y  $b$  are computed as linear transformations of some distribution's parameters:

$$a = \frac{\gamma^*}{\gamma}, \quad b = \mu^* + \frac{\gamma^*}{\gamma}\mu \quad (3.7)$$

where  $\gamma^*$  and  $\gamma$  are the dispersion parameters of the alpha-stable intensity distribution of the non-normalized and the reference image respectively, and  $\mu^*$  and  $\mu$  are the location parameters of the same images.

Despite traditionally structural modalities such as [MRI](#) did not use intensity normalization, there exist a new tendency towards the use of quantitative T1 - weighted ([qT1](#)) and quantitative T2 - weighted ([qT2](#)) images [28] that provide biomarkers for absolute measures such as myelination, water and iron levels. This strategy is especially designed to overcome different sources of variability that affect multicentre studies, e.g. magnetic field inhomogeneity, noise, evolution of the scanners, etc. The role of those in multi-centre studies is addressed at Chapter 7.

See Figure 3.3 for a comparison between different strategies of intensity normalization on the same images.

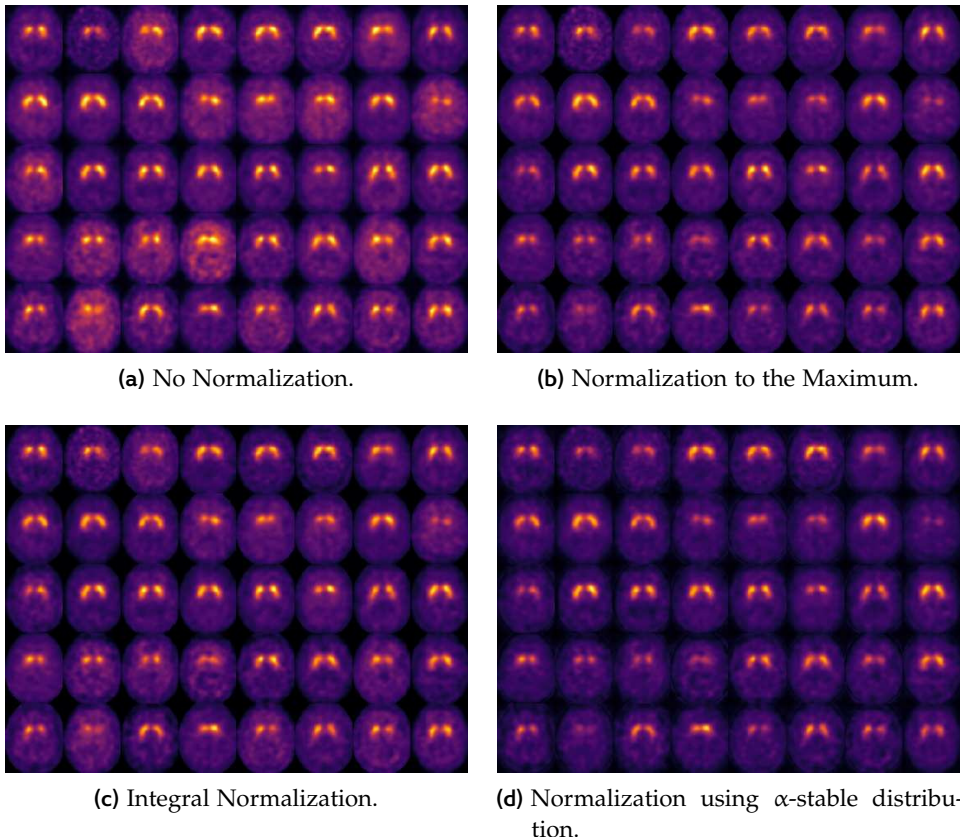


**Figure 3.3:** Comparison between different types of intensity normalization, applied to the VDLN-DAT dataset (see Appendix A).

### 3.3 Evaluation Parameters and Methodology

#### 3.3.1 Cross-validation

Some machine learning applications such as digit or faces recognition use tens of thousands of images as input. In these cases, the common practice is to divide randomly the data in three subsets: training, validation and testing [95]. However, in neuroimaging, sample size is an issue. In contrast to those applications, we only have hundreds of patients in the best case, and the estimation of the performance using these subsets might not be reliable.

In these cases, Cross-validation ([CV](#)) is used to obtain more accurate performance measures. [CV](#) performs a division of the dataset into several subsets  $X = S_1, S_2, \dots, S_k$  and iteratively use some of these subsets for training or testing.

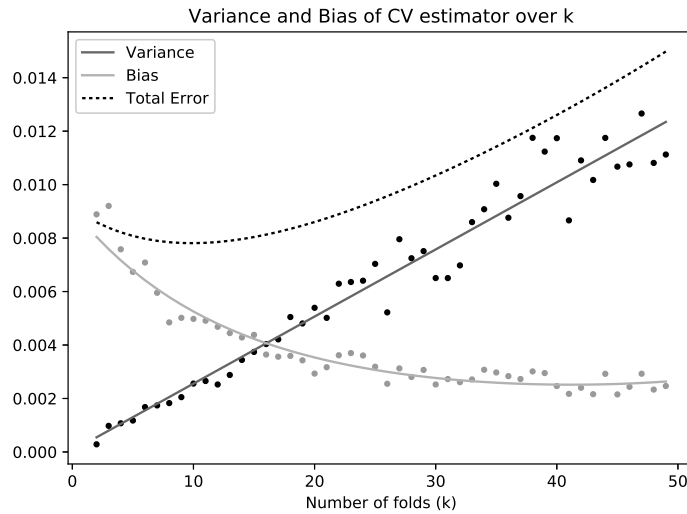


**Figure 3.4:** Evolution of bias and variance when increasing the number of folds in a k-fold [CV](#).

The simplest [CV](#) estimator is k-fold. This approach uses  $k$  equally-sized, non-overlapping subset. For each subset  $S_i$  (or “fold”, hence the name), the model is trained on all subsets  $S_k \forall k \neq i$ , and then evaluated on  $S_i$ . The performance measures, e.g. accuracy, are obtained as the average of the accuracies on each fold.

A particular case where  $k = N$  (where  $N$  is the exact number of subjects in the dataset) is Leave-One-Out ([LOO](#)). This estimator is approximately unbiased for the true accuracy, but can have high variance because there is much overlapping between the  $N$  training set [45]. This imply that the learned models are correlated, and therefore, dependent. All [CV](#) strategies with  $k > 2$  have overlap, and therefore, high variance. See how variance and bias evolve in a k-fold validation in Figure 3.4.

Using  $k = 10$  is assumed as a good compromise between variance and bias in many works [45, 101]. In this thesis, when referring to k-fold, we often use stratified cross validation, which is a subclass of k-fold where the distribution of classes within each fold is similar to the distribution of classes in the whole dataset, making the estimates more accurate [101].

		Predicted	
		Positive	Negative
Actual	Positive	True Positive	False Positive
	Negative	False Negative	True Negative

Table 3.1: Confusion matrix and its parts

### 3.3.2 Classification Performance

From each iteration in the [CV](#) loop, a confusion matrix is obtained, from which all performance measures will be obtained.

The confusion matrix (see Table 3.1) accounts for the number of correct and incorrect predictions: True Positives ([TPs](#)) and True Negatives ([TNs](#)) are correct predictions, and False Positives ([FPs](#)) and False Negatives ([FNs](#)) are incorrect predictions. It also allow us to identify which type of error is our model making, which in hypothesis testing are known as type I errors([FPs](#)) and type II errors ([FNs](#)). The confusion matrix is the basis for computing other performance measures, such as accuracy (acc), sensitivity (sens) or specificity (spec).

$$\text{acc} = \frac{\text{TP} + \text{TN}}{\text{TP} + \text{TN} + \text{FP} + \text{FN}} \quad (3.8)$$

$$\text{sens} = \frac{\text{TP}}{\text{TP} + \text{FN}} \quad (3.9)$$

$$\text{spec} = \frac{\text{TN}}{\text{TN} + \text{FP}} \quad (3.10)$$

Sensitivity is also known as [TP](#) rate or recall in the literature, and specificity is known as [TN](#) rate. Sensitivity is widely used in the medical literature, since it gives an idea of how “sensitive” is our model to the patterns related to a disease (usually considered the positive).



Part II

**REDUCING THE FEATURE SPACE**



# 4

## IMAGE DECOMPOSITION

In this chapter, we will focus on those **CAD** systems that use a combination of an image decomposition method and feature selection by means of hypothesis testing. These variety of methods have been published in [17, 23, 31, 38].

Image decomposition methods model a set of samples as a linear combination of  $c$  latent variables, also known as components. These variables can be considered as the basis of a  $c$ -dimensional space where each sample is represented by a feature vector of length  $c$ . The  $i$ -th neuroimage in our dataset can be therefore decomposed as:

$$\mathbf{x}_i = s_0 \mathbf{w}_0 + s_1 \mathbf{w}_1 + \cdots + s_c \mathbf{w}_c + \epsilon = \mathbf{s} \mathbf{W} + \epsilon \quad (4.1)$$

Where  $s_i$  is the coordinate (or component score) of the current image in the  $i$ -th dimension of the new space defined by all the base vectors  $\mathbf{w}_i$  (component loadings), and  $\epsilon$  is the error of the estimation. Figure 4.1 shows an illustration of the process.



**Figure 4.1:** Illustration of how decomposition algorithms such as **FA** and **ICA** work on a **PET-FDG** brain image.

Many signal decomposition techniques are used in the literature, for example **PCA** or **PLS** [10, 27, 37, 39, 49]. We will focus on two less known decomposition algorithms Factor Analysis (**FA**) and Independent Component Analysis (**ICA**), which we will integrate in different **CAD** systems using a pipeline similar to the one displayed at Figure 4.2. This pipeline involves feature selection (for reducing the dimensionality), decomposition of the feature vectors and classification.

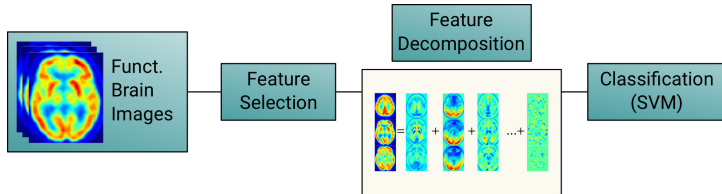


**Figure 4.2:** Illustration of the system used in Chapter 4.

## 4.1 Feature Selection

Feature selection is the first strategy used for feature reduction [5], and it is often used along with feature extraction in order to build more complex pattern recognition systems. It refers to any strategy intended to find a subset of the original features containing the more suitable ones according to a certain criterion. Therefore, irrelevant features are discarded, and resultant models are faster and more cost-effective [74]. However, it usually requires an additional optimization to find the parameters for the optimal feature subset, and furthermore, it is impossible to guarantee that the optimal features for the subset are the same of the full feature set [72].

In this work, we will use filtering methods to perform feature selection. As we introduced in Section 2.4.2, filtering methods are based on the computation of a feature relevance score directly on the data. The relevance score is used to sort the different features, discarding those with a lower score, and it is usually computed independently for each feature, in what is called a univariate approach [62].

Feature selection can be used before or after feature extraction. When using computationally-intensive algorithms such as FA or especially ICA, the selection of best features prior to the decomposition is key to obtain high performance while keeping the computation times small [31, 38]. This also removes noise in some cases where the decomposition algorithm cannot compute correctly the variance.

Three feature selection algorithms have been used in this thesis, not only in the CAD systems proposed in this chapter, but in many other models that will be presented later: the t-Test, the Kullback-Leibler divergence or Relative Entropy, and the Mann-Whitney-Wilcoxon rank test.

### 4.1.1 t-test

The t-test is an old friend of statisticians. In this work we will use the independent two-sample t-test [42]. It quantifies the differences between two classes using an assumption of independent variances. Let  $X_i^f$  a vector containing the f-th feature of all elements in class i. The t-score of the f-th feature can be computed as:

$$t_f = \frac{\bar{X}_1^f - \bar{X}_2^f}{\sqrt{\frac{\sigma_{X_2^f}^2 + \sigma_{X_1^f}^2}{n}}} \quad (4.2)$$

where  $\sigma_{X_i^f}^2$  is the variance and  $\bar{X}_i^f$  is the average of the f-the feature within class i. The t-test is extensively used in the neuroimaging community, and it is the basis for the [SPM](#) and [VBM](#) analyses [59]. See figure 4.13a for an example of the t-test computed on the ADNI-PET database.

### 4.1.2 Kullback-Leibler Divergence

Another alternative is the Kullback-Leibler ([KL](#)) divergence, also known as Relative Entropy. It is a non-symmetric measure of the difference between two probabilities distributions. Let us assume that  $X_1^f$  and  $X_2^f$ , the vectors containing the f-th feature of all elements in class i, are two discrete random variables. Therefore, the [KL](#) divergence can be calculated with equation 4.3 [94].

$$KL_f = \left( \frac{\sigma_{X_2^f}^2}{\sigma_{X_1^f}^2} + \frac{\sigma_{X_1^f}^2}{\sigma_{X_2^f}^2} - 2 \right) + \frac{1}{2} (\bar{X}_2^f - \bar{X}_1^f)^2 \left( \frac{1}{\sigma_{X_1^f}^2} + \frac{1}{\sigma_{X_2^f}^2} \right) \quad (4.3)$$

using the same notation than in t-test. See figure 4.13b for an example of the computed [KL](#) divergence on the ADNI-PET database.

### 4.1.3 Mann-Whitney-Wilcoxon

The Mann-Whitney-Wilcoxon ([MWW](#)) rank test, also known as U-test, assigns a rank to all values in the vector corresponding to the f-th feature,  $X^f$ , without considering any class. The method used to assign a rank is the ‘average’, which means that each value is assigned with the average of the ranks that would have been assigned to all the tied values. This means that, for example, in the case of the vector  $X^f = (0, 2, 3, 2)$ , the ranks assigned to each element would be  $R^f = (1, 2.5, 4, 2.5)$ .

Let  $n_1$  and  $n_2$  be the number of elements in class 1 and 2 respectively, and  $R^f$  the vector of ranked elements. We proceed by selecting the first  $n_1$  elements in  $R^f$  by:

$$R_{n_1}^f = R_i^f \quad \forall i \in (0, n_1) \quad (4.4)$$

The U-score for the f-th feature and the first class will be:

$$U_1^f = n_1 n_2 + n_1 \frac{n_1 + 1}{2} - \sum R_{n_1}^f \quad (4.5)$$

And the it can be computed for the second class as the remainder:

$$U_2^f = n_1 n_2 - U_1^f \quad (4.6)$$

The final  $U^f$  can be assigned to either  $U_1^f$ ,  $U_2^f$  or  $\min U_1^f, U_2^f$  [42], but the usual approach nowadays is to assign  $U^f = U_2^f$ . Unlike t-test, MW test does not assume any prior distribution, and therefore is less likely than it to spuriously indicate significance because of the presence of outliers. Under the normal distribution, it performs relatively similar [42]. See figure 4.13c for an example of the MWU test computed on the ADNI-PET database.

## 4.2 Decomposition Algorithms

The feature selection algorithms presented above will perform a significant feature reduction, from hundreds of thousands of voxels to a few thousands. These few thousands voxels are considered the best in discriminating between CTL and affected subjects in each of the diseases. The feature selection strategy can be thought of as a mask, in which only the most relevant regions according to the tests are selected (see Figure ??).

However, this number of features is still large, and therefore, further feature reduction can be applied by performing a decomposition of the masked regions. We have used two algorithms in our CAD systems: Factor Analysis (FA) and Independent Component Analysis (ICA).

### 4.2.1 Factor Analysis

Factor Analysis (FA) was used in [31, 38] to perform feature extraction in CAD systems. This strategy assumes that each image in the database is a realization of a given experiment. FA then models each of the N observations (or subjects) as the expression of c unobserved variables, known as factors. The model follows the general decomposition equation (Eq. 4.1), but assuming that the dataset

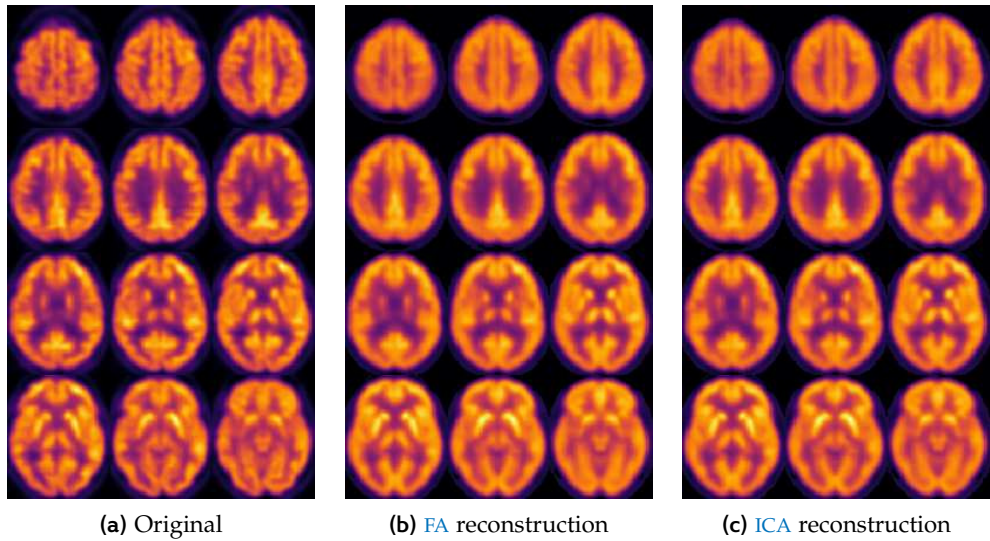


**Figure 4.3:** Original PET image from the ADNI-PET dataset, and examples of reconstruction using FA or ICA, with 10 components.

matrix  $\mathbf{X}$  is zero-centred. That is, that we have subtracted the mean prior to the computation. In matrix form, Eq. 4.1 can be rewritten as:

$$\mathbf{X} - \boldsymbol{\mu} = \mathbf{S}\mathbf{W} + \boldsymbol{\epsilon} \quad (4.7)$$

The columns of  $\mathbf{W}$  are known as factors, and the rows of  $\mathbf{S}$  are known as loadings (similar to the concept of component loading and component scores in PCA). Thanks to this, we can convert the original dataset  $\mathbf{X}$  of size  $N \times f$  into  $\mathbf{S}$ , of size  $N \times c$ . The procedure of computing the decomposition imposes some assumptions on  $\mathbf{W}$ :

- $\mathbf{W}$  and  $\boldsymbol{\epsilon}$  must be independent.
- $E[\mathbf{W}] = 0$ .
- $Cov(\mathbf{W}) = \mathbf{I}$ , which ensures that the factors are uncorrelated.

Now we can rewrite Eq. 4.7 as:

$$Cov(\mathbf{X} - \boldsymbol{\mu}) = Cov(\mathbf{S}\mathbf{W} + \boldsymbol{\epsilon}) \quad (4.8)$$

Under the previous constraints, and setting  $\boldsymbol{\Sigma} = Cov(\mathbf{X} - \boldsymbol{\mu})$ , Eq. 4.8 becomes:

$$\boldsymbol{\Sigma} = \mathbf{S}Cov(\mathbf{W})\mathbf{S}^T - Cov(\boldsymbol{\epsilon}) \quad (4.9)$$

Since  $\text{Cov}(\mathbf{W}) = \mathbf{I}$ , and making  $\text{Cov}(\boldsymbol{\epsilon}) = \boldsymbol{\Psi}$ , the diagonal matrix containing the specific variances of the reconstruction error, we obtain the alternative form of FA:

$$\boldsymbol{\Sigma} = \mathbf{S}\mathbf{S}^T - \boldsymbol{\Psi} \quad (4.10)$$

The mean  $\mu$ , and the matrices  $\mathbf{S}$  and  $\boldsymbol{\Psi}$  are obtained via Maximum Likelihood estimation. To guarantee an unique solution, we impose that  $\mathbf{S}^T\boldsymbol{\Psi}^{-1}\mathbf{S}$  is a diagonal matrix. Then, we obtain the parameters by maximizing the log-likelihood given by the following expression:

$$\ell(\mu, \mathbf{S}, \boldsymbol{\Psi}) = -\frac{np}{2} \log 2\pi - \frac{n}{2} \log |\mathbf{S}\mathbf{S}^T + \boldsymbol{\Psi}| - \frac{1}{2} \sum_{i=1}^n (\mathbf{x}_i - \mu)^T (\mathbf{S}\mathbf{S}^T + \boldsymbol{\Psi})(\mathbf{x}_i - \mu) \quad (4.11)$$

FA differs from PCA mainly because it performs an estimation of the noise, and needs the number of factors  $c$  as an input. Choosing  $c$  is not a naive task. A large  $c$  can yield a small reconstruction error, but the factors will not be representative enough, leading to overfitting of the subsequent model. Conversely, a small  $c$  can lead to a large reconstruction error, causing information loss. We have computed the reconstruction error variance over the ADNI-PET dataset, and plotted it in Figure 4.4 (similar graphs can be obtained for other databases). This proves that the error is asymptotical as we increase  $c$ , and therefore, once arrived at certain error, the improvements are not significant. To observe how the error affects the reconstruction, in Figure 4.3b we can compare a reconstructed image with its corresponding original.



**Figure 4.4:** Specific variance of reconstruction error  $\boldsymbol{\Psi}$  using FA, in function of number of factors extracted ( $K$ ) for ADNI-PET database (the behaviour is similar in other datasets).

### 4.2.2 Independent Component Analysis

Independent Component Analysis (**ICA**) [88] is an algorithm that performs decomposition imposing that the resulting components must be independent. It was used in [Alvarez2009, 31, 38] as part of a **CAD** system, and it had been used in other medical imaging applications such as segmentation [56].

**ICA** was born as a solution to the *blind source separation* problem, in which the aim is to estimate  $c$  independent sources from a series of mixed signals [88]. To do so, we assume the source signals to be non-gaussian, in addition to the independence assumption that we mentioned before. That is why their authors consider **ICA** to be a non-gaussian version of **FA** [75], although due to this assumption, the results are very different to those obtained in **FA**.

Unlike **FA**, **ICA** does not account for noise in the estimation procedure, and therefore the equation remains:

$$\mathbf{X} = \mathbf{WS} \quad (4.12)$$

where **S** are the component scores and **W** are the component loading, ‘sources’ or ‘mixing matrix’. Given that **ICA** lacks a noise term, there is a procedure called *whitening* that must be applied for the algorithm to converge [88]. The whitening implies a linear transformation of the  $i$ -th observed variable  $\mathbf{x}_i$  into a *white* vector  $\tilde{\mathbf{x}}_i$  so that its covariance matrix equals the identity:

$$\mathbb{E}\{\tilde{\mathbf{x}}_i \tilde{\mathbf{x}}_i^T\} = \mathbf{I} \quad (4.13)$$

This procedure is often performed using the eigen-value decomposition (**EVD**) of the covariance matrix  $\mathbb{E}\{\mathbf{x}_i \mathbf{x}_i^T\} = \mathbf{E} \mathbf{D} \mathbf{E}^T$ . **E** is the covariance matrix containing the eigenvectors of  $\mathbb{E}\{\mathbf{x}_i \mathbf{x}_i^T\}$ , and **D** is a diagonal matrix whose diagonal elements are the eigenvalues of  $\mathbb{E}\{\mathbf{x}_i \mathbf{x}_i^T\}$ . Whitening is done using the following equation:

$$\tilde{\mathbf{x}}_i = \mathbf{ED}^{-1/2} \mathbf{E}^T \mathbf{x}_i \quad (4.14)$$

This procedure transform the mixing matrix to:

$$\tilde{\mathbf{x}}_i = \mathbf{ED}^{-1/2} \mathbf{E}^T \mathbf{Ws}_i \quad (4.15)$$

which is indeed orthogonal, as can be seen here:

$$\mathbb{E}\{\tilde{\mathbf{x}}_i \tilde{\mathbf{x}}_i^T\} = \tilde{\mathbf{W}} \mathbb{E}\{\tilde{\mathbf{s}}_i \tilde{\mathbf{s}}_i^T\} \tilde{\mathbf{W}}^T = \tilde{\mathbf{W}} \tilde{\mathbf{W}}^T = \mathbf{I} \quad (4.16)$$

This property reduces the number of parameters to be estimated, since an orthogonal matrix contains  $n(n - 1)/2$  degrees of freedom, in contrast to the  $n^2$  degrees of freedom of the original mixing matrix **W**.

Thanks to the central limit theorem, we assume that the sum of a large number of independent random variables tends will be approximately normally distributed, regardless of the individual statistical distributions [65]. This property is used to maximize non-gaussianity and independence in the sources using any independence criteria such as the kurtosis or negentropy in any of the proposed algorithms. In this work, we will use the FastICA algorithm.

#### 4.2.2.1 FastICA

FastICA is a block fixed-point iteration algorithm [91, 96] based on negentropy as a non-gaussianity measure. Fixed-point algorithms are converge faster than adaptive algorithms [91]. The FastICA algorithm can be considered a neural algorithm [88], where the weight vector  $\mathbf{w}$  can be updated using a learning rule. FastICA defines a learning rule that finds a direction  $\mathbf{w}$ , a unit vector such that the projection  $\mathbf{w}^T \mathbf{x}_i$  maximizes non-gaussianity [91].

The non-gaussianity measure used here is the negative entropy, or negentropy. The negentropy is a form of differential entropy, which for a random vector  $\mathbf{y}$  is defined as:

$$J(\mathbf{y}) = H(\mathbf{y}_{gauss}) - H(\mathbf{y}) \quad (4.17)$$

where  $\mathbf{y}_{gauss}$  and  $\mathbf{y}$  share the same covariance matrix, although  $\mathbf{y}$  is not a gaussian random variable, and  $\mathbf{y}_{gauss}$  is. There are many approximations to negentropy. The FastICA defines negentropy using the function:

$$J(\mathbf{y}) \propto [E\{G(\mathbf{y})\} - E\{G(\mathbf{v})\}]^2 \quad (4.18)$$

where we assume that  $\mathbf{y}$  is of zero mean and unit variance,  $\mathbf{v}$  is a Gaussian variable sharing the same mean and variance, and  $G(x)$  is any non-quadratic function. Many functions have been proposed, but in the FastICA algorithm we use either  $G(x)_1 = (1/\alpha_1) \log \cosh \alpha_1 x$  with  $1 < \alpha_1 < 2$  or  $G(x)_2 = \exp(-x^2/2)$  [91].

With these measures, we can compute the derivatives of these functions by:

$$g_1(x) = \tanh(\alpha_1 x), \quad (4.19)$$

$$g_2(x) = x \exp(-x^2/2) \quad (4.20)$$

The algorithm for the one-unit version of FastICA can be defined [91] as:

1. Choose an initial (e.g. random) weight vector  $\mathbf{w}$ .
2. Let  $\mathbf{w}^+ = E\{\mathbf{x}g(\mathbf{w}^T \mathbf{x})\} - E\{g'(\mathbf{w}^T \mathbf{x})\}\mathbf{w}$
3. Let  $\mathbf{w} = \mathbf{w}^+ / \|\mathbf{w}^+\|$

4. If not converged, go back to 2.

The algorithm considers that the values of  $\mathbf{w}$  converge when their dot product is close to 1, that is, they are pointing in the same direction. Note that the expectations are computed as the sample mean in the FastICA algorithm. Additional modifications were presented in [88], in which step 2 is converted to a Newton iteration and further simplification is performed.

This is the algorithm for one computational unit, or neuron, which computes one component. However, the procedure can be extended to  $c$  components by defining  $c$  neurons with weight vectors  $\mathbf{w}_1, \dots, \mathbf{w}_c$  so that  $\mathbf{W} = (\mathbf{w}_1, \dots, \mathbf{w}_n)^T$ . The outputs  $\mathbf{w}_1^T \mathbf{x}, \dots, \mathbf{w}_n^T \mathbf{x}$  must be decorrelated to prevent them from converging to the same maxima, using three methods proposed in [88].

The method used in this work uses a two-step iterative algorithm [88] to decorrelate the outputs after each iteration:

1. Let  $\mathbf{W} = \mathbf{W} / \sqrt{\|\mathbf{W}\mathbf{W}^T\|}$ .
2. Let  $\mathbf{W} = \frac{3}{2}\mathbf{W} - \frac{1}{2}\mathbf{W}\mathbf{W}^T\mathbf{W}$

And repeat step 2 until convergence. For simplicity, the norm in step 1 can be computed as any norm but the Frobenius norm, for example, the L2-norm or the largest absolute row sum.

## 4.3 Results

In this work we will analyse the behaviour of the system proposed in the introduction and illustrated at Figure 4.2. The system comprises the selection of the most relevant voxels using filtering methods (we will focus on t-test, relative entropy and wilcoxon) and a feature decomposition of these using either FA or ICA. Finally, the feature vectors are classified using a SVC with linear kernel, and performance values are obtained via cross-validation (see Section 3.3 for more information).

We vary the number of selected voxels and the number of factors or components depending on the algorithm and the dataset used and evaluate the system with those characteristics. That way, we obtain an estimation of the performance of the system in different situations, so that we can draw conclusions on the disease patterns and the ability of the system in the detection of different diseases.

### 4.3.1 Alzheimer's Disease

We begin by applying the proposed feature selection plus decomposition pipeline to the two functional neuroimaging datasets: ADNI-PET and VDNL-HMPAO. For this experiment we will use a maximum of 20,000 selected voxels and 25 components.

#### 4.3.1.1 Factor Analysis

First, we use [FA](#) as a decomposition technique. In Figure [4.5](#) we average the accuracy over the number of voxels or the number of components respectively, to look at how these variables affect the performance of the system, and we do this for the three filtering methods used.

We can observe that the results are generally better when using the ADNI-PET dataset than with the VDNL-HMPAO, and this is especially notorious when using the relative entropy selection criterion. The performance tends to slightly increase with the number of voxels selected, but it is not the case with the number of components. By looking at figures [4.5b](#), [4.5d](#) and [4.5f](#), it seems that a relatively small number of components (approximately 6) is enough to obtain good performance, and afterwards, the performance holds or even decreases.

#### 4.3.1.2 Independent Component Analysis

In this section, we compute the results of applying [ICA](#) to the ADNI-PET and VDNL-HMPAO datasets. Figure [4.6](#) depicts the average accuracy over the number of voxels or the number of components respectively for the different selection criteria.

The case is similar to the one presented in Section [4.3.1.1](#), where the performance slightly improves when increasing the number of selected voxels. The performance is again better when using the ADNI-PET dataset than with the VDNL-HMPAO, although the behaviour is similar.

The results change when varying the number of components. In this case, although good performance is obtained within the first 5 components in most cases, the model achieves similar performance in both datasets with components between 5 and 10, and then, the estimates diverge. In the VDNL-HMPAO, the performance starts to decrease after this number of components, whereas when using the ADNI-PET dataset, the higher average performance is obtained with  $c > 15$ , especially in the case of the t-test or the wilcoxon selection criteria).



**Figure 4.5:** Average performance and standard deviation of the proposed system using the two AD datasets, FA and the three feature selection criteria: t-test ((a) and (b)), relative entropy ((c) and (d)) and wilcoxon ((e) and (f)).



**Figure 4.6:** Average performance and standard deviation of the proposed system using the three AD datasets, ICA and the three feature selection criteria: t-test ((a) and (b)), relative entropy ((c) and (d)) and wilcoxon ((e) and (f)).



**Figure 4.7:** Performance of the proposed system using the two AD datasets: ADNI-PET and VDNL-HMPAO at the operation point, and how they vary over the number of selected voxels.

#### 4.3.1.3 At the Operation Point

Now we focus on non-averaged values, the values for which our system is optimal: the operation point. In this scenario we see that the tendency is that all systems behave similarly.

When increasing the number of selected voxels, we can see that there is always a tendency of slightly increase in both datasets and decomposition strategies, as can be seen in Figure 4.7. For the ADNI-PET dataset, the maximum accuracies are obtained with a large number of voxels  $f > 15000$ , however, in the case of VDNL-HMPAO, we obtain similar performance with fewer voxels,  $f < 7000$  in all selection criteria.

Now we can focus on the performance variations over the number of components in Figure 4.8. The accuracy slightly varies almost in any case, and there is



**Figure 4.8:** Performance of the proposed system using the two [AD](#) datasets: [ADNI-PET](#) and [VDLN-HMPAO](#) at the operation point, and how they vary over the number of components used in the decomposition.

a steep increase in the performance within the first five components in both [FA](#) and [ICA](#).

A particular case is the combination of [FA](#) and the relative entropy selection criteria applied to the [VDLN-HMPAO](#) dataset. In this case there seems to be a trend to achieve a maximum performance at between 5 components. But with the [ADNI-PET](#) dataset, the performance keeps and achieves maximum accuracy with  $c \approx 20$ .

In Table 4.1 we show the performance values obtained at the operation point for our different test combining decomposition algorithms and selection criteria, for the two datasets analysed in this section. It is obvious that both datasets obtain similar performance in almost every case, with values close to 0.9. These values are compared to the baseline classification performance, quantified using [VAF](#) [70]. From this, we can see that the decomposition systems always perform

DB	Dec.	Criterion	Accuracy	Sensitivity	Specificity
ADNI-PET	<a href="#">VAF</a>	-	$0.882 \pm 0.064$	$0.876 \pm 0.099$	$0.890 \pm 0.097$
		t-test	$0.893 \pm 0.074$	$0.886 \pm 0.119$	$0.901 \pm 0.101$
	<a href="#">FA</a>	entropy	$0.893 \pm 0.074$	$0.894 \pm 0.092$	$0.891 \pm 0.088$
		wilcoxon	$0.903 \pm 0.066$	$0.917 \pm 0.079$	$0.891 \pm 0.082$
	<a href="#">ICA</a>	t-test	$0.903 \pm 0.071$	$0.893 \pm 0.100$	$0.910 \pm 0.107$
		entropy	$0.898 \pm 0.059$	$0.917 \pm 0.088$	$0.881 \pm 0.084$
		wilcoxon	$0.903 \pm 0.066$	$0.906 \pm 0.097$	$0.901 \pm 0.094$
VDLN-HMPAO	<a href="#">VAF</a>	-	$0.802 \pm 0.074$	$0.803 \pm 0.088$	$0.805 \pm 0.145$
		t-test	$0.885 \pm 0.076$	$0.890 \pm 0.127$	$0.875 \pm 0.149$
	<a href="#">FA</a>	entropy	$0.896 \pm 0.092$	$0.907 \pm 0.150$	$0.875 \pm 0.139$
		wilcoxon	$0.885 \pm 0.076$	$0.923 \pm 0.130$	$0.825 \pm 0.154$
	<a href="#">ICA</a>	t-test	$0.885 \pm 0.073$	$0.923 \pm 0.130$	$0.825 \pm 0.154$
		entropy	$0.885 \pm 0.076$	$0.903 \pm 0.132$	$0.850 \pm 0.130$
		wilcoxon	$0.885 \pm 0.076$	$0.907 \pm 0.130$	$0.850 \pm 0.152$

**Table 4.1:** Accuracy, sensitivity, specificity, and their standard deviation at the operation point for each method and its corresponding feature selection criterion, using two [AD](#) datasets.

better than the baseline, but this difference is especially large in the case of the VDLN-HMPAO dataset, which contains very noisy images.

Overall, all methods achieve similar values of accuracy, sensitivity and specificity. When analysing the ADNI-PET dataset, the wilcoxon selection criteria seems to outperform the rest especially with [ICA](#), with a higher accuracy and sensitivity. On the other hand, with the VDLN-HMPAO dataset, either the t-test or the wilcoxon achieves higher sensitivity, but there is no difference in accuracy when decomposing with the [ICA](#) algorithm. When using [FA](#) decomposition, the relative entropy seems to perform better. In general, there seems to be little difference among methods, and a curious relationship between the relative entropy selection and the VDLN-HMPAO dataset that we will discuss later.

### 4.3.2 Parkinson's Disease

Now we will look at how the proposed [CAD](#) system behaves when applied to the three DaTSCAN datasets: VDLN-DAT, VDLV-DAT and PPMI-DAT. For this experiment we will use a maximum of 1500 selected voxels and 25 components, and images that have been previously intensity normalized using the integral normalization algorithm (see Section 3.2).

### 4.3.2.1 Factor Analysis

Firstly, we will explore the average behaviour of the system that uses FA as a decomposition technique. For this purpose, as in previous sections, Figure 4.9 shows how the average performance varies when varying the number of voxels selected and the number of components extracted.

In this case there is a clear difference between datasets, since some of them are more complex than others, usually due to a typical acquisition procedure in DaTSCAN. In the VDLN-DAT, the images were often composed only of a few cuts around the striatum, whereas in PPMI and VDLV-DAT this rarely happens. That would explain the average outperformance of these two datasets over the VDLN-DAT in almost all cases.

Their behaviours are consistent. Usually, there is no variation with the number of voxel selected (except in the obvious case of the VDLN-DAT dataset and the relative entropy selection criterion). However, there are repeated trends regarding the number of components or factors used in the computation. We can see that the performance increases in the first components, and once we have achieve a decent number (between 4 and 6), the performance starts to decrease. This could mean that the decomposition in more than 5 or 6 components only introduces noise and leads to a wrong decomposition.

Again, this behaviour is consistent with the VDLN-DAT dataset, except for one case. It does seem that the interaction between the VDLN-DAT dataset and the relative entropy selection criterion leads to a wrong model. We will explore this question later, in the discussion.

### 4.3.2.2 Independent Component Analysis

Regarding the application of the ICA decomposition model to the DaTSCAN datasets. In Figure 4.10 we present the average accuracy achieved by this model using three different selection criteria and the three PKS datasets.

In average, PPMI-DAT and VDLV-DAT achieve similar performance, while VDLN-DAT generally achieves much poorer results. However, the behaviour of the system when varying the number of voxels or number of components is similar in all three datasets. The tendency is that accuracy does not significantly vary when increasing the number of voxels (except in the case of the relative entropy and VDLN-DAT). In contrast, when varying the number of components, we observe that the maximum performance is achieved in the first components, typically between 5 and 10.



**Figure 4.9:** Average performance and standard deviation of the proposed system using the three PKS datasets, FA and the three feature selection criteria: t-test ((a) and (b)), relative entropy ((c) and (d)) and wilcoxon ((e) and (f)).



**Figure 4.10:** Average performance and standard deviation of the proposed system using the three PKS datasets, ICA and the three feature selection criteria: t-test ((a) and (b)), relative entropy ((c) and (d)) and wilcoxon ((e) and (f)).

### 4.3.2.3 At the Operation Point

Let us now have a look at the behaviour of this system at the operation point, using the parameters  $c$  and  $f$  for which our system is optimal. When varying the number of voxels selected, we obtain the graphs presented at Figure 4.11.

In this case, we obtain again that our system maintains approximately the same performance regardless of the number of voxels selected when tested on both the PPMI-DAT and the VDLV-DAT datasets. In contrast, the performance increases when increasing the number of selected voxels when testing the VDLN-DAT dataset, especially when using the relative entropy criterion. This latter dataset also obtains less performance, whereas the VDLV-DAT achieves the best.

As for the changes in performance when varying the number of components, the results for both FA and ICA based systems are shown in Figure 4.12.

In this first case, the most evident result is the general performance of our system in the three datasets. It is clear that the system performs better when tested on VDLV-DAT than when tested on PPMI-DAT, and both datasets outperform, VDLN-DAT. It is even clearer that when testing on VDLV-DAT, the results are similar using any type of decomposition and selection criteria, with similar performance. We will discuss this issue in more detail later.

The tendency of the performance at the operation point is similar to the average behaviour commented before. In general, there is an accuracy increasing in the first components (usually, between 5 and 10 depending on the decomposition) and then, the performance remains stable. Again, the combination of relative entropy selection and VDLN-DAT achieves striking results. For this dataset, the higher performance is obtained with more than 10 components ( $c = 14$ ), and shows higher variability than other datasets.

Now we will focus on the specific performance values obtained at the operation point, that can be seen in Table 4.2. In this table we observe the differences in performance between datasets and also between CADs using each decomposition strategy.

In general, the systems using ICA tend to perform slightly better than those using FA, although the difference is small. There is little difference between selection criteria as well, although the combination of relative entropy and ICA seems to work better, at least in the PPMI-DAT and VDLN-DAT (in VDLV-DAT all combinations perform equally well).



**Figure 4.11:** Performance of the proposed system using the two PKS datasets: PPMI-DAT, VDLN-DAT and VDLV-DAT at the operation point, and how they vary over the number of selected voxels.



**Figure 4.12:** Performance of the proposed system using the two PKS datasets: PPMI-DAT, VDNL-DAT and VDLV-DAT at the operation point, and how they vary over the number of components used in the decomposition.

DB	Dec.	Criterion	Accuracy	Sensitivity	Specificity
PPMI-DAT	<a href="#">VAF</a>	-	$0.800 \pm 0.071$	$0.831 \pm 0.093$	$0.747 \pm 0.112$
		t-test	$0.917 \pm 0.037$	$0.918 \pm 0.095$	$0.918 \pm 0.091$
	<a href="#">FA</a>	entropy	$0.917 \pm 0.060$	$0.918 \pm 0.076$	$0.921 \pm 0.120$
		wilcoxon	$0.912 \pm 0.056$	$0.927 \pm 0.098$	$0.889 \pm 0.102$
	<a href="#">ICA</a>	t-test	$0.917 \pm 0.056$	$0.900 \pm 0.095$	$0.948 \pm 0.109$
		entropy	$0.928 \pm 0.055$	$0.909 \pm 0.091$	$0.961 \pm 0.090$
VDLN-DAT	<a href="#">VAF</a>	wilcoxon	$0.912 \pm 0.070$	$0.909 \pm 0.100$	$0.920 \pm 0.118$
		-	$0.796 \pm 0.129$	$0.860 \pm 0.143$	$0.675 \pm 0.208$
	<a href="#">FA</a>	t-test	$0.856 \pm 0.111$	$0.887 \pm 0.178$	$0.795 \pm 0.164$
		entropy	$0.890 \pm 0.098$	$0.875 \pm 0.118$	$0.910 \pm 0.116$
	<a href="#">ICA</a>	wilcoxon	$0.864 \pm 0.070$	$0.916 \pm 0.114$	$0.780 \pm 0.183$
		t-test	$0.864 \pm 0.101$	$0.873 \pm 0.174$	$0.840 \pm 0.166$
VDLV-DAT	<a href="#">VAF</a>	entropy	$0.907 \pm 0.075$	$0.889 \pm 0.124$	$0.935 \pm 0.131$
		wilcoxon	$0.873 \pm 0.108$	$0.859 \pm 0.181$	$0.890 \pm 0.151$
	<a href="#">FA</a>	-	$0.918 \pm 0.062$	$0.900 \pm 0.094$	$0.926 \pm 0.087$
		t-test	$0.957 \pm 0.063$	$0.910 \pm 0.094$	$0.973 \pm 0.065$
	<a href="#">ICA</a>	entropy	$0.952 \pm 0.037$	$0.940 \pm 0.066$	$0.964 \pm 0.064$
		wilcoxon	$0.957 \pm 0.033$	$0.940 \pm 0.066$	$0.973 \pm 0.065$
	<a href="#">VAF</a>	t-test	$0.952 \pm 0.037$	$0.940 \pm 0.066$	$0.964 \pm 0.064$
		entropy	$0.947 \pm 0.045$	$0.940 \pm 0.066$	$0.955 \pm 0.076$
		wilcoxon	$0.952 \pm 0.037$	$0.940 \pm 0.066$	$0.964 \pm 0.064$

**Table 4.2:** Accuracy, sensitivity, specificity, and their standard deviation at the operation point for each method and its corresponding feature selection criterion, using three [PKS](#) datasets

## 4.4 Discussion

Now we will discuss the general behaviour of the selection and decomposition algorithm in the **CAD** systems proposed and how they perform on the different diseases and databases.

Our **CAD** system performs reasonably well on the **AD** datasets, where it achieves around 90% accuracy, and more than 92% sensitivity. This is achieved in both systems composed by **FA** and **ICA** regardless of the selection criterion chosen. The system outperforms the visual analysis estimated by means of **VAF** [70] in both cases. In [38] and [31], the systems achieved better performance (up to 95.1% accuracy) when using multivariate quadratic classifiers and **ICA**, different from the **SVC** used here.

We have chosen to evaluate the system only on linear **SVCs** for two main reasons. First, it favours a side-by-side comparison between all methods applied to different datasets in this thesis. And second, linear **SVC** has been proven to be better generalizable than other systems, even in environments where the small sample size is the norm [97].

The selected areas on these **CAD** systems correspond to the highlighted areas in Figure 4.13, in the case of ADNI-PET dataset.

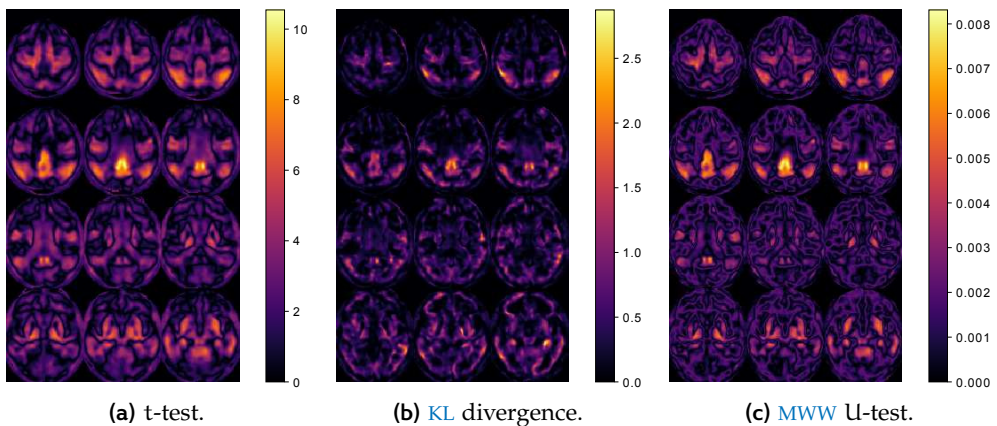


**Figure 4.13:** Comparison between the different filtering methods, and the regions selected by them, in the ADNI-PET dataset.

In the VDNL-HMPAO different areas are selected as we can see in Figure 4.14. This is mainly due to a change in the modality that deserves to be analysed.

To have a more profound look at the selected regions in both modalities, we provide Table 4.3, where the AAL regions with an overlapping higher than 0.5 in any of the modalities and selection criteria are displayed.

Region	ADNI-PET			VDLN-HMPAO		
	entropy	t-test	wilcoxon	entropy	t-test	wilcoxon
Angular_L	<b>1.000</b>	<b>1.000</b>	<b>1.000</b>	<b>1.000</b>	<b>0.858</b>	<b>1.000</b>
Angular_R	0.729	0.782	<b>0.809</b>	<b>0.980</b>	0.566	0.697
Cingulum_Post_L	<b>1.000</b>	<b>1.000</b>	<b>1.000</b>	0.589	0.509	0.773
Cingulum_Post_R	<b>0.843</b>	<b>0.852</b>	0.791	0.524	0.228	0.442
Cuneus_R	0.173	0.121	0.188	<b>1.000</b>	0.683	<b>0.857</b>
Fusiform_L	0.495	0.156	0.167	0.652	0.561	0.713
Hippocampus_R	<b>0.807</b>	0.375	0.413	0.235	0.155	0.425
Occipital_Inf_L	0.378	0.078	0.023	<b>1.000</b>	<b>1.000</b>	<b>1.000</b>
Occipital_Inf_R	0.380	0.080	0.011	<b>1.000</b>	0.794	<b>0.930</b>
Occipital_Mid_L	0.449	0.184	0.138	<b>1.000</b>	<b>0.881</b>	<b>1.000</b>
Occipital_Mid_R	0.347	0.174	0.128	<b>0.861</b>	0.642	0.770
Occipital_Sup_R	0.268	0.094	0.106	<b>0.955</b>	0.600	0.736
ParaHippocampal_L	0.778	0.444	0.465	0.098	0.132	0.262
ParaHippocampal_R	<b>0.917</b>	0.276	0.316	0.233	0.159	0.311
Parietal_Inf_R	0.497	0.414	0.439	<b>1.000</b>	0.339	0.477
Precuneus_L	0.322	0.429	0.463	0.708	0.485	0.660
Precuneus_R	0.311	0.375	0.409	0.770	0.469	0.644
SupraMarginal_L	0.195	0.156	0.183	0.627	0.561	0.762
Temporal_Inf_L	0.748	0.350	0.495	0.676	0.561	0.735
Temporal_Mid_L	0.411	0.244	0.364	<b>0.952</b>	0.635	<b>0.810</b>
Temporal_Mid_R	0.594	0.234	0.326	<b>1.000</b>	0.537	0.711

**Table 4.3:** Percentage of overlap between the selected areas by each method and the AAL atlas regions. For simplicity, overlapping values higher than 0.8 are displayed in bold.

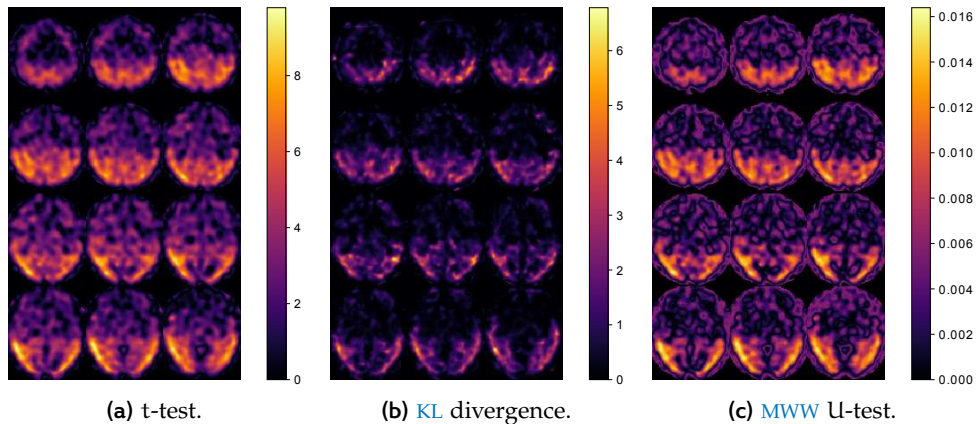


**Figure 4.14:** Comparison between the different filtering methods, and the regions selected by them, in the ADNI-PET dataset.

In the case of the VDLN-HMPAO dataset, the most interesting regions are located at the occipital lobe, the angular lobe and few of them in the temporal lobe. These are selected using almost any of the selection criteria. However, when using the ADNI-PET dataset, the only region with a significant overlapping is the angular lobe, and other regions with a widely documented relation to **AD** are highlighted [57, 103], such as the cingulum, hippocampus and parahippocampal lobe.

It is clearly noticeable that the relative entropy selection criterion focuses on many different regions, but it is the only one able to detect the hippocampus or parahippocampal lobe in the **PET** dataset, which other criteria ignore. It also focuses more on the different parts of the occipital lobe in the **SPECT** dataset. This difference in the selected areas could lead to the different overall performance observed in Figures 4.5c, 4.5d, 4.6c, and 4.6d.

For its part, wilcoxon and t-test often select similar regions. This can be due to their similarity under the normal distribution [42], and leads to a higher performance in the systems in average and at the operation point (see Figures 4.5, 4.6, 4.7 and 4.8). From the selected regions, and since t-test and wilcoxon perform generally better, we can infer the more interesting regions for **AD** classification. For the ADNI-PET dataset, these would be the angular lobes and the cingulum, whereas for the VDLN-HMPAO, we can observe differences in the angular lobe and also all over the occipital lobe and parts of the temporal lobe.

Regarding the decomposition method, there seems not to be any significant differences. Both **ICA** and **FA** perform similarly in both datasets, regardless of the noise contained in the images, although the differences with the baseline

system are much higher in the case of the VDLN-HMPAO dataset. This is perhaps due to the smoother nature of the ADNI-PET, in which several images from the same subject were averaged, and therefore, much of the noise was removed, whereas in the VDLN-HMPAO images, the noise could be removed afterwards by discarding many of the lower-significance components.

When applied to the [PKS](#) datasets, the results differ from the PPMI-DAT and VDLN-DAT to the VDLV-DAT. These databases differ in the number of subjects that they contain. Whereas in the former there are different subjects with [PKS](#), including subjects without evidence of dopaminergic deficit ([SWEDD](#)), in the later we only have [PD](#) and [CTL](#) subjects, which makes the classification easier.

This accuracy differences can be found throughout all figures and tables, although in general, the VDLN-DAT dataset has the lowest performance, while the PPMI-DAT and VDLV-DAT behave similarly in average.

When using [FA](#) with the [PKS](#) datasets, we observe a similar behaviour to that already seen with [AD](#) datasets: there is little difference in performance when varying the number of selected voxels, except when using the relative entropy criterion. In this particular case, there is a rise in the average performance when increasing the number of selected voxels, which is more noticeable when using the VDLN-DAT dataset.

For its part, there are more significant variations when increasing the number of components. Smaller  $c$  values lead to a fast increase in performance up to a maximum. Depending on the selection criterion used, this value varies from  $c = 3$  when using the t-test to  $c = 14$  for the entropy criterion applied to VDLN-DAT. The optimal  $c$  is usually located at  $c \in [3, 5]$  in most cases, as can be seen in Figure 4.9. A very similar behaviour is achieved when using the [ICA](#) decomposition, as Figure 4.10 shows.

In [AD](#) we provided a table with the selected regions in both [PET](#) and [SPECT](#) modalities. Conversely, in DaTSCAN imaging, the selected regions are always in the striatum, and the smaller resolution of these images hardly reveals the underlying structures. The selected regions with either t-test or wilcoxon fundamentally cover the whole caudate, putamen and globus pallidus, and some external structures as well. However, the relative entropy criterion focus almost exclusively in the striatum, with a strong preference for the posterior part, and discards all other regions, introducing less noise.

This is clearly seen in Figure 4.11 where the performance around the operation point is displayed. Here, when looking at the VDLN-DAT dataset, the correlation between performance and number of selected voxels is more obvious. As can be seen in Table 4.2, in the two datasets where [SWEDD](#) subjects are included the system which uses relative entropy achieves better results. How-



**Figure 4.15:** Comparison between the different filtering methods, and the regions selected by them, in the PPMI-DAT dataset.

ever, in the VDLV-DAT, where the system only involves **PD** and **CTL** subjects, the performance is very similar using all three selection criteria.

When looking at the evolution of the performance with the number of selected components, (Figure 4.12), the pattern observed in **AD** holds for the PPMI-DAT and the VDLV-DAT datasets. In these cases, maximum performance is obtained with a relatively small  $c$  (between 4 and 8, depending on the decomposition algorithm). However, with the relative entropy criterion, the VDLN-DAT still needs a higher number (more than 10) to reach the operation point.

All these differences in behaviour could be due to a higher variability in VDLN-DAT, compared to the other two datasets. The number of components needed, especially in **FA**, points to a more complex decomposition of those images. The sources of variability in this dataset probably correspond to a higher proportion of **SWEDD** subjects and the number of cuts used in the acquisition. The number of **SWEDD** in VDLN-DAT is 30 for a total dataset of 148 patients, whereas in the PPMI-DAT dataset we only have 32 **SWEDD** for 301 subjects. Furthermore, the number of cuts in the images of VDLN-DAT differs from one image to another, since they follow a common practice in which only the **ROIs** of the brain (the striatum) are acquired.



# 5

## TEXTURE FEATURES

### 5.1 Introduction

Texture is a household word outside image processing or related fields. However, in that context, it lacks a definition that allow us to measure and quantify it. Pattern recognition provides us with a mathematical definition that allow us to use texture as a feature in our [CAD](#) systems.

Texture analysis is defined as any procedure by which we can quantify and classify the spatial variation of intensity throughout an image. In neuroimaging, texture has been widely used in segmentation (tissue classification) of [MRI](#) images [50, 71, 80], although there exist a number of works using it for feature extraction in [CAD](#)-like systems, like the works in [12, 84], or our work on [PKS](#) feature extraction [18, 22].

Texture features can be classified in first, second and higher order analysis, depending on the number of variables used. First order statistics [5] are the most basic form of texture analysis, computing values such as average, variance or histogram of voxel intensity values [54].

The most popular form, with a very developed theoretical background, is second-order statistical texture analysis. This particular form is based on the probability of finding a pair of similar intensities at a certain distance and orientation of a certain image. From these probabilities, many measures can be derived, being the most popular the Haralick texture analysis [109].

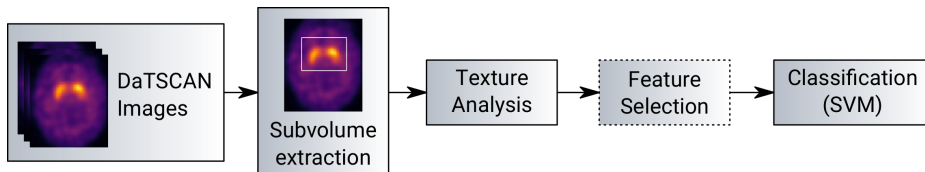


**Figure 5.1:** Schema of the proposed Texture-based [CAD](#) system, including an optional feature selection block.

In this work we have used Haralick texture analysis to extract features from DaTSCAN images and perform an automatic diagnosis of [PD](#). It follows the pipeline depicted at Figure 5.1, as in [18, 22]. First we will provide an introduction to the methodology followed at Section 5.2, including the volume selection

tools, the Haralick texture analysis and the experiments used to validate the system. Later, in Section 5.3 we define the experiments and show their results. Finally, at Section 5.4 we discuss the implications of this systems and the evaluation results of our texture-based CAD system.

## 5.2 Methodology

### 5.2.1 Volume selection

Even the registered DaTSCAN images contain many voxels that are outside the brain. Therefore, to obtain a more robust estimation of the texture, it would be desirable to perform the computation of the features on subvolumes of those images (or subimages) that contain only voxels inside the brain. Many strategies can be performed for this, for example, force the computation of the Grey Level Co-occurrence Matrix (**GLCM**) to ignore background voxels.

In this work, we opted for extracting a subvolume which contains only voxels higher than a certain intensity threshold  $I_{th}$ , which should be specified. To do so, we obtain the maximum and minimum coordinates for which  $I$  is higher than the threshold:

$$p_{x,\min} = \arg \min_x (I > I_{th}) \quad (5.1)$$

$$p_{x,\max} = \arg \max_x (I > I_{th}) \quad (5.2)$$

And we do the same for the  $y$  and  $z$  axis of the array. Once this is computed, we can select the volume by:

$$I_{sub} = I[p_{x,\min} : p_{x,\max}, p_{y,\min} : p_{y,\max}, p_{z,\min} : p_{z,\max}] \quad (5.3)$$

The resulting subvolume  $I_{sub}$  is the minimum box-shaped volume containing all the values for which  $I > I_{th}$ , which allow us to select a  $I_{th}$  so that only the regions of interest are contained within.

Different subimages and sizes are obtained when applying different  $I_{th}$ . In Figure 5.2 we depict a comparison between the resulting images for  $I_{th} = [0.25, 0.30, 0.35]$ .



**Figure 5.2:** Comparison of the different  $I_{th}$  values for a random subject extracted from the PPMI database.

## 5.2.2 Haralick Texture Analysis

### 5.2.2.1 Gray Level Co-occurrence Matrix

The Haralick texture analysis is based on the computation of a Grey Level Co-occurrence Matrix ([GLCM](#)), which is a form of evaluating second-order texture statistics. This matrix is a summary of the probabilities of finding a pair of similar grey levels at a certain distance and in a certain direction.

The combination of the unitary vector dimension and the distance defines the offset  $\Delta = (d_x, d_y, d_z)$ , whose norm is the distance  $d$  and is defined in a given spatial direction. In this work, we use a three-dimensional approach to the computation of the [GLCM](#), based on [53], that uses thirteen spatial directions to generalize the standard 2D [GLCM](#) to 3D. These offset define different angles and are used to get some degree of rotational invariance [53].

Medical images have different number precision, which can vary from regular 8bit integers (256 values) to the type float64 ( $1.844 \times 10^{19}$  possible values). Using all these values, even in the smallest case, would lead to  $256 \times 256$  matrices, which would be both non representative of the real texture and computationally expensive. Therefore, prior to the [GLCM](#) computation, we posterize the image, that is, the image is quantified to use only 16 grey levels. This leads to more tractable [GLCM](#) without losing their representativeness.

Once images have been posterized, for two different grey levels  $i$  and  $j$ , the value of the co-occurrence matrix  $\mathbf{C}$  over a  $n \times m \times k$  three-dimensional image  $\mathbf{I}$  is defined as:

$$\mathbf{C}_\Delta(i, j) = \sum_{\mathbf{p}=(1,1,1)}^{(n,m,k)} \begin{cases} 1, & \text{if } \mathbf{I}(\mathbf{p}) = i \text{ and } \mathbf{I}(\mathbf{p} + \Delta) = j \\ 0, & \text{otherwise} \end{cases} \quad (5.4)$$

where  $\Delta$  is the three dimensional offset that we defined previously, and  $\mathbf{p}$  is the position of a given voxel inside the image.

We will compute one  $16 \times 16$  GLCM for each of the combinations of direction and distances. This matrix  $\mathbf{C}_\Delta$  is later modified to create the probability matrix  $\mathbf{P}$  as:

$$\mathbf{P}(i, j) = \frac{\mathbf{C}_\Delta(i, j)}{\sum_{i,j} \mathbf{C}_\Delta(i, j)} \quad (5.5)$$

from which the texture features will be derived.

### 5.2.2.2 Haralick Texture Features

In [105, 109], many texture features are derived from the probability matrix defined above. We have selected twelve of these features to use in this work. These features are:

$$\text{Energy} = \sum_i \sum_j \mathbf{P}(i, j)^2 \quad (5.6)$$

$$\text{Entropy} = \sum_i \sum_j \mathbf{P}(i, j) \log \mathbf{P}(i, j) \quad (5.7)$$

$$\text{Correlation} = \frac{\sum_i \sum_j ij \mathbf{P}(i, j) - \mu_x \mu_y}{\sigma_x \sigma_y} \quad (5.8)$$

$$\text{Contrast} = \sum_{n=0}^{N_g-1} n^2 \left\{ \sum_{|i-j|=n} \mathbf{P}(i, j) \right\} \quad (5.9)$$

$$\text{Variance} \sum_i \sum_j (i - \mu_i)^2 \mathbf{P}(i, j) + (j - \mu_j)^2 \mathbf{P}(i, j) \quad (5.10)$$

$$\text{Sum Mean} = \frac{1}{2} \sum_i \sum_j (i \mathbf{P}(i, j) + j \mathbf{P}(i, j)) \quad (5.11)$$

$$\text{Inertia} \sum_i \sum_j (i - j)^2 \mathbf{P}(i, j) \quad (5.12)$$

$$\text{Cluster Shade} \sum_i \sum_j (i + j - \mu_x - \mu_y)^3 \mathbf{P}(i, j) \quad (5.13)$$

$$\text{Cluster Tendency} \sum_i \sum_j \{i + j - \mu_x - \mu_y\}^4 \mathbf{P}(i, j) \quad (5.14)$$

$$\text{Homogeneity} = \sum_i \sum_j \frac{\mathbf{P}(i, j)}{1 + |i - j|} \quad (5.15)$$

$$(5.16)$$

$$\text{Max Probability} = \max_{i,j} P(i,j) \quad (5.17)$$

$$\text{Inverse Variance} = \sum_i \sum_j \frac{P(i,j)}{(i-j)^2} \quad (5.18)$$

where  $\mu_i$ ,  $\mu_j$ ,  $\sigma_i$  and  $\sigma_j$  are the column and row-wise mean and variance respectively. These feature measure things such as the randomness of the grey-level distribution (entropy), the number of repeated pairs (energy), the local contrast or homogeneity of the image, variance, the tendency to form clusters (cluster shade and tendency), among others.

For this work we have used a distance  $d$  ranging from 1 to 10, at each of the 13 spatial directions. Therefore, we have computed  $13 \times 10 = 130$  GLCMs per image, from which 12 texture features are computed. Our final feature vector will therefore have 1560 features in total.

To further reduce the dimensionality of the feature vector, we have performed feature selection using the t-test, MWW U-test and the relative entropy (KL divergence) criteria (see Section 4.1).

### 5.2.3 Experiments

For evaluating the system proposed in this chapter, combining texture analysis and other feature selection algorithms, we propose two experiments:

- Experiment 1: Ability of the different texture features to differentiate between PD affected subjects and CTls. Each of the texture features is analysed in two different ways: a "single approach", which only considers one type of feature using only the matrices at a distance  $d$  from the central voxel -and using all the spatial directions- and a "cumulative approach" which considers one type of feature too, but this time using all matrices in distances ranging from 1 to  $d$ .
- Experiment 2: Impact of the introduction of a feature selection algorithm (of those presented at Section 4.1) after computing the texture features. This allow us to pool all texture features at all distances and directions, and then select the most discriminative ones according to some of these criteria.

All images used are intensity normalized using either normalization to the maximum or integral normalization (see Section 3.2), and afterwards, a subvolume can be extracted using the intensity threshold methodology described at Section 5.2.1. In addition to the feature extraction technique using texture analysis, and the feature selection procedure defined for Experiment 2, we use a

linear [SVC](#) for classifying, and 10-fold cross validation strategy (see Section [3.3](#) for more details).

## 5.3 Results

### 5.3.1 Experiment 1

In this experiment, the influence and effect of each texture feature is tested, as in [\[22\]](#). We have tested the computation of the [GLCMs](#) over the image subvolumes using different thresholds  $I_{th}$  (see Sec. [5.2.1](#)) ranging from 0 to 50% of the maximum intensity value, and a range of distances  $d = 1, 2, \dots, 10$  in the thirteen spatial directions.

To check which value of the intensity threshold is the best for computing the texture features, we can compute the general tendency of the system by averaging the accuracy values. Figure [5.3](#) depicts the general trend of the performance over the intensity threshold for either the no normalized or normalized images. This is done for the single and cumulative approach.

The most obvious differences can be found between normalization procedures. As a general trend, the integral normalization barely has an impact over the performance achieved with the registered images. Furthermore, the normalization to the maximum even drops the performance for high  $I_{th}$ , however it increases the general performance in the range 0.1-0.3. From these graphs it is patent that normalization has no impact on the performance achieved by our system, which can be consider an advantage, since it reduces the preprocessing needed.

In this regard, the VDLV-DAT dataset has an strange behaviour. It performance holds and even increases when using normalization to the maximum, but significantly drops when integral normalization is used. This is exactly the opposite as happens to the other dataset, and will be discussed later.

In these images, we can observe a strong dependence of the system's performance with the intensity threshold  $I_{th}$ . In general, the performance increases with a more restrictive threshold (a smaller box around the striatum). This increase is probably due to removing the background from the texture analysis. According to Figure [5.2](#), a value between 0.30 a 0.35 could be indicative of a complete background removal from the computation. In most cases,  $I_{th} \approx 0.35 \times I_{max}$  seems to be a critical value: either the global maximum or the inflection point from which accuracy stabilizes. This would prove that eliminating the background is beneficial for the texture analysis and a posterior classification of the images.



**Figure 5.3:** Evolution of the average accuracy values obtained for the single approach and the cumulative approach over the intensity threshold, using no normalization, normalization to the maximum and integral normalization.

To obtain a deeper insight on the behaviour of each texture feature, we can use a violin plot. This plot is an evolution of the boxplot, frequently used in statistical distributions, in which the distribution of values is shown along with the mean and standard deviation of the set of given data. In our case, we show the violin plot of all accuracy values for each database, grouped by texture feature, at Figure 5.4. Since the performance of the integral normalization was similar to applying no normalization at all, we have only used performance data for the databases normalized to the maximum and the original images.

Figure 5.4 shows the differences between applying or not the normalization to the maximum (in colors), and also the differences in performance obtained depending on the database. We can observe that in average (the white dot), Cluster Tendency is the best performing feature. Homogeneity, Contrast and Correlation also achieve good results. This behaviour is consistent along all three databases, from which we can consider Cluster Tendency the most discriminant feature for PD patterns.

In Tables 5.1 and 5.2, we take a look at the performance achieved by the maximum scoring feature in all databases with different normalization procedures. This is shown for both the single and the cumulative approach.

	Norm.	Feature	$I_{th}$	d	acc.	sens.	spec
PPMI-DAT	Original	Cluster Tendency	45	8	0.952	0.946	0.956
	Integral	Cluster Tendency	45	4	0.952	0.946	0.956
	Maximum	Cluster Tendency	45	8	0.948	0.955	0.943
VDLN-DAT	Original	Cluster Tendency	40	1	0.941	0.956	0.932
	Integral	Cluster Tendency	35	3	0.941	0.978	0.918
	Maximum	Inverse Variance	45	8	0.923	0.933	0.918
VDLV-DAT	Original	Cluster Tendency	35	7	0.941	0.978	0.918
	Integral	Cluster Tendency	30	6	0.904	0.889	0.920
	Maximum	Cluster Tendency	35	1	0.923	0.907	0.940

**Table 5.1:** Maximum scoring feature for each combination of database and normalization procedure, and the intensity threshold and offset distance for which this maximum performance is achieved, using the single approach.

The first noticeable feature is that, for both the single and cumulative approaches, the best scoring normalization method is using no normalization at all. As commented before, that will be discussed later. Secondly, as anticipated, the best scoring feature is Cluster Tendency in most cases, and the systems perform better when the intensity threshold is more restrictive.



**Figure 5.4:** Violin plot of all accuracy values, grouped by database and showing the differences between normalization to the maximum and the original images.

	Norm.	Feature	$I_{th}$	d	acc.	sens.	spec
PPMI-DAT	Original	Cluster Tendency	45	6	0.970	0.982	0.962
	Integral	Cluster Tendency	40	5	0.966	0.982	0.956
	Maximum	Cluster Tendency	45	5	0.966	0.982	0.956
VDLN-DAT	Original	Cluster Tendency	45	7	0.966	1.000	0.945
	Integral	Cluster Tendency	45	7	0.966	1.000	0.945
	Maximum	Cluster Tendency	50	7	0.958	0.978	0.945
VDLV-DAT	Original	Inertia	50	7	0.918	0.963	0.870
	Integral	Inertia	50	6	0.918	0.963	0.870
	Maximum	Cluster Tendency	45	7	0.918	0.944	0.890

**Table 5.2:** Maximum scoring feature for each combination of database and normalization procedure, and the intensity threshold and offset distance for which this maximum performance is achieved, using the cumulative approach.

When comparing the single approach with the cumulative one, it is obvious that best results are obtained with the cumulative one, except for the particular case of the VDLV-DAT. Whereas with the single approach there was no evident choice for the offset distance  $d$ , in the cumulative one results are obtained combining the first 5-7 distances at which the GLCM was computed. This is reasonable, since for the single approach we only use the features contained at each  $d$ , while in the cumulative approach we pool much more information for training and testing the system. Nevertheless, the single approach obtains decent results in many cases, which proves the value of the Haralick texture features for characterizing DaTSCAN images.

### 5.3.2 Experiment 2

In experiment 2 we pool together all features derived from all GLCMs, and use a feature selection algorithm (see Section 4.1). This gives us 1560 features per subject, from a total 12 features computed at 13 directions and 10 distances. We will test how values such as  $I_{th}$ , the normalization algorithm or the percentage of selected voxels affects the performance of this system, and discuss the results.

In Figure 5.5 we show how the performance evolves when varying the  $I_{th}$ , as we did in Experiment 1, by displaying the average accuracy. As in the previous case, the integral normalization performs similarly to the original, non-normalized images. In this case, the normalization to the maximum strategy



**Figure 5.5:** Accuracy obtained by averaging all accuracy values using a given volume selection threshold  $I_{th}$ .



**Figure 5.6:** Average accuracy computed for each selection criteria, using all accuracy values for intensity thresholds of 0.10 to 0.45, compared to the proportion of selected features for the PPMI-DAT, VDLV-DAT and VDLN-DAT databases.

seems to affect more the VDLV-DAT dataset, slightly improving its performance. Again, best  $I_{th}$  seems to be located at approximately 0.30 for all databases when using normalization to the maximum, although for other approaches, this happens with smaller  $I_{th}$  (0.20 for VDLN-DAT and VDLV-DAT original images). For these values, there are still background voxels included in the computation of textures, but its negative influence might be overcome by the feature selection procedure.

These results corroborate that our volume selection strategy is profitable in almost any case, using a intensity threshold between 0.25 and 0.45.

Regarding the different selection criteria, Fig. 5.6 analyses the behaviour of our system under the three proposed methods. For this purpose, we average all accuracy values for a given proportion of selected features (from 1% to 100% of the 1560 total texture features, previously ranked according to the selection criteria), using  $I_{th}$  values ranging from 0.1 to 0.45.

From these figures we can infer that either the t-test or the relative entropy criteria perform better than the [MWW](#) U-test. Of these two, the relative entropy seems to perform the best in the PPMI-DAT and VDLN-DAT datasets, whereas when applied to the VDLV-DAT, the wilcoxon achieves similar results to the relative entropy. In these cases, the relative entropy criterion obtains its maximum average accuracy using the first 10% of features, while wilcoxon needs more than 50% of the features, which makes it less efficient.

After describing the general behaviour, we can take another look at the different combinations of normalization, datasets and selection criteria. In Table 5.3, the peak results of these combinations are shown, including the percentage of selected features needed to achieve this value.

This table confirms that best values are obtained generally by the relative entropy criterion, with few exceptions. It also confirms that best performance is obtained when using the volume extraction method proposed in Sec. 5.2.1, with values of  $I_{th}$  between 0.25 and 0.30. As for the datasets, we see that PPMI-DAT achieves the best performance in all cases, with all selection criteria, whereas, contrary to their average performance examined in Figure 5.5, VDLN-DAT and VDLV-DAT can actually perform similarly.

The application of intensity normalization algorithms does not imply an improvement in performance, and most systems achieve good accuracy without any normalization at all. This was pointed in other analysis, and can be checked again at this table. However, there is only one benefit that can be inferred from the table, which is a decrease in number of selected features needed to achieve best performance with the PPMI-DAT. In this case, and partially in the case of VDLN-DAT as well, similar performance is obtained using either normalized or original images, but when using the normalized data, the percentage of selected features is smaller. Nevertheless, this does not hold for the VDLV-DAT, therefore we cannot consider it a general behaviour.

The choice of a best selection method is here a matter of trade-off between the computer performance (the number of features to estimate) and the accuracy needed. In the case of the PPMI-DAT, it is patent that using normalized images and the t-Test selection criterion achieves best performance. For VDLN-DAT is more difficult to assure that any option will perform better than others, although the t-test still performs well with the original images. Finally, with the VDLV-DAT dataset, the preferred method will be again to use the original images, since the selection of features seems more optimal, especially when using relative entropy. Anyway, all the options reveal the ability of our system in the PD detection with an relevant performance (over 90% of accuracy in most cases).

	Norm.	Selection	$I_{th}$	acc.	sens.	spec.	%
PPMI-DAT	Orig.	<b>entropy</b>	<b>30</b>	<b>0.970</b>	<b>0.972</b>	<b>0.968</b>	<b>0.983</b>
		t-test	30	0.966	0.972	0.962	0.966
		wilcoxon	30	0.959	0.954	0.962	0.858
	Int.	entropy	25	0.966	0.981	0.955	0.308
		<b>t-test</b>	<b>25</b>	<b>0.973</b>	<b>0.990</b>	<b>0.962</b>	<b>0.358</b>
		wilcoxon	35	0.947	0.954	0.943	0.983
	Max.	entropy	25	0.966	0.981	0.955	0.308
		<b>t-test</b>	<b>25</b>	<b>0.973</b>	<b>0.990</b>	<b>0.962</b>	<b>0.358</b>
		wilcoxon	30	0.959	0.954	0.962	0.858
VDLN-DAT	Orig.	entropy	30	0.932	0.933	0.931	0.175
		<b>t-test</b>	<b>30</b>	<b>0.940</b>	<b>0.955</b>	<b>0.931</b>	<b>0.175</b>
		wilcoxon	15	0.898	0.955	0.863	0.433
	Int.	<b>entropy</b>	<b>25</b>	<b>0.932</b>	<b>0.977</b>	<b>0.904</b>	<b>0.100</b>
		t-test	25	0.915	0.955	0.890	0.100
		wilcoxon	25	0.915	0.911	0.917	0.966
	Max.	entropy	20	0.923	1.000	0.876	0.233
		t-test	30	0.932	0.933	0.931	0.225
		<b>wilcoxon</b>	<b>45</b>	<b>0.932</b>	<b>0.933</b>	<b>0.931</b>	<b>0.033</b>
VDLV-DAT	Orig.	<b>entropy</b>	<b>35</b>	<b>0.937</b>	<b>0.935</b>	<b>0.940</b>	<b>0.133</b>
		t-test	35	0.932	0.953	0.910	0.350
		wilcoxon	20	0.927	0.916	0.940	0.383
	Int.	<b>entropy</b>	<b>20</b>	<b>0.937</b>	<b>0.935</b>	<b>0.940</b>	<b>0.983</b>
		t-test	10	0.932	0.907	0.960	0.508
		wilcoxon	10	0.937	0.935	0.940	0.966
	Max.	<b>entropy</b>	<b>20</b>	<b>0.937</b>	<b>0.953</b>	<b>0.920</b>	<b>0.608</b>
		t-test	35	0.932	0.935	0.930	0.341
		wilcoxon	20	0.932	0.925	0.940	0.141

**Table 5.3:** Best results of the experiment 2 per database, normalization and selection criteria. The  $I_{th}$  and percentage of selected features (of the total 1560 features computed) at which each value is obtained is also shown for comparison.

## 5.4 Discussion

The system proposed in this chapter was published in [18, 22], and fundamentally defines a new pipeline for the CAD of PD based on texture analysis. It combines intensity normalization, a subvolume extraction algorithm, texture analysis and classification via SVC.

The application of a intensity normalization procedure was proved fundamental for feature extraction methods such as VAF [30], Singular Value Decomposition (SVD) [33] or PLS [25]. These methods strongly rely on the absolute intensity values found at each anatomical position. Conversely, texture analysis depends on the computation of the GLCM, which quantifies pixel relations. When analysing the behaviour of our system in both experiments, we can infer that normalizing the images does not pose any further improvement over using the original images themselves.

The different experiments still find improvement in using normalization, but these are very small. We find that the type of normalization depends on the database used, and no general trend could be stated. For example, VDLV-DAT has a preference for the normalization to the maximum, whereas the PPMI-DAT performs better when using integral normalization. There were even more cases where normalization decreased performance than those in which it improved the system. Therefore, we can assume that it yields no benefit at all, and therefore, our system can be intensity-independent, which we can consider an advantage.

Now, regarding the volume selection algorithm, it has proved beneficial in almost any case. This can be due to a series of reasons. Firstly, the optimum sub-volume (for an intensity threshold around  $0.30I_{\max}$ ) has a size smaller than  $40 \times 40 \times 50$ . The maximum value at which we computed the GLCMs was  $d = 10$ , which correspond to at least a 20% of the subvolume selected with the previous value. Since the voxel size of the images in the three databases is approximately  $2 \times 2 \times 2$ mm, the maximum textural changes that we could analyse were computed at a distance of 20mm, approximately half the size of the striatum. This is more than enough to characterize texture in these noisy images, since lower frequency textural changes can be obviated for diagnosis, enhancing the descriptive ability of the texture features.

Secondly, the descriptive ability of the texture features is also enhanced with the removal of the background introduced by this subvolume extraction algorithm. Within the subvolume, the texture changes only correspond to real changes represented by the dopamine distribution, and no to the contrast between the brain and the background. And thirdly, computing the texture fea-



**Figure 5.7:** Distribution of the 100 first selected features by means of the different selection methods (using the  $I_{th} = 0.35I_{max}$ ) for PPMI-DAT, VDLN-DAT, VDLV-DAT database.

tures over a subvolume is always faster than over the whole brain, which makes our system faster.

The features that best describe the texture of DaTSCAN images are analysed in Experiment 1. In Fig. 5.4, we saw that features such as homogeneity, Sum Mean and, overall, Cluster Tendency, achieve the best performance of our system in either the single and the cumulative approach, in all three datasets. Since Cluster tendency measures the grouping of voxels with a similar grey-level, it is obviously a good descriptor of the striatum shape, where most of the intensities of the images is concentrated. Higher values of Cluster Tendency can be associated with CTL, whereas lower values can be related to people affected by dopaminergic deficit.

The introduction of a feature selection algorithm using hypothesis testing improved the performance in the three datasets. Thanks to this, we can take best features according to a criterion, and use all of them regardless of what they measure. We would assume that most criteria would select fundamentally Cluster Tendency, Homogeneity and other high performance measures. In Figure 5.7 we count how many features of each type are in the 100 first ranked using each criterion and dataset. We see that the best-performing features such as cluster tendency, are not always selected, especially with the VDLN-DAT dataset, which could be responsible for its lower overall performance. It reveals that each database has internal characteristics, for example, the discarded cuts in VDLN-DAT, that are better modelled using other features, what could lead to the apparition of outliers in the computation, and a decrease in performance. However, the selection approach allow us to overcome the individual characteristics of each dataset, making the system extensible to other uses in clinical practice.

Finally, we will compare our proposed system with other methods used in PD diagnosis in the literature. We will compare with the baseline VAF from [30], and two additional methods. These are an asymmetrical Single Value Decomposition (SVD) [33] that applied SVD on both sides of the brain (since PD often appears only in one hemisphere), and a Empirical Mode Decomposition (EMD) [25] using different Independent Mode Functions (IMF), particularly the IMF-3. These systems are compared with either the cumulative approach and the system of experiment 2 with different criteria in Table 5.4.

In this table, we compare the values at the operation point for Experiment 1 and 2 with other methods in the literature. In Experiment 1, values for six texture features, such as Sum Mean, Homogeneity or Cluster Tendency are shown (using the single approach), and values for the three selection criteria are shown. The values of using only one texture feature match those obtained by state of the art methods like the ones proposed in [25, 33], whereas the methodology used in Experiment 2 outperform all previously used methods. This holds for all feature selection criterion, proving the ability of the Haralick texture analysis to detect PD patterns in DaTSCAN imaging.

<b>System</b>	<b>Acc</b>	<b>Sens</b>	<b>Spec</b>
SumMean	0.951	0.972	0.936
Homogeneity	0.944	0.946	0.943
Cluster Shade	0.940	0.936	0.943
Cluster Tendency	0.951	0.945	0.956
Energy	0.936	0.954	0.924
Correlation	0.944	0.963	0.930
Entropy	0.970	0.972	0.968
t-test	0.966	0.972	0.962
Wilcoxon	0.959	0.954	0.962
VAF	0.840	0.807	0.862
VAF-IN	0.913	0.890	0.932
SVD	0.940	0.962	0.918
EMD-IMF3	0.950	0.951	0.948

**Table 5.4:** Comparison between our proposed system and other PD diagnosis systems in the literature: a VAF system using the intensity-normalized images, a combination of intensity normalization strategies and classifiers (VAF-IN) [30], a SVD-based approach [33] and EMD using the third independent mode function (IMF3) [25].

# 6

## SPHERICAL BRAIN MAPPING

### 6.1 Introduction

In this section we will present a feature extraction technique called Spherical Brain Mapping (**SBM**). **SBM** is based on the use of spherical coordinates to extract radial features from structural **MRI** images. Using the features at each coordinate, we can characterize the texture in each direction, and even project the information to a bidimensional maps, which provides a significant feature reduction and a visual aid for diagnosis.

The most basic form is the standard **SBM** [6, 16], in which all voxels crossed by a rectilinear vector in a spherical coordinate pair  $(\theta, \varphi)$  are selected, and then, a certain measure is extracted from that set. In this sense, statistical and morphological measures such as tissue thickness, average or entropy, among others, are computed.

Further improvements can be made to this simple approach, for example, with the layering extension [6], in which the mapping vector is divided in  $n$  subsets containing the same number of voxels. Therefore, instead of a single map, we can obtain  $n$  maps at different distances from the centre of the brain. Another useful approach is the characterization of texture features via Local Binary Patterns (**LBP**), computed around the mapping vector, which yielded very good results in [11].

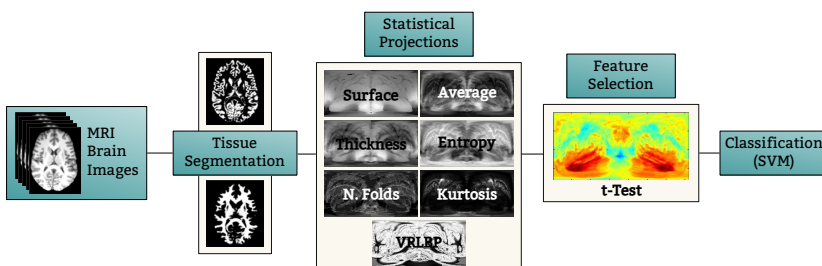


**Figure 6.1:** Flow diagram of the procedure used in the textural analysis of projected MR brain images.

The most relevant extension to the **SBM** was proposed in [7]. In this work, instead of using rectilinear vectors to select voxels, we developed a path creation

algorithm that follows a minimum-intensity change path towards an attractor placed in its corresponding spherical coordinate pair  $(\theta, \varphi)$ . This way, the mapping paths follow the structural features of the [MRI](#) image, which could be used to create the bidimensional [SBM](#) maps as well as directly use the intensity distribution along the path. This was extended to make use of the [GLCM](#) and Haralick texture analysis (see Chapter 5) to characterize the brain texture along each path and its neighbourhood.

## 6.2 Spherical Brain Mapping

The original [SBM](#) proposed in [6, 16] was based on the use of spherical coordinates in the brain. The central voxel is used as the origin point from which a number of mapping vectors  $\mathbf{v}_{\theta,\varphi}$  are defined for each inclination ( $\theta$ ) and azimuth ( $\varphi$ ) angles in the range  $0^\circ < \theta < 180^\circ$  and  $0^\circ < \varphi < 360^\circ$  (see Figure 6.2). The voxels crossed by this mapping vector are selected, to form the sampled set  $V_{\theta,\varphi}$ , a set that contains  $P$  voxels crossed by the mapping vector  $\mathbf{v}_{\theta,\varphi}$ .



**Figure 6.2:** Illustration of the computation of the mapping vector  $\mathbf{v}_{\theta,\varphi}$ , the angles  $\theta$  and  $\varphi$  and the  $r$ -neighbourhood of  $\mathbf{v}$  (see Section 6.2.2).

The basic form in which [SBM](#) works is by computing a mapping value  $v$  from each set  $V_{\theta,\varphi}$  at each coordinate pair  $(\theta, \varphi)$ . In [6, 16], six basic measures were proposed:

- A basic brain surface approach, which is intended to characterize the surface of either **GM** or **WM** tissue. It accounts for the distance between the origin and the last tissue voxel in  $V_{\theta,\varphi}$  greater than a threshold  $I_{th}$ . This might correlate with structural neurodegeneration and tissue loss in the surface of the tissue.

$$v_{surf} = \arg \max_i \{V_{\theta,\varphi}(i) > I_{th}\} \quad \forall i = 1, \dots, P \quad (6.1)$$

- The thickness of the tissue. It is defined as the distance between the last and first elements in  $V_{\theta,\varphi}$  with an intensity greater than a threshold  $I_{th}$  (typically 0). This can be useful when measuring the thickness of segmented **GM** or **WM** maps, and, although less powerful than other implementations like Freesurfer's [90], it might be representative enough and easier to compute :

$$v_{thick} = \arg \max_i \{V_{\theta,\varphi}(i) > I_{th}\} - \arg \min_i \{V_{\theta,\varphi}(i) > I_{th}\} \quad \forall i = 1, \dots, P \quad (6.2)$$

- The number of folds represents the number of overlapping segments of tissue in the set  $V_{\theta,\varphi}$ . It is computed by counting the number of connected subsets in a thresholded  $V_{\theta,\varphi}$  using the value  $I_{th}$ . Let  $A_{\theta,\varphi}$  be the set that contains all the indices of the voxels in  $V_{\theta,\varphi}$  with an intensity greater than  $I_{th}$ :

$$A_{\theta,\varphi} = \{i / V_{\theta,\varphi}(i) > I_{th}\} \quad (6.3)$$

where  $A_{\theta,\varphi} \in \mathbb{N}$ . Let us divide  $A_{\theta,\varphi}$  in  $J$  disjoint connected subsets so that:

$$A_{\theta,\varphi} = A_{\theta,\varphi}^1 \cup A_{\theta,\varphi}^2 \cup \dots \cup A_{\theta,\varphi}^J \quad \text{so that} \quad A_{\theta,\varphi}^i \cap A_{\theta,\varphi}^j = \emptyset \quad \forall i, j \quad (6.4)$$

Therefore, our  $v_{nf} = J$ , the number of disjoint connected subsets in  $A_{\theta,\varphi}$ .

- The average of  $V_{\theta,\varphi}$ :

$$v_{av} = \frac{1}{N} \sum_i V_{\theta,\varphi}(i) \quad \forall i = 1, \dots, P \quad (6.5)$$

- The entropy of  $V_{\theta,\varphi}$ , assuming it is a probability mass vector (probability of belonging to a certain tissue, normalized). It computes  $v$  as:

$$v_{ent} = \sum_i V_{\theta,\varphi}(i) * \log(V_{\theta,\varphi}(i)) \quad \forall i \in \arg_i \{V_{\theta,\varphi}(i) > 0\} \quad (6.6)$$

- The uncorrected kurtosis, also known as fourth standardized moment, of the set  $V_{\theta,\varphi}$  in which  $v$  is calculated using:

$$v_{kurt} = \frac{\frac{1}{N} \sum_i (V_{\theta,\varphi}(i) - \bar{V}_{\theta,\varphi}(i))^4}{\left( \frac{1}{N} \sum_i (V_{\theta,\varphi}(i) - \bar{V}_{\theta,\varphi}(i))^2 \right)^2} \quad \forall i = 1, \dots, P \quad (6.7)$$

where  $\bar{V}_{\theta,\varphi}$  is the average of all voxels in  $V_{\theta,\varphi}$  (same value as  $v_{av}$ , described in Eq. 6.5).

We can compute each of these six maps over the **GM** or **WM** tissue maps of a segmented **MRI**, which are depicted in Figure 6.3. In these maps, the value  $v$  computed at each direction  $(\theta, \varphi)$  is represented, where the azimuth  $\varphi$  is represented in the x-axis, from  $0^\circ$  to  $360^\circ$  and the inclination angle  $\theta$  in the y-axis, from  $0^\circ$  to  $180^\circ$ . The whole algorithm that produces these maps can be downloaded at <http://pakitochus.github.io/mapBrain/>.

This methodology defines the sampling set as the voxels that are crossed by the sampling vector  $\mathbf{v}_{\theta,\varphi}$ . This implies a loss of information on the neighbourhood of  $\mathbf{v}_{\theta,\varphi}$  that increases with the distance to the origin. To overcome this problem, two different approaches have been suggested. In the first one, the sampled set  $V_{\theta,\varphi}$  is divided in  $n$  equal parts, and one map is computed for each of the  $n$  parts, in the “Layered approach”. A second approach uses Local Binary Patterns (**LBP**) and helical sampling to map the neighbourhood of  $\mathbf{v}_{\theta,\varphi}$  and characterize texture. Finally, we will define new paths that adapt to the intensity changes of the brain images, using a **HMM** based approach.

### 6.2.1 Layered Extension

The layered extension is the simplest approach to keep relevant information of the different “layers” of tissue in our **SBM** maps. To do so, we divide each sampled set  $V_{\theta,\varphi}$  in  $n$  equal subsets, from which  $n$  maps will be derived. For example, with a  $n = 4$ , 4 subsets will be used to compute 4 different maps at different distances from the origin, from the closest to the farthest. We assume that this approach features more detail, since overlapping structures placed at different depths will be contained within different maps.

### 6.2.2 Volumetric Radial LBP

Another addition that can be made to the original **SBM** is the inclusion of the  $r$ -neighbourhood of the mapping vector  $\mathbf{v}_{\theta,\varphi}$  in the computation of  $v$ . We do so

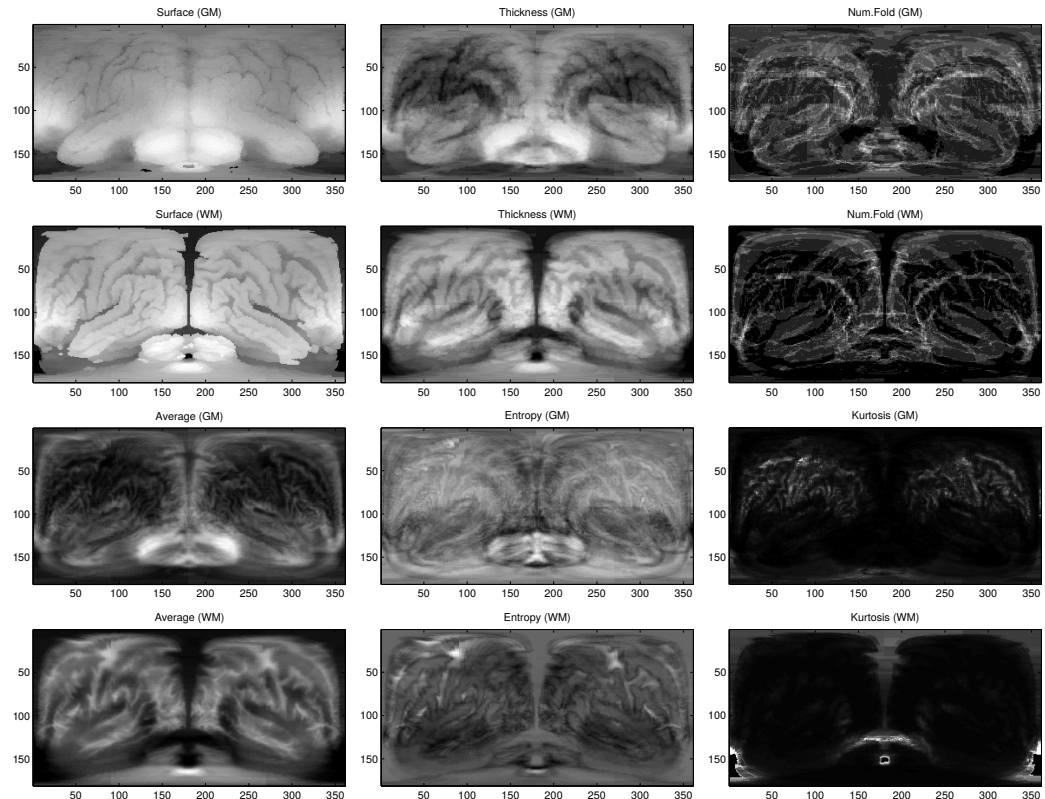


**Figure 6.3:** Resulting GM and WM maps of the same control subject using the six proposed measures: Surface, Thickness, Number of Folds, Average, Entropy and Kurtosis.



**Figure 6.4:** Example of the layered approach using the average measure on GM maps. Some internal GM structures such as the Putamen or Globus Pallidus can be identified at Layer 2 (see anatomical reference at Figures 6.7 and 6.8).

by computing the Volumetric Radial LBP (VRLBP), based on the LBP descriptors proposed in [99].



**Figure 6.5:** Example of how the basic LBP is computed.

LBP was devised to describe the texture of a image, with an initial application to face recognition. In its basic form, it consist of three steps: sampling, calculating the difference and thresholding (See Figure 6.5). The value of the LBP is defined as:

$$v_{LBP} = \sum_{p=0}^{P-1} s(I_p - I_c)2^p \quad (6.8)$$

where P is the number of neighbours at a distance r of the central voxel, and  $I_p$  and  $I_c$  are the intensities of the  $p^{\text{th}}$  voxel and the central voxel for which the

value  $v_{LBP}$  is being computed. The threshold step is performed using the sign function  $s(x)$ , defined as:

$$s(x) = \begin{cases} 1 & x \geq 0 \\ 0 & x < 0 \end{cases} \quad (6.9)$$

This basic approach was extended to Volumetric LBP [63], in which a 3D texture is defined in a local neighbourhood using a cylinder of radius  $r$  oriented in one direction. For this work, we will update the sampling procedure proposed in [63] using a helix around the mapping vector  $\mathbf{v}_{\theta,\varphi}$  (see Figure 6.2). This new helical sampling of [11] defines the set of  $P$  sampled voxels on the image  $I$  using a  $r$ -neighbourhood  $V_{\theta,\varphi}^{P,r}$  as:

$$V_{\theta,\varphi}^{P,r} = \{I(\mathbf{g}_{\theta,\varphi}^{0,r}), I(\mathbf{g}_{\theta,\varphi}^{1,r}), I(\mathbf{g}_{\theta,\varphi}^{2,r}), \dots, I(\mathbf{g}_{\theta,\varphi}^{P-1,r})\} \quad (6.10)$$

where the coordinate vector  $\mathbf{g}_{\theta,\varphi}^{p,r}$  of each voxel are computed in the direction of  $\mathbf{v}_{\theta,\varphi}$  by:

$$\mathbf{g}_{\theta,\varphi}^{p,r} = \begin{cases} x_{\theta,\varphi}^{p,r} = p \sin(\varphi) \cos(\theta) - r \sin(2\pi np/P) \\ y_{\theta,\varphi}^{p,r} = p \sin(\varphi) \sin(\theta) + r \cos(2\pi np/P) \\ z_{\theta,\varphi}^{p,r} = p \cos(\varphi) \end{cases} \quad p = \{0, \dots, P-1\}, P \in \mathbb{N} \quad (6.11)$$

being  $n$  the number of turns in the helical sampling. We use linear interpolation to estimate the intensities in positions that do not fall exactly at the coordinates computed in Eq. 6.11, as in [63].

If we fix  $P$  and  $r$  to constant values, the set of sampled voxels  $V_{\theta,\varphi}^{P,r}$  becomes  $V_{\theta,\varphi}$ , which is similar to the definition of **SBM** found in Section 6.2. The value  $v$  of the **VRLBP** approach is therefore defined as:

$$v_{VRLBP} = \sum_p s(V_{\theta,\varphi}(p) - V_{\theta,\varphi}(0)) \cdot 2^p \quad \forall p = 1, \dots, P \quad (6.12)$$

The resulting texture maps for **GM** and **WM** tissues can be found at Figure 6.6.

### 6.2.3 Anatomical Reference

To better understand the **SBM** maps, and the location of different features, we have projected the widely known [AAL] atlas [Tzourio-Mazoyer2002] using **SBM**. That way, we have an anatomical reference of the different structures and their position in the different coordinate pairs  $(\theta, \varphi)$ . The regions are displayed in Figures 6.7 and 6.8.

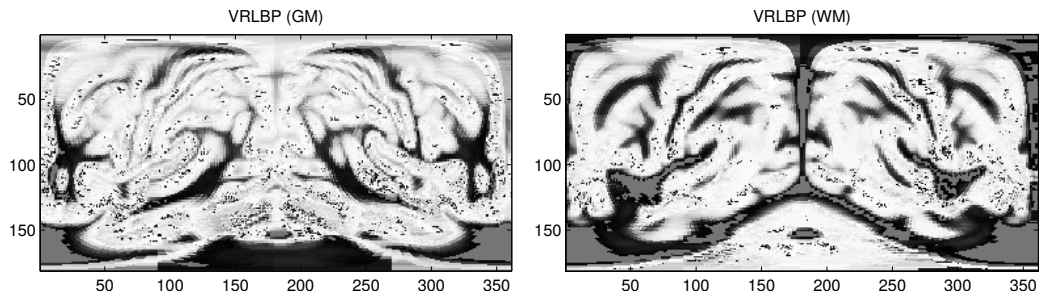


**Figure 6.6:** An example of the [VRLBP](#) projection for [GM](#) and [WM](#) Tissues.

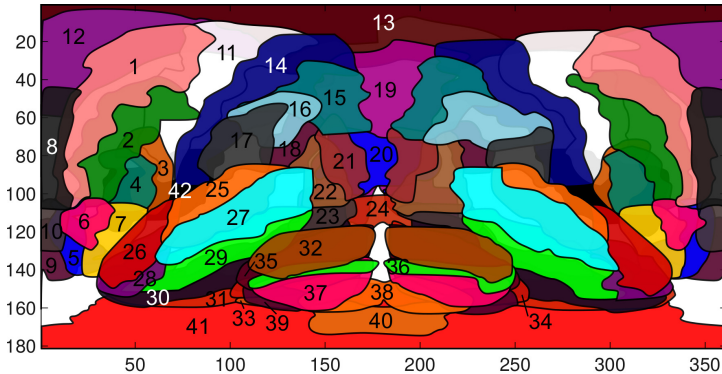


**Figure 6.7:** [SBM](#) mapping of different cortical regions. In the Frontal region, we can find: 1) Frontal Sup., 2) Frontal Mid., 3) Frontal Inf. Oper., 4) Frontal Inf. Tri., 5) Frontal Sup. Orb, 6) Frontal Mid. Orb, 7) Frontal Inf. Orb, 8) Frontal Sup. Medial, 9) Rectus, 10) Frontal Med. Orb., 11) Precentral, 12) Supp. Motor Area. In the Parietal region: 13) Paracentral Lobe, 14) Postcentral, 15) Parietal Sup., 16) Parietal Inf., 17) Supramarginal, 18) Angular. In the Occipital region: 19) Precuneus, 20) Cuneus, 21) Occipital Sup., 22) Occipital Mid., 23) Occipital Inf., 24) Lingual. In the Temporal region: 25) Temporal Sup., 26) Temporal Pole Sup., 27) Temporal Mid., 28) Temporal Pole Mid., 29) Temporal Inf., 30) Fusiform, 31) Parahippocampal. The Cerebellum, divided in: 32) Cerebellum Crus 1, 33) Cerebellum 3, 34) Cerebellum 4-5, 35) Cerebellum 6, 36) Cerebellum 7b, 37) Cerebellum 8, 38) Cerebellum 9, 39) Cerebellum 10. And additionally, the 40) Medulla, 41) Brain Stem and 42) Insula.

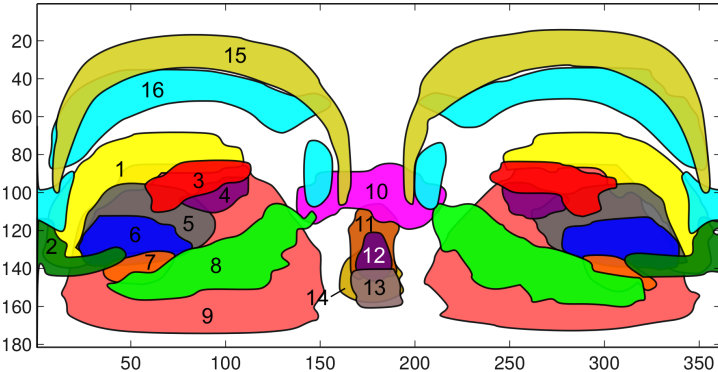


**Figure 6.8:** SBM mapping of some important subcortical regions and organs. We observe the following subcortical structures: 1) Caudate Nucleus, 2) Olfactory Bulb, 3) Rolandic Operculum, 4) Heschl's gyri, 5) Putamen, 6) Globus Pallidus, 7) Amygdala, 8) Hippocampus, 9) Thalamus, 10) Lingual, 11) Vermis 4-5, 12) Vermis 7, 13) Vermis 9, 14) Vermis 1-2, 15) Cingulate Gyrus, 16) Corpus Callosum

### 6.3 Sampling Paths via Hidden Markov Models

The rectilinear mapping vector used in the original SBM [6, 11, 16] has some limitations, partially overcome by the VRLBP and the layered extension. However, a more flexible sampling could be beneficial for the computation of texture measures. In this section we present the technique used to define minimum intensity change sampling paths via Hidden Markov Models, that was firstly proposed in [7]. These paths are defined so that the resulting sampled sets contain information about both intensity and structure of the brain.

To define the paths, we consider each three-dimensional image as a tuple that contains spatial information in the image range (the coordinates  $\mathbf{p} \in \mathbb{I}$ ) where  $\mathbb{I} \subset \mathbb{R}^3$ ) as well as intensity information ( $I(\mathbf{p}) \in \mathbb{R}$ ). The intensity information will be interpreted as a sampling of the underlying tissue density, and therefore, an estimation of the probability of finding tissue in each position.

Following the notation of the VBM defined in Section 6.2, we formulate a 3D path tracing algorithm that defines a curvilinear mapping set of positions  $\mathbb{P}_{\theta, \varphi}$  directly linked to each direction  $(\theta, \varphi)$  that is, at the same time, representative of the underlying intensity distribution. We then use both spatial and intensity information to construct the minimum intensity change paths oriented in the direction  $(\theta, \varphi)$ . Thus, we could note our 3D path in a certain direction as a Markov Model [51]:

$$\mathbb{P}_{\theta, \varphi} = \{\mathbf{p}_0, \mathbf{p}_1, \mathbf{p}_2, \dots, \mathbf{p}_N\} \quad (6.13)$$

Therefore, our optimum path would be the one that maximizes the probability of the path:

$$\mathbb{P}_{\theta,\varphi}^{\text{opt}} = \arg \max_{\mathbb{P}_{\theta,\varphi}} \{P(\mathbb{P}_{\theta,\varphi})\} \quad (6.14)$$

or its equivalent, the probability of all the nodes:

$$P(\mathbb{P}_{\theta,\varphi}) = P(p_0, p_1, p_2, \dots, p_N) \quad (6.15)$$

with  $p_0$  being the origin of the spherical coordinates, and  $p_N$  is the last possible coordinate within  $\mathbb{I}$  in the current direction  $(\theta, \varphi)$ . In this work, we have placed  $p_0$  at the Anterior Commissure (AC) of the image, although other options, such as setting the origin at the middle point of  $\mathbb{I}$  could be considered. This choice is a convention when using the MNI coordinates [Evans1993], sharing connectivity with both hemispheres, therefore allowing the optimal computation of our paths. If we assume a first-order Hidden Markov Model (HMM) for the tracing of the path, the probability of the  $i$ -th node in the path can be approximated as:

$$P(p_i | p_{i-1}, p_{i-2}, \dots, p_0) \approx P(p_i | p_{i-1}) \quad (6.16)$$

Using this assumption, Eq. 6.15 becomes:

$$P(\mathbb{P}_{\theta,\varphi}) = P(p_0, p_1, \dots, p_N) = \prod_{i=1}^N P(p_i | p_{i-1}) \quad (6.17)$$

Using this HMM definition, the hidden state of each node will be its intensity  $I(p_i)$ . Similarly to the original SBM, let  $V_{\theta,\varphi} = \{I(p_0), I(p_1), \dots, I(p_N)\}$  be the set containing all the intensities at each node of the path. Thank to this, our optimal path (Eq. 6.14) can be defined as:

$$\mathbb{P}_{\theta,\varphi}^{\text{opt}} = \arg \max_{\mathbb{P}_{\theta,\varphi}} \{P(\mathbb{P}_{\theta,\varphi} | I)\} \quad (6.18)$$

$$P(\mathbb{P}_{\theta,\varphi} | I) = P(p_0, \dots, p_N | I(p_0), \dots, I(p_N)) \quad (6.19)$$

$$= \frac{P(I(p_0), \dots, I(p_N) | p_0, \dots, p_N) \cdot P(p_0, \dots, p_N)}{P(I(p_0), \dots, I(p_N))} \quad (6.20)$$

where:

$$P(I(p_0), \dots, I(p_N) | p_0, \dots, p_N) = \prod_{i=1}^N P(I(p_i) | p_i) \quad (6.21)$$

and  $P(I(p_0), \dots, I(p_N))$  is the *a priori* probability of the intensities in the path. We can ignore this term in the optimization process under the assumption that it is constant along the path, which is generally true.

To avoid computational overload, we will define a restricted set of candidates from which we will derive all the needed probabilities. This set of candidates are defined inside the L2-norm support ball  $B_{2,r}(\mathbf{p} - \mathbf{p}_{i-1})$  of radius  $r$  centred in  $\mathbf{p}_{i-1}$ , resulting in the candidate set  $\mathbb{P}_{\theta,\varphi}^c = \{\mathbf{p}_{c,1}, \mathbf{p}_{c,2}, \dots, \mathbf{p}_{c,M}\}$ .

Individual probabilities  $P(I(\mathbf{p}_i)|\mathbf{p}_i)$  needed in the computation of Eq. 6.21 can be computed under the assumption of a normally distributed intensity candidate set  $V_{\theta,\varphi}^c$  (containing the intensities of the candidate set  $\mathbb{P}_{\theta,\varphi}^c$ ) with mean  $I(\mathbf{p}_{i-1})$  and variance  $\sigma_c^2$ . We will estimate the probability of the  $i^{\text{th}}$  candidate node  $\mathbf{p}_i$  as:

$$P(I(\mathbf{p}_i)|\mathbf{p}_i) = \frac{1}{\sqrt{2\pi\sigma_c^2}} \exp\left(-\frac{(I(\mathbf{p}_i) - I(\mathbf{p}_{i-1}))^2}{2\sigma_c^2}\right) \quad (6.22)$$

This supports the assumption of minimal intensity change paths, since the  $I(\mathbf{p}_i)$  maximizes its probability when similar to  $I(\mathbf{p}_{i-1})$ .

Finally, we must restrict the direction of the computed path  $\mathbb{P}_{\theta,\varphi}$ , to match the definition of the [SBM](#) framework. We do this by defining the last term  $P(\mathbf{p}_0, \dots, \mathbf{p}_N)$  in Eq. 6.20, setting an attractor located in the position  $\mathbf{p}_N$ , the last possible coordinate within  $\mathbb{I}$  in the current direction  $(\theta, \varphi)$ . It should affect the transition probability between states by means of an isotropic Radial Basis Function ([RBF](#)), defined in Eq. 6.23:

$$P(\mathbf{p}_0, \dots, \mathbf{p}_N) = P(\mathbf{p}_i|\mathbf{p}_N) \quad (6.23)$$

$$= \frac{1}{\sqrt{(2\pi)^d |\Sigma|}} \exp\left(-\frac{1}{2}(\mathbf{p}_i - \mathbf{p}_N)\Sigma^{-1}(\mathbf{p}_i - \mathbf{p}_N)\right) \quad (6.24)$$

where  $\Sigma$  is the covariance matrix of the [RBF](#). For simplicity we will employ an isotropic gaussian kernel, so that  $\Sigma$  is a matrix whose diagonal elements constant and equal to the euclidean distance between  $\mathbf{p}_i$  and  $\mathbf{p}_N$ . This way, the attractor conditions the direction of the path, very slightly in the first nodes, and more strongly as it approaches the cortex, leading to a better representation of the underlying structure.

### 6.3.0.1 Step Size

This algorithm considers all candidate points  $\mathbf{p} \in B_{2,r}(\mathbf{p} - \mathbf{p}_i)$  for each member of the final path  $\mathbb{P}_{\theta,\varphi}$ . Therefore, instead of a fixed step size, we will define the radius  $r$  of the support ball. To avoid computational overload while maintaining good results, we will set  $r = 3$ , which yields approximately 200 candidate points per iteration.

### 6.3.0.2 Stop Condition

The image  $\mathbb{I}$  not only contains information about the structure of the brain, but also many empty space. If the attractor is located at the last point  $\mathbf{p} \in \mathbb{I}$ , we expect the resulting path to reach that point. However, what we are really interested on is the brain itself, so we define a stop condition that considers that the path is finished once it reaches the last voxel inside the brain. To do so, we use an intensity threshold.

This threshold is calculated under the entropic thresholding, as in [Yen1995]. If we note  $G_m \equiv \{I_0, I_1, \dots, I_m\}$  the set containing all intensity levels in the image  $I$  (a vectorized image of length  $m$ ), we can compute a histogram that characterizes the observed frequencies. From these frequencies we can derive the observed probability of the different grey levels. The entropic thresholding defines two distributions after normalization:

$$A \equiv \left\{ \frac{p_0}{P(I_s)}, \frac{p_1}{P(I_s)}, \dots, \frac{p_{s-1}}{P(I_s)} \right\} \quad (6.25)$$

$$B \equiv \left\{ \frac{p_s}{1 - P(I_s)}, \frac{p_{s+1}}{1 - P(I_s)}, \dots, \frac{p_m}{1 - P(I_s)} \right\} \quad (6.26)$$

where  $P(I_s) = \sum_i^s p_{I_i}$  is the cumulative density function for the  $s$ -th grey level. The algorithm is called entropic thresholding because we choose the threshold  $I_{th} = I_s$  so that the total amount of information provided by A and B (which we can consider the foreground and background of the image) is maximized. Therefore, we can define the total information provided by choosing the  $s$ -th grey level as:

$$TE(s) = E_A(s) + E_B(s) \quad (6.27)$$

$$= - \sum_{i=0}^{s-1} \left( \frac{p_i}{P(I_s)} \right) \log \left( \frac{p_i}{P(I_s)} \right) \quad (6.28)$$

$$- \sum_{i=s}^{m-1} \left( \frac{p_i}{1 - P(I_s)} \right) \log \left( \frac{p_i}{1 - P(I_s)} \right) \quad (6.29)$$

The  $s$  that maximizes that latter equation is the grey level that we choose as threshold.

A summary of our HMM-based path tracing method is shown in Algorithm 1. In Figure 6.9 we show all paths computed in all directions  $(\theta, \varphi)$  for  $0^\circ < \varphi < 360^\circ$  and  $0^\circ < \theta < 180^\circ$  at an interval of  $1^\circ$ .

**Algorithm 1: HMM-based Path Creation**


---

**input :** MRI Brain Image  $I$  of size  $U \times V \times W$ ,  $p_0$   
**output:** List of nodes in the optimum path  $\mathbb{P}_{\theta,\varphi}^{\text{opt}}$

---

Compute the  $I_{th} = I_s$  where  $s$  maximizes  $TE(s)$ ;

Set  $p_0$  to the AC;

Compute the attractor position  $p_N$  in the direction  $(\varphi, \theta)$ ;

$p_i \leftarrow p_0$ ;

**while** ( $i < IterLimit$ )  $\&$  ( $I(p_i) > I_{th}$ )  $\&$  ( $p_i \in \mathbb{I}$ ) **do**

Get the node candidates  $\mathbb{P}_{\theta,\varphi}^c = \{p_{c,1}, p_{c,2}, \dots, p_{c,M}\}$  where

$p_{c,m} \in B_{2,r}(p_{c,m} - p_i)$ ;

Get the intensities of the candidates  $I(p_c) \quad \forall p_c \in \mathbb{P}_{\theta,\varphi}^c$ ;

**foreach**  $p_c \in \mathbb{P}_{\theta,\varphi}^c$  **compute**  $P(p_c|p_N)$  and  $P(I(p_c)|p_i)$  ;

$p_{i+1} = \arg \max_{p_c} [P(I(p_c)|p_i) \cdot P(p_c|p_N)]$ ;

$i = i + 1$ ;

$\mathbb{P}_{\theta,\varphi}^{\text{opt}} \leftarrow \{p_0, p_1, \dots, p_N\}$ ;

---

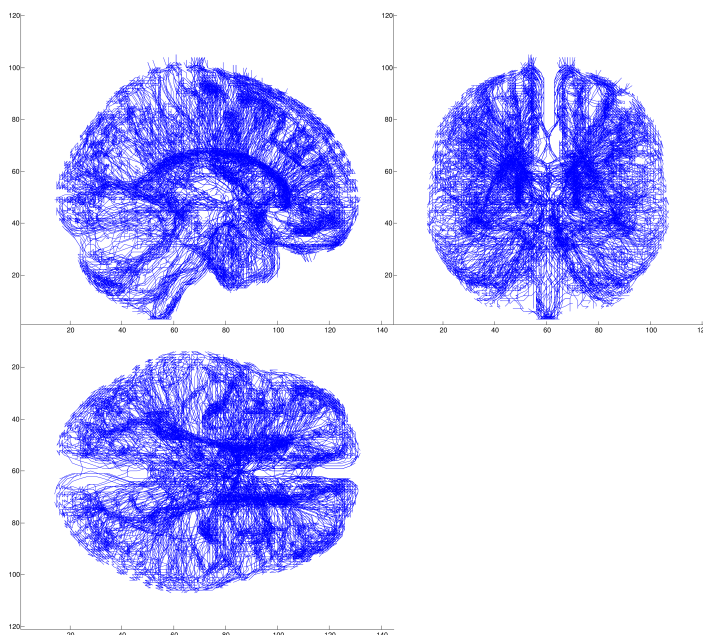


**Figure 6.9:** Set of HMM based paths over the MRI DARTEL template.

### 6.3.1 Radial Texture Features

The paths  $\mathbb{P}_{\theta,\varphi}$  proposed above could theoretically be used as a feature selection tool to extract the set of intensities  $V_{\theta,\varphi}$  as in the standard **SBM**. However, since these new paths contain geometric information, they encode the internal structure, which is itself an additional feature. This encoding could be used to characterize the texture in the neighbourhood of  $\mathbb{P}_{\theta,\varphi}$ .

In [11] a helical sampling was proposed to define the neighbourhood of the mapping vector  $v_{\theta,\varphi}$ . Due to the topology of the **HMM** paths, that is an approach that could not work. Conversely, we propose a modification of the **GLCM** (see Section 5.2.2) that instead of computing the texture in a given direction, characterizes it along the defined **HMM** paths.

This is basically a node-wise **GLCM**, in which the number of grey-level transitions between adjacent nodes, which we could note as  $p_i$  and  $p_{i+1}$ , is stored along the whole path  $\mathbb{P}_{\theta,\varphi} = \{p_0, p_1 \dots p_N\}$ . Mathematically, the computation of the GLCM in each point in the path will be:

$$C_{\Delta_n}(i, j) = \sum_{n=0}^{N-1} \begin{cases} 1 & I(p_n) = i, I(p_{n+1}) = j \\ 0 & \text{otherwise} \end{cases} \quad (6.30)$$

where the offset is different for each pair of nodes  $\Delta_i = p_{i+1} - p_i$ .

The definition in Eq. 6.30 computes the values at each node, without considering the neighbourhood. We can generalize it to include the surrounding vicinity of the  $i$ -th node  $p_i$  in the **HMM** path, which we have noted as the set  $X_i$ . Under this generalization, equation 6.30 becomes:

$$C(i, j) = \sum_{n=0}^{N-1} \sum_{p \in X_i} \begin{cases} 1 & I(p) = i, I(p + \Delta_n) = j \\ 0 & \text{otherwise} \end{cases} \quad (6.31)$$

Once the **GLCM** is computed, we can extract a variety of texture descriptors, as defined in Section 5.2.2.2. Specifically, in this work, we will use the aforementioned Energy (eq. 5.6), Entropy (eq. 5.7), Correlation (eq. 5.8), Contrast (eq. 5.9) and Homogeneity (eq. 5.15), along with other texture features proposed in the original Haralick's article [109] as well as in [92] and [77]. These are Dissimilarity[92] (eq. 6.32), Difference Variance[109] (D. Variance, eq 6.33), Difference Entropy[109] (D. Entropy, eq 6.34), Inverse Difference Normalized[77] (IDN, eq 6.35) and Inverse Difference Moment Normalized[77] (IDMN, eq. 6.36).

$$\text{Dissimilarity} = \sum_i \sum_j \{|i - j|P(i, j)\} \quad (6.32)$$

$$\text{D. Variance} = \text{VAR} \left\{ \sum_{|i-j|=k} P(i, j) \right\} \quad (6.33)$$

$$\text{D. Entropy} = - \sum_{k=0}^{N_g-1} \sum_{|i-j|=k} P(i, j) \log \left\{ \sum_{|i-j|=k} P(i, j) \right\} \quad (6.34)$$

$$\text{IDN} = \sum_i \sum_j \frac{P(i, j)}{1 + |i - j|/N} \quad (6.35)$$

$$\text{IDMN} = \sum_i \sum_j \frac{P(i, j)}{i + (j - i)^2/N^2} \quad (6.36)$$

### 6.3.2 Experiments

In this chapter, we have proposed a completely new framework for extracting features and visualizing structural MRI images from the ADNI-MRI database. To evaluate them, we will combine statistical significance assessment and classification analysis. For this purpose, we propose the following experiments:

- Experiment 1: assessment of the original SBM maps and the VRLBP over segmented GM and WM images. We will provide a statistical significance analysis and a classification analysis under the AD vs CTL scenario of the six proposed maps.
- Experiment 2: assessment of the layered extension of the SBM over segmented GM and WM images. That way, we want to prove if dividing the sampling set, and thus, increasing the depth resolution of the system affects the overall performance of our system. We will provide statistical significance analysis and classification analysis under the AD vs CTL scenario .
- Experiment 3: evaluation of the HMM based paths on simulated datasets, to demonstrate the ability of this algorithm to adapt to different intensity distributions.
- Experiment 4: evaluation of the HMM based paths on a real MRI dataset, by taking the different paths as feature selectors, and evaluating the performance obtained by each individual paths, and a combination of them.

We provide a classification analysis of the selected features under the **AD** vs **CTL** scenario.

- Experiment 5: evaluation of the texture maps derived from the **HMM** based paths on the T1-weighted **MRI** dataset, under a classification analysis of **AD** vs **CTL** subjects.

In the first three experiments, we will use segmented **GM** and **WM** maps, whereas in experiments 5 and 6, we will use raw, T1-weighted images. The classification analysis is performed by using a linear **SVC** for classifying, and 10-fold cross validation strategy (see Section 3.3 for more details). For estimating statistical significance, we use the two-sample t-test defined in Section 4.1.1.

## 6.4 Results

### 6.4.1 Experiment 1: Original and VRLBP Spherical Brain Mapping

First, with experiment 1, we test the original and **VRLBP SBM** maps, by means of significance and classification analysis. To start with, we provide the significance maps computed under the **AD** vs **CTL** scenario in the six original **SBM** measures (surface, thickness, number of folds, average, entropy and kurtosis) in Figure 6.10.

For  $p < 0.05$ , in the database subset of the ADNI-MRI, the significance threshold can be established at  $|t| > 1.96$ . This means that, in Figure 6.10, the most relevant differences between classes can be found at the areas coloured in dark red (positive, **CTL** subjects have a higher measure) and dark blue (negative, **AD** subjects have a higher measure). For the anatomic structures, we refer to the anatomical reference presented in Section 6.2.3.

We first note that the surface measure, tested in both **GM** and **WM** maps, does not look relevant. Very few significant pixels are scattered throughout the image, although with a slightly higher concentration in the areas corresponding to the temporal lobe.

In the remaining **GM** maps, we observe similar behaviours, with higher absolute t-values located in the frontal, occipital and parietal lobes. But again, the most significant areas can be found at the temporal lobe. It is more obvious in the average and entropy measures, but can also be found at the thickness, or negatively in the number of folds and kurtosis maps. This points to the well known fact that most of the neurodegeneration in **GM** occurs within the structures that are mapped to these directions, including mid temporal lobe, amygdala, hippocampus or parahippocampal lobe, considered a strong indicator in

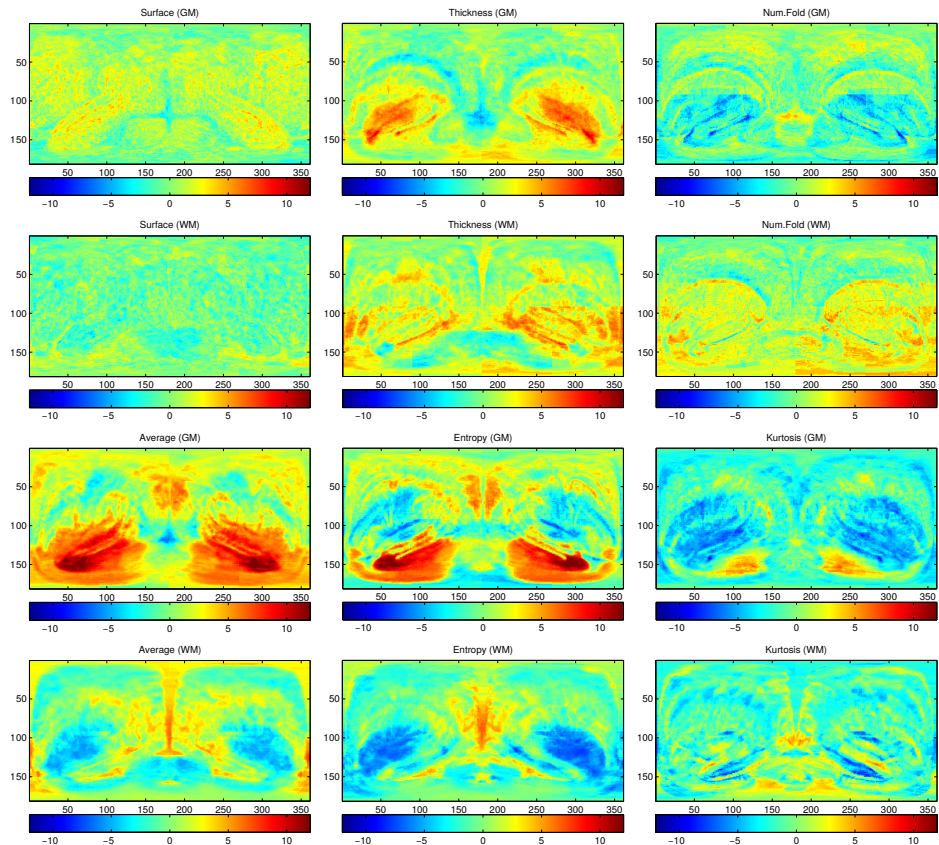


**Figure 6.10:** t-maps to assess the regions with a higher statistical relevance in the **AD** vs **CTL** paradigm, for each **SBM** measure and using **GM** and **WM** maps.

the NINCDS-ADRDA criteria [57]. Other GM structures such as the caudate nucleus and putamen also appear with significant t values, especially in the entropy and kurtosis maps (with negative t) [24].

In the WM, the levels of significance achieved are smaller than in the GM, but still high. We see the higher levels of number of folds and thickness located in the vicinity of those obtained for GM, but in negative. For the average, entropy and kurtosis measures, we observe a different behaviours. These maps present large areas of negative t-values located in the Caudate Nucleus, Globus Pallidus and Putamen. Areas around the posterior cingulate gyrus and the adjacent precuneus also present reduced t values, which could be related to cell loss, as suggested in [82].

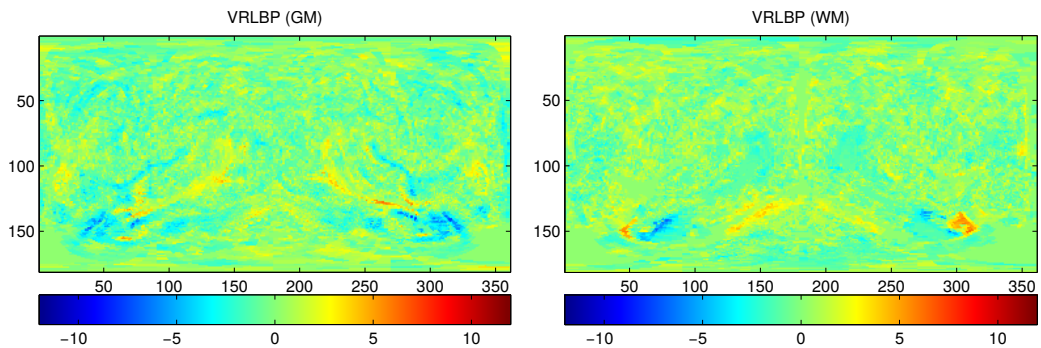


**Figure 6.11:** Maps that present the level of the t statistic in the AD vs. CTL paradigm, for the VRLBP projections mapping over a) GM and b) WM.

Finally, we take a look at the statistical significance of the VRLBP maps. In Figure 6.11, we can observe that most of the image features small t values, however there are small areas that contain higher significance. These areas correspond to the temporal lobe, amygdala and hippocampus (in the GM maps) and smaller regions located at the limits between the hippocampus and amygdala (in WM).

Now, we perform a classification analysis of the images. To this purpose, we will use the computed t-maps to select the most relevant pixels in the SBM maps, which will be used to train and test a SVC. The performance results for the six original measures and the VRLBP approach, including the percentage of selected pixels (perc.), can be found at Table 6.1.

We can see a general trend in which the statistical measures (average, entropy and kurtosis) clearly outperform the morphological ones (surface, thickness and number of folds), although the tissue thickness is the best performing of these, as it could be expected. For GM maps, average ( $0.879 \pm 0.005$ ) and entropy ( $0.846 \pm 0.008$ ) achieve the best performance, followed by thickness ( $0.781 \pm 0.007$ ), kurtosis ( $0.753 \pm 0.019$ ), and finally, the number of folds ( $0.749 \pm 0.013$ ) and sur-

Approach	Perc.	Accuracy	Sensitivity	Specificity
Surface (GM)	0.100	$0.638 \pm 0.006$	$0.660 \pm 0.030$	$0.616 \pm 0.024$
Surface (WM)	0.100	$0.672 \pm 0.007$	$0.692 \pm 0.018$	$0.652 \pm 0.018$
Thickness (GM)	0.725	$0.781 \pm 0.007$	$0.811 \pm 0.011$	$0.751 \pm 0.017$
Thickness (WM)	0.925	$0.758 \pm 0.009$	$0.773 \pm 0.017$	$0.744 \pm 0.011$
Num.Fold (GM)	0.600	$0.749 \pm 0.013$	$0.782 \pm 0.019$	$0.716 \pm 0.013$
Num.Fold (WM)	0.500	$0.757 \pm 0.005$	$0.745 \pm 0.006$	$0.768 \pm 0.009$
Average (GM)	0.575	$0.879 \pm 0.005$	$0.897 \pm 0.006$	$0.861 \pm 0.006$
Average (WM)	0.150	$0.800 \pm 0.011$	$0.802 \pm 0.013$	$0.798 \pm 0.009$
Entropy (GM)	0.825	$0.846 \pm 0.008$	$0.842 \pm 0.009$	$0.849 \pm 0.011$
Entropy (WM)	0.525	$0.796 \pm 0.006$	$0.811 \pm 0.009$	$0.781 \pm 0.009$
Kurtosis (GM)	1.000	$0.753 \pm 0.007$	$0.801 \pm 0.011$	$0.704 \pm 0.015$
Kurtosis (WM)	0.175	$0.697 \pm 0.008$	$0.702 \pm 0.018$	$0.693 \pm 0.009$
VRLBP (GM)	0.200	$0.903 \pm 0.010$	$0.890 \pm 0.012$	$0.916 \pm 0.018$
VRLBP (WM)	0.150	$0.909 \pm 0.014$	$0.899 \pm 0.028$	$0.919 \pm 0.018$

**Table 6.1:** Performance values (Average  $\pm$  Standard Deviation) for the different SBM approaches.

face ( $0.638 \pm 0.006$ ). These results match what we presented previously with the statistical maps, in which the surface contained the less significant measures.

As for the performance of the **SBM** measures based on **WM** maps, the rank is very similar to that obtained for **GM**. Again, average ( $0.800 \pm 0.011$ ) and entropy ( $0.796 \pm 0.006$ ) are the best performing features among the original measures. They are followed by thickness and the number of folds, with respectively  $0.758 \pm 0.009$  and  $0.757 \pm 0.005$ . Finally, the kurtosis and the surface are the less discriminant measures again, with  $0.697 \pm 0.008$  and  $0.672 \pm 0.007$ . All these measures are outperformed by the **VRLBP** approach, which achieves more than 90% accuracy in both **GM** and **WM**.

In Figure 6.12 we explore the evolution of the performance as the number of selected pixels varies. Very small differences in the accuracy exist for most measures, and so, we can consider that the performance of the **SBM**, once that a few thousand significant pixels (a 10% of  $181 \times 361 = 65341$ ) have been selected, the system performs well independently of that number. That is, however, not the case of the surface approach, and more remarkably, of the **VRLBP**. In this latter case, for both tissues, the performance is high in the first 40% of selected voxels, but after that, it dramatically decreases down to less than 70% accuracy.

#### 6.4.2 Experiment 2: Layered Extension

In Experiment 2, we have assessed how the performance of our **SBM** varies when adding different layers, which could theoretically improve the accuracy of the **SBM** representation. First, we will take a look at the performance achieved by this extension on all six original **SBM** maps, using 4 layers and different t-thresholds (2, 4, 8 and 10). This is presented at Figure 6.13.

The first thing that we can observe is that for **GM** maps, the better performance is achieved within the second and third layers, and only for the second layer in the case of **WM**. In almost all cases, the average performance achieves higher accuracy than any other **SBM** measure, closely followed by entropy. It also tells us that, with less restrictive t-thresholds, the performance generally decreases, and the best values are between 2 and 4.

Performing a significance analysis on the 4 layer extension of the 7 proposed **SBM** maps over the **GM** and **WM** images could be infeasible for this thesis, therefore we will only provide t-maps of the best performing measure: the average on the **GM** and **WM** tissues. The significance assessing of this case is found at Figure 6.14.

In **GM**, the most obvious changes are located in layers 2 and 3, specifically at the hippocampus, parahippocampal lobe and amygdala (layer 2), and the

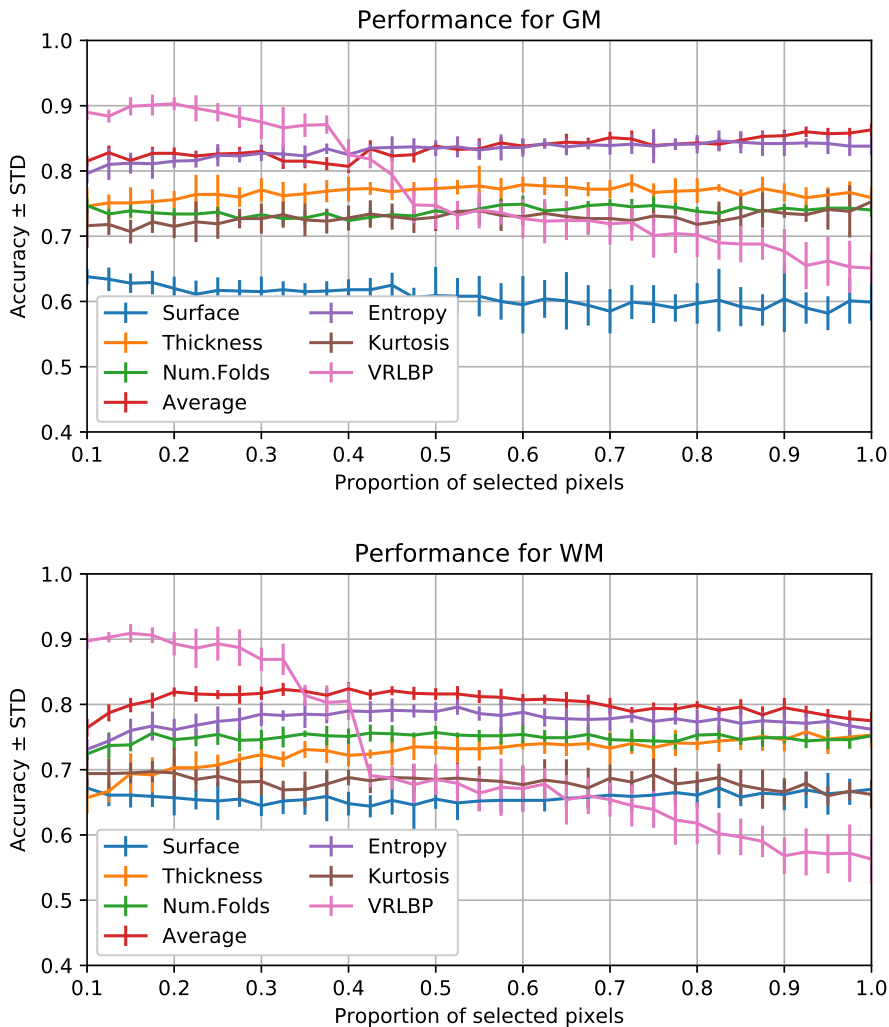


**Figure 6.12:** Performance for the different SBM approaches over the: a) Grey Matter and b) White Matter.

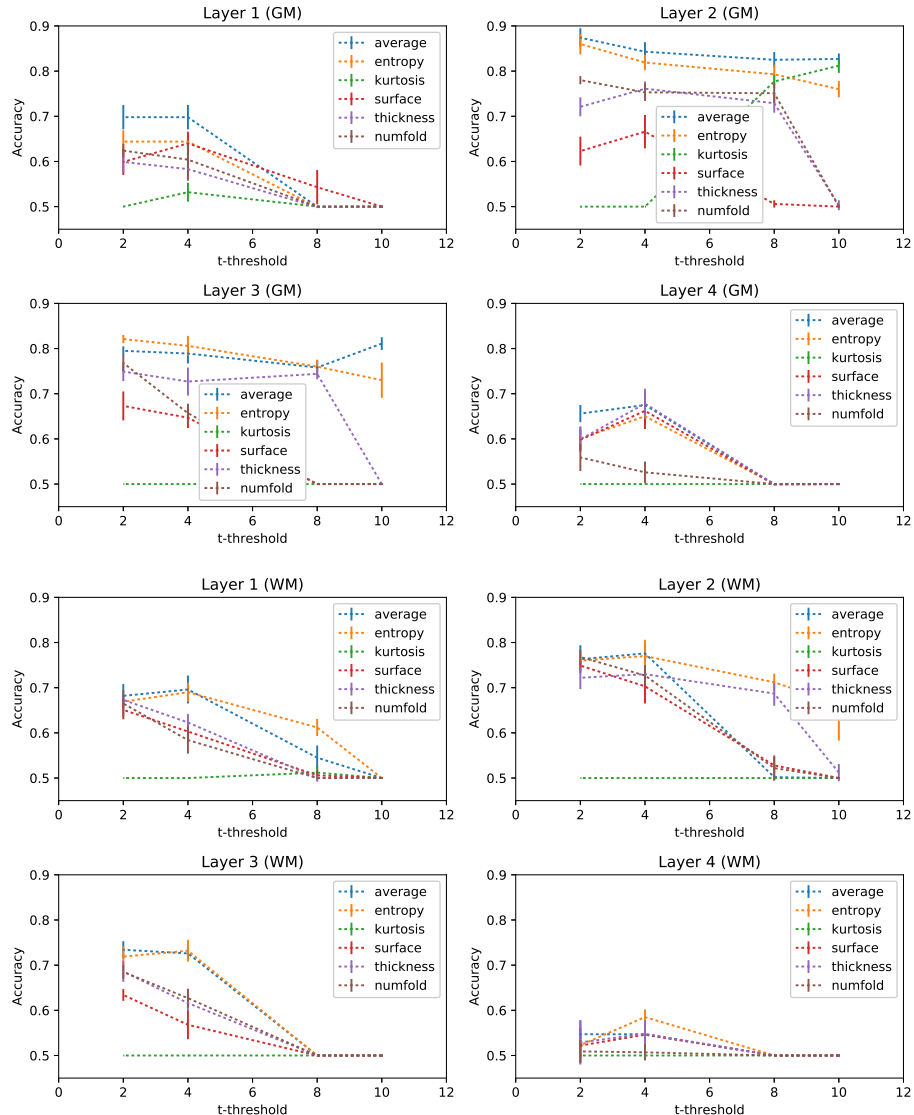


**Figure 6.13:** Performance for the different four-layered mappings over the: a) Grey Matter and b) White Matter at different levels of statistical significance.

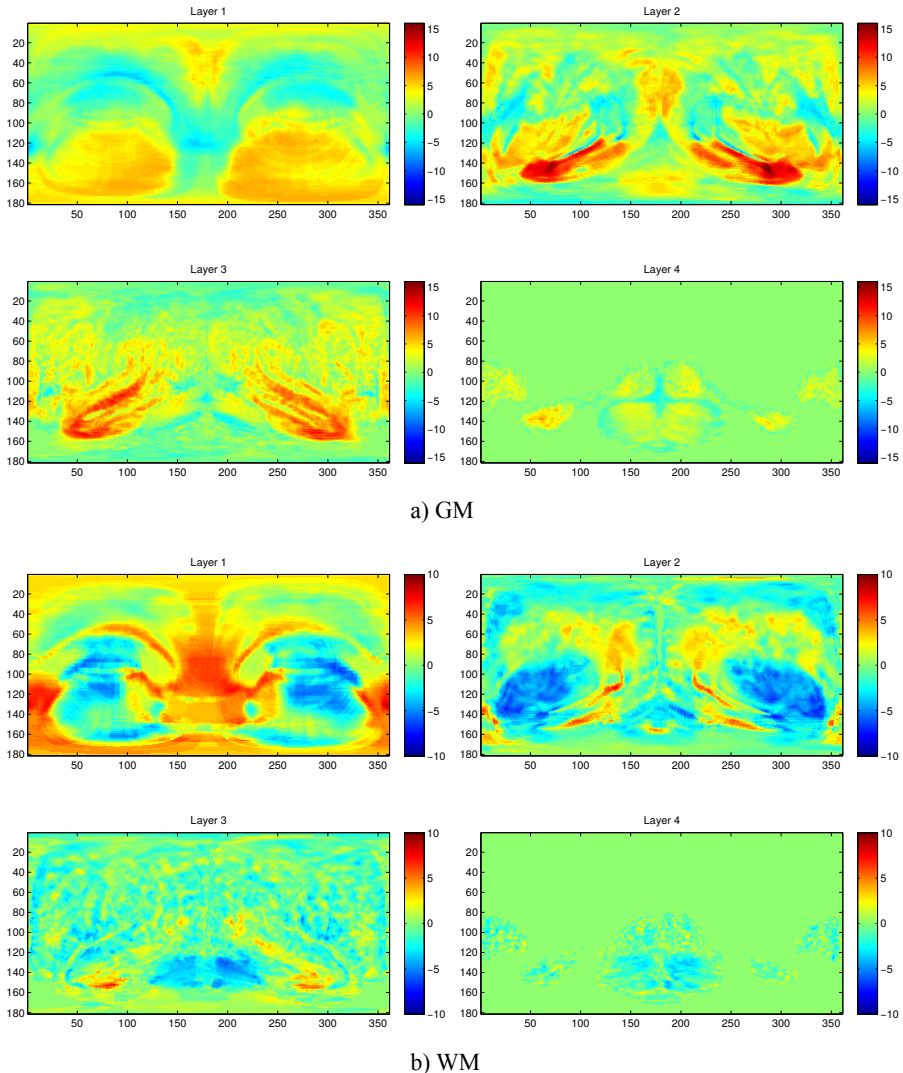


**Figure 6.14:** t-maps that present the level of statistical relevance in the AD vs. NC paradigm, for a four-layered average mapping over a) **GM** and b) **WM**.

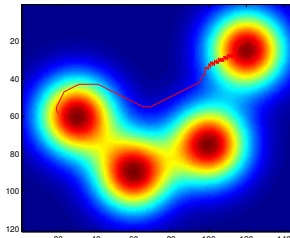


**Figure 6.15:** Path traced over a gaussian mixture distribution of 4 isotropic gaussian kernels.

temporal lobe (layer 3), where the values achieved by [CTL](#) subjects are much higher than those found in [AD](#). This could reveal atrophy in these organs, as it has been reported in the literature [24, 57] and will be discussed later. For [WM](#), we obtain large negative t-values in areas occupied by the rolandic operculum, heschl's gyri, putamen and globus pallidus, with positive values in parts of the hippocampus, and parts of the temporal lobe. Nevertheless, the most significant differences can be located in layer 1, at the borders between ventricles and thalamus, and the cuneus, precuneus and posterior cingulate gyrus, which have been reported in [82].

#### 6.4.3 Experiment 4: HMM on Synthetic Datasets

A demonstration of the ability of our [HMM](#) path tracing algorithm can be found in Figures 6.15 and 6.16. In Fig. 6.15, the path tracing algorithm has been tested over a synthesized gaussian mixture probability density function using four isotropic gaussian kernels. The initial point was located at  $\mathbf{p}_0 = (120, 20)$  and the attractor at  $\mathbf{p}_N = (20, 60)$ . The resulting path maximizes both the orientation of the path (towards  $\mathbf{p}_N$ ) and the minimum change in the intensity values, which is specially visible in the last nodes of the path, where it approaches  $\mathbf{p}_N$  surrounding the nearby kernel. In this case, the chosen L<sub>2</sub>-norm of the support ball has been  $r = 3$ .

The algorithm has been tested on a three-dimensional, helix-shaped point distribution as well (Fig. 6.16). The tracing algorithm needs per-voxel intensity (or probability) values, therefore we have estimated the probability distribution of the points as the number of points within each voxel over the total number of points. Using  $\mathbf{p}_0$  as the point with minimum  $z$  coordinate in the data distribution and  $\mathbf{p}_N$  the one with maximum  $z$ , the resulting path follows the data distribution consistently until it reaches the attractor.

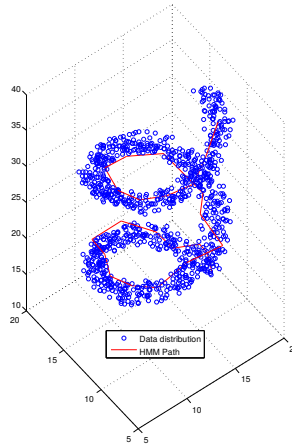


**Figure 6.16:** HMM path computed inside a density distribution defined by an helix.

Finally, we have tested the algorithm on a real world example, using a digital elevation model (DEM) of the Iberian Peninsula, generated by the LANDSAT SRTM30+ mission (see Fig. 6.17). We have tested a multiple path tracing by establishing sequentially  $p_0$  and  $p_N$  in ten cities. The resulting paths optimize both the distance and height variation, as well as resembling -in most cases- the roads that connect these cities in the real world. Given the dimensions of the image, in this case, the L<sub>2</sub>-norm of the support ball has been set to  $r = 30$ .

#### 6.4.4 Experiment 5: Feature Selection using HMM Paths

In this section, we present the results of the first experiment involving paths in MRI. To do so, we define a set of canonical paths that are computed on the DARTEL template. These DARTEL paths model the anatomy of a normal subject to whom all other images have been registered. This means that we have fixed the location of the nodes to the structural information of the template, and by extension, to the general anatomy of all images in the database. Therefore, we can characterize the structural differences by the intensity distribution –in other words, the tissue density– of the voxels at the path nodes. Comparing the intensity distribution found in controls to the one found in AD affected subjects is thus the first logical step to measure how these paths can distinguish the different classes.

To test the algorithm we use the  $180 \times 360 = 64800$  DARTEL paths computed in each spatial direction  $(\theta, \varphi)$ , with  $\varphi \in [0, 360]$  and  $\theta \in [-90, 90]$ , to select the intensities in the voxels that are placed at the nodes. The amount of voxels

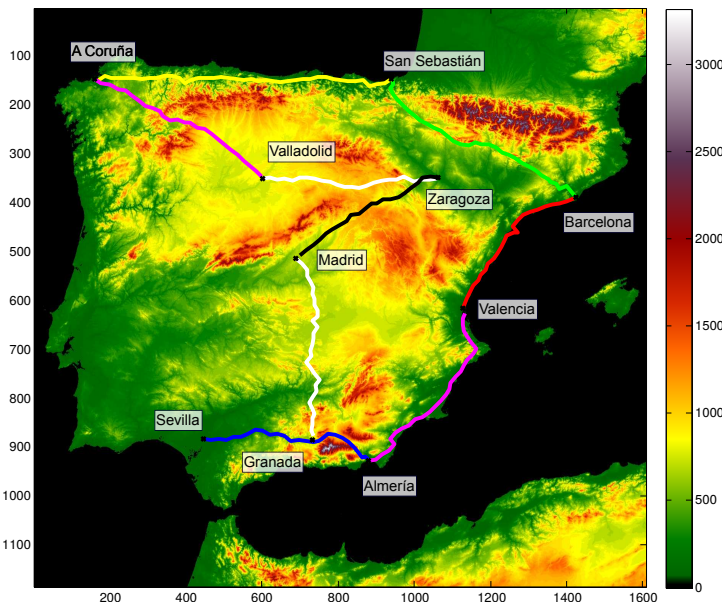


**Figure 6.17:** Simulation of the HMM-based path tracing over an Iberian Peninsula height map, interconnecting different cities.

selected ranges from 2 to several dozens. The set of selected intensities are used as features to train and test a SVM classifier. The accuracy reached by each path (using the aforementioned cross-validation strategy) is presented as colour information in Figure 6.18. The higher accuracy obtained using only one path is  $0.8028 \pm 0.0873$ , and corresponds to the light green paths that cross the temporal lobe.

It is interesting to question if the performance of this differential diagnosis could be improved using the information contained in more than one path at a time. To this end, we first take the higher accuracy (accuracy  $\geq 0.7$ ) paths according to the aforementioned performance and select all voxels located in the nodes of these paths. Additionally, we use a t-test over the set of voxels selected by these paths, to further reduce the set to those voxels that have significant ( $p < 0.05$ ) t-values ( $|t| > 1.96$ ). The performance values for the experiment involving all voxels in the paths (first row) and the one that uses only those significant voxels (second row) are presented in Table 6.2.

Finally, we mimic the procedure followed in the SBM article[6]. That is, we first compute the average, variance, entropy and kurtosis maps of each brain, but instead of using rectilinear paths, we use the DARTEL paths. Afterwards, all the features contained in these maps are used as an input to the SVM classifier. The performance results are shown in Table 6.3.

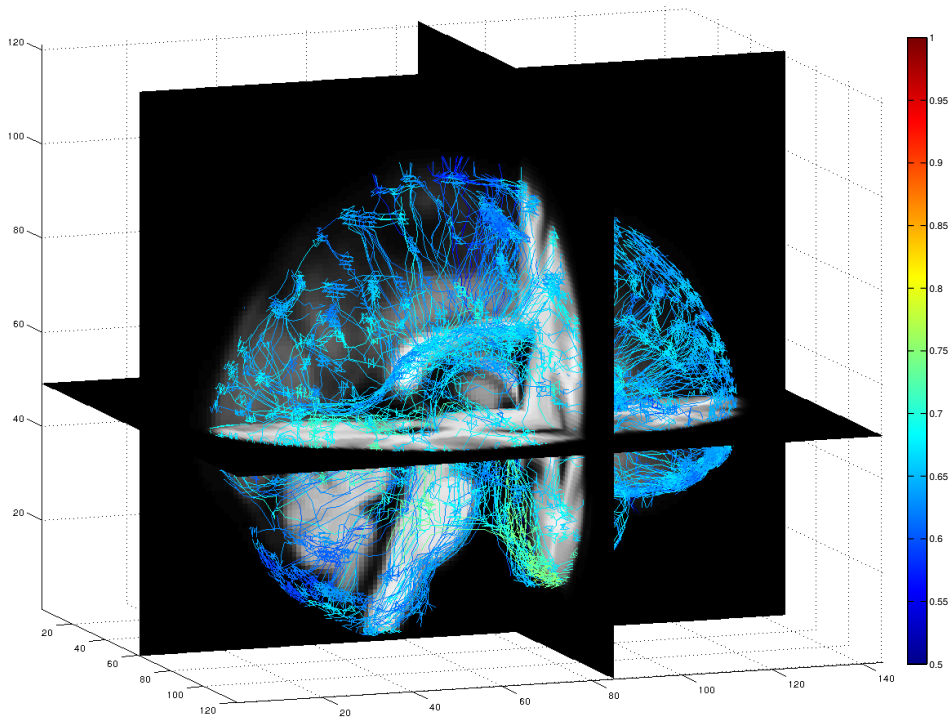


**Figure 6.18:** DARTEL paths computed in each direction ( $\theta, \varphi$ ). Each path's colour represent the accuracy in a differential diagnosis. Only one in every five paths are shown for clarity purposes.

Side	Accuracy	Sensitivity	Specificity
Both	$0.806 \pm 0.069$	$0.733 \pm 0.073$	$0.878 \pm 0.097$
Left	$0.769 \pm 0.035$	$0.717 \pm 0.061$	$0.822 \pm 0.057$
Right	$0.792 \pm 0.080$	$0.706 \pm 0.120$	$0.878 \pm 0.101$
Both	$0.828 \pm 0.054$	$0.794 \pm 0.095$	$0.861 \pm 0.039$
Left	$0.733 \pm 0.037$	$0.694 \pm 0.099$	$0.772 \pm 0.124$
Right	$0.781 \pm 0.085$	$0.711 \pm 0.122$	$0.850 \pm 0.083$

**Table 6.2:** Performance values ( $\pm SD$ ) for the selected paths as features, and using t-test to select the voxels.

Feature	Accuracy	Sensitivity	Specificity
Average	$0.594 \pm 0.062$	$0.661 \pm 0.121$	$0.528 \pm 0.106$
Variance	$0.750 \pm 0.064$	$0.633 \pm 0.131$	$0.867 \pm 0.102$
Entropy	$0.603 \pm 0.069$	$0.661 \pm 0.071$	$0.544 \pm 0.125$
Kurtosis	$0.756 \pm 0.105$	$0.733 \pm 0.165$	$0.778 \pm 0.150$

**Table 6.3:** Performance values ( $\pm SD$ ) for each of the measures used in the [SBM](#) article.

Feature	Accuracy	Sensitivity	Specificity
Contrast	$0.733 \pm 0.060$	$0.689 \pm 0.126$	$0.778 \pm 0.105$
Correlation	$0.672 \pm 0.068$	$0.672 \pm 0.112$	$0.672 \pm 0.100$
Dissimilarity	$0.711 \pm 0.085$	$0.678 \pm 0.110$	$0.744 \pm 0.102$
Energy	$0.689 \pm 0.061$	$0.700 \pm 0.115$	$0.678 \pm 0.073$
Entropy	$0.675 \pm 0.101$	$0.672 \pm 0.115$	$0.678 \pm 0.159$
Homogeneity	$0.697 \pm 0.058$	$0.700 \pm 0.115$	$0.694 \pm 0.106$
Difference Variance	$0.736 \pm 0.070$	$0.683 \pm 0.098$	$0.789 \pm 0.090$
Difference Entropy	$0.725 \pm 0.122$	$0.683 \pm 0.176$	$0.767 \pm 0.114$
IDN	$0.719 \pm 0.065$	$0.683 \pm 0.108$	$0.756 \pm 0.105$
IDMN	$0.717 \pm 0.076$	$0.678 \pm 0.125$	$0.756 \pm 0.084$

**Table 6.4:** Performance values ( $\pm SD$ ) for each of the 10 texture features.

#### 6.4.5 Experiment 6: Texture SBM Maps based on HMM Paths

The second experiment is intended to extract texture features from the DARTEL paths. With this approach, we obtain one single value per texture feature and path in the subjects, values that intrinsically contain information from their location in the path, in contrast to standard [SBM](#) measures. In the end, each subject will be characterized by a 2D,  $361 \times 181$  array of scalars, one for each texture feature applied to the paths. Performance values for the nine texture features maps from Section 6.3.1 are presented in Table 6.4.

The higher accuracy obtained by the texture maps is  $0.736 \pm 0.070$ , corresponding to Difference Variance. The performance values of the different texture features, all obtaining accuracies higher than 65% (most of them above 70%) reveal the discrimination abilities of these textures, although these values are not as good as those obtained using the voxel intensities or the [SBM](#) features.

#### 6.4.5.1 *Layered Extension*

#### 6.4.5.2 *VRLBP*

### 6.4.6 Classification Analysis

To obtain comparable performance metrics suitable to analyse the generalization capabilities of [SBM](#), in this section a number of classification results are presented. A baseline is established in Section [6.4.6.1](#) and then the performance of our maps, included the layered extension and VRLBP, is presented in Section [??](#).

#### 6.4.6.1 *Baseline - VAF*

In order to establish a baseline to assess the predictive ability of our maps, we will use the Voxels As Features ([VAF](#)) paradigm, described in [\[70\]](#). This approach uses the whole 3D [GM](#) or [WM](#) segmented MR images and then uses all voxels of the 3D images as features in the SVM classification, yielding the performance values shown in Table [6.5](#). The performance of the [SBM](#) maps will be compared to these.

Approach	Accuracy	Sensitivity	Specificity
<a href="#">VAF (GM)</a>	$0.768 \pm 0.011$	$0.752 \pm 0.016$	$0.785 \pm 0.016$
<a href="#">VAF (WM)</a>	$0.642 \pm 0.009$	$0.668 \pm 0.012$	$0.617 \pm 0.013$

**Table 6.5:** Performance values (Average  $\pm$  Standard Deviation) for the Voxels as Features approach in both [GM](#) and [WM](#) tissues.

## 6.5 Discussion

### 6.5.1 Spherical Brain Mapping

The structural changes in MR images during the progression of the Alzheimer's Disease are widely documented in the bibliography [\[han2006reliability, Fischl2004, 24, 47, 70, 82\]](#). According to our current knowledge, the neurodegeneration and posterior atrophy occurs mainly in the [GM](#) tissue, although significant changes are present also in [WM](#).

The mappings defined throughout Sections [6.2](#), [6.2.1](#) and [6.2.2](#) account for different properties of the tissues crossed by  $v_{\theta,\varphi}$ . As it can be seen in Figure [6.19](#), our mappings show in general a higher performance when using the

**GM** tissue, which is consistent with the literature. There are some exceptions, however, being the clearest the VRLBP, and, to a lesser extent, the number of folds and surface. The different mappings and their utility will be described in the following paragraphs.

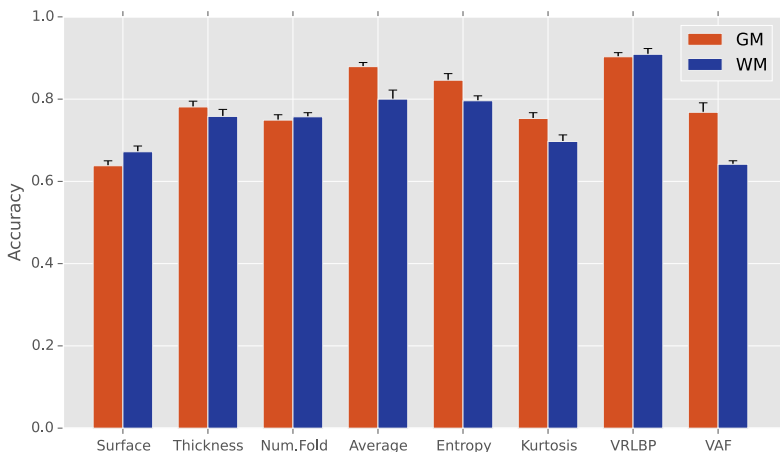


**Figure 6.19:** Performance at the operation point for the different mappings over the Grey Matter and White Matter, compared with the performance of **VAF**.

The first three approaches, Surface, Thickness and Number of Folds are easily interpreted, as they intend to represent the surface of the tissue by mapping the distance between the centre of the image and the last voxel, the thickness of the tissue, and a measure of the complexity of the different sulci and gyri.

Surface and Thickness are highly related to other measures provided by widely-used software. However, as they are related to our more general **SBM** description, their performance is poor, specially in the case of the Surface mapping. As it can be seen in Fig. 6.3, and later in the t-maps at Fig. 6.10, the detail of the surface map lacks higher detail, specially due to the superposing gyri and sulci. These superposition occur to a lesser extent in **WM** tissue, and this is probably why this technique obtains higher performance in **WM** than in **GM**.

As for the case of Thickness, although similar, it gathers much more information than the surface, without achieving, however, the level of detail of the cortical thickness measures provided by Freesurfer [Fischl2004] or other software. Nevertheless, cortical thickness it is a descriptive, widely accepted as a measure of neurodegeneration in Alzheimer's Disease in the literature [han2006reliability, Fischl2004], and its measures might be relevant for a subsequent analysis.

Number of Folds, however, is intended to model the complexity of the cerebral cortex, and therefore, it is of far more use in the case of GM than in the WM. This can be easily checked when looking at the maps obtained for both GM and WM in Figure 6.3.

The last three measures described in Section 6.2 are statistical values that describe the variability of the sampling set  $V_{\theta,\varphi}$ . It would be reasonable to expect the better performance to be linked to the mapping that better models the tissue atrophy.

This is the case of the average of these intensities, which can be interpreted as the total amount of tissue, being therefore a good measure of the level of brain atrophy in each direction  $(\theta, \varphi)$ . The average maps show the best performance of all the measures proposed in Section 6.2, and is higher in GM than in WM. This is consistent with the literature, as atrophy mainly occurs in GM tissues.

Entropy is a more complex statistical concept that comes from information theory, but is usually related to the amount of information, or in other words, the “randomness” of a source. In our particular case it could be interpreted as a measure of texture, that is, the grey-level variability in the direction of  $v_{\theta,\varphi}$ . These maps perform very similar to the average ones in both GM and WM, suggesting that the entropy accounts for the tissue density as well.

The last mapping defined, Kurtosis, is a fourth-order statistic, often interpreted as the peakedness (width of peak) of a probability distribution. In our context, it is related to the sharpness of the changes in the direction of  $v_{\theta,\varphi}$ , and thus is related to the number of folds. As in the case of the latter, the Kurtosis performs poorly in both types of tissues, probably because they are measures that are not as directly related to atrophy as other measures such as average, entropy or thickness.

The last of the single measures proposed in this work is the Volumetric Radial LBP defined in Section 6.2.2. It is a measure of the texture not only in the direction of  $v_{\theta,\varphi}$ , but also in the neighbourhood of the mapping vector. Therefore, it is not strange that it obtains the best performance of the whole work, yielding accuracy results above 0.9 for both GM and WM tissues.

This could seem counter-intuitive, as the t-maps for this technique, presented in Fig. 6.11, show small regions of high significance, when compared to the measures in Sec. 6.2. Yet, despite its size, it performs fairly well with a relatively small amount of data. It is probably due to the nature of VRLBP, and the areas highlighted in Fig. 6.11 probably correspond to the texture changes associated to the loss of tissue in the Hippocampus.

As for the layered extension, which might seem a powerful method to add detail to the mappings, obtains however similar performance to the methodology above. It seems that the amount of information that can be obtained by each

measure does not depend on the number of layers, and accordingly, its benefits are only related to visualization. In this case, best values are obtained in layer 2, which is consistent to the presence of some organs, specially the Hippocampus.

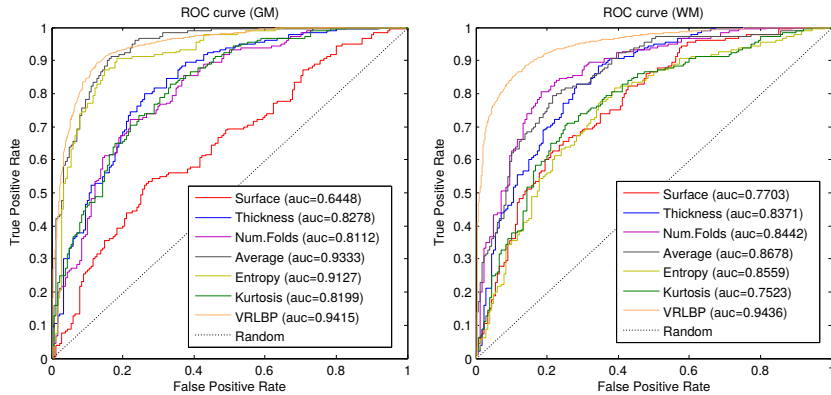


**Figure 6.20:** ROC curves of the different mappings for the **GM** and **WM** tissues.

Finally, in order to have another look at the performance of our mappings, the ROC curves of each type are presented in Figure 6.20. There we can see how the VRLBP approach outperforms all the other measures, specially in the case of **WM** tissue. In **GM**, Average and Entropy present values really close to VRLBP, as expected. Conversely, the poorest performance is achieved by the Kurtosis and Surface mappings, however the Surface performs better in **WM** than in **GM**. These results confirm the performance values presented in Table 6.1 and Figure 6.12, making our proposed mapping framework a reasonable choice for obtaining both a visual interpretation of otherwise hidden features and a significant dimensionality reduction.

It is important to note that our Spherical Brain Mapping defines a whole framework that can be easily extended with different sampling strategies. This is the case of the layered extension and the helical sampling in VRLBP, but they are only two examples of what can be done. Since our simplest approach implies a computation of a value from a vector of intensities, measures used to describe time-course data could be added to complete and highlight different properties of the tissues. In this context, high-order statistics [Zhou2008], as well as spectral measures [Locatelli1998] have been successfully applied to analyse electroencephalogram (EEG) signals, and could be therefore applied here to bring different structural properties of the images into focus. Additionally, our mapping method is potentially applicable to other imaging modalities, such as PET and SPECT, where the structural information is sometimes lost [IAIlan2010, Ram'irez2009]. Our technique does not need the use of complex co-registering of MRI and functional imaging to locate cerebral structures, as it rely only in

their angle and depth. Moreover, in the case of Diffusion Tensor Imaging (DTI), which has proven itself as a good tool for the diagnosis of Alzheimer's Disease [Grana2011, Medina2008], SBM could be modified to replace  $v_{\theta,\varphi}$  with each tract, and subsequently project a given feature, resulting in a summary of the tract's behaviour in a single two-dimensional image.

### 6.5.2 Paths via HMM

In this work we propose a new path tracing algorithm based on Hidden Markov Models used to trace similar intensity paths inside the brain. The paths are meant to be used as a feature extraction tool in the SBM framework either by selecting voxels or computing features. We have performed several experiments to evaluate these approaches in a differential diagnosis of AD using MRI brain images.

Our paths are defined so that they construct a minimum intensity variation path starting at the AC and oriented in a general direction set by the spherical coordinate pair  $(\theta, \varphi)$ . As commented before, the AC is the obvious starting point, given its privileged position in the middle of the left and right hemispheres. A different starting point will reveal suboptimal, stopping at disconnected regions such as the ventricles, and yielding incomplete paths.

The paths adapt to the intensity changes in a certain direction in the brain, modelling grey level connectivity in all spherical directions. Since grey level is directly related to tissue density, we can assume that the outcome follows smooth, same-density paths that start in white matter and progressively transition to grey matter in a specific direction. Therefore, they are not functional connectivity maps like Diffusion Tensor Imaging (DTI), which have been used as well in the diagnosis of AD[Grana2011, Medina2008]. While DTI fibers are the result of a tensor processing over diffusion images that quantify the water molecule motion -in both direction and average magnitude- at the voxel level, our HMM paths only characterize grey level connectivity in static MRI images, and are meant to be used for feature selection.

Our first experiment uses HMM paths computed on the DARTEL template to describe how the intensity of the set of voxels corresponding to a certain path can be used as discriminant features in a SVM classifier. The differences in the distribution of intensities between controls and AD affected subjects are used to identify structural changes in AD. Fig. 6.21 depicts the paths that achieved best performance (accuracy higher than 0.75) in this differential diagnosis, superimposed to some structures rendered from the Automated Anatomical Labeling (AAL) brain atlas[Tzourio-Mazoyer2002].

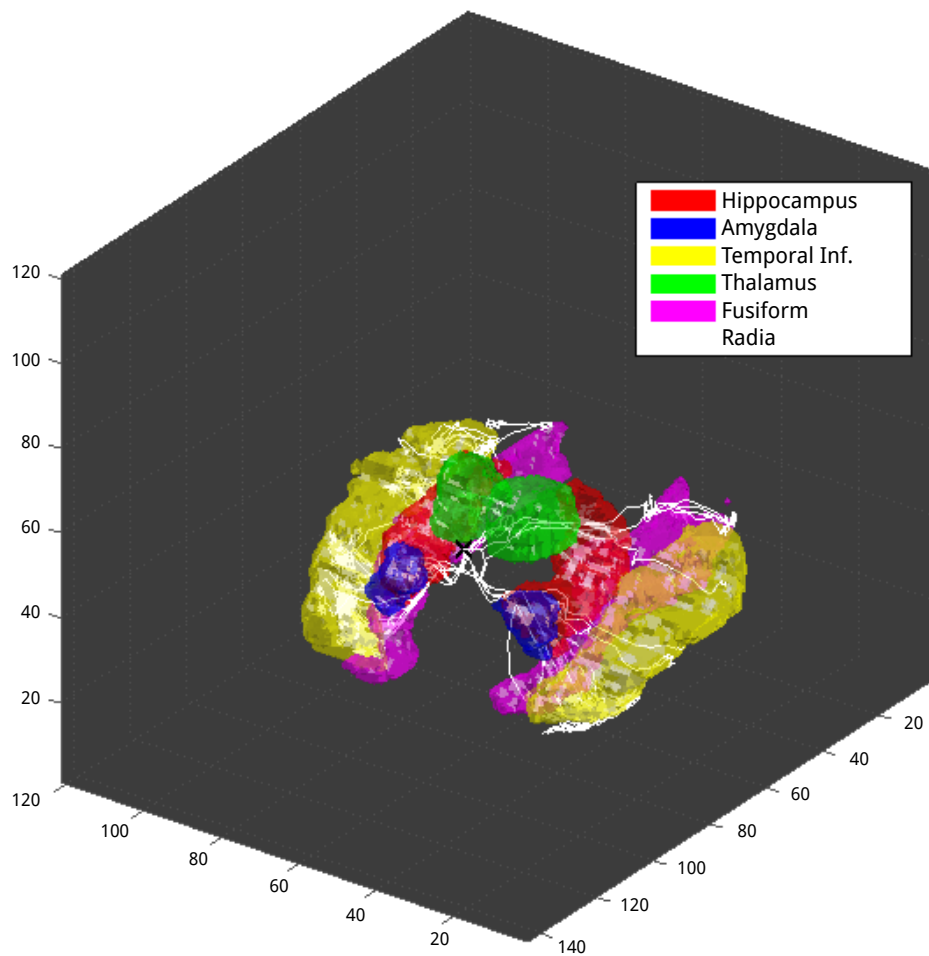


**Figure 6.21:** Paths that obtain more than 75% accuracy, and a three-dimensional representation of the structures crossed by them.

The paths that obtained higher accuracy are those that cross structures such as the Hippocampus, Amygdala, Thalamus, Fusiform and Inferior Temporal Gyrus. Particularly, grey matter loss in the Hippocampus has been described in the NINCDS-ADRDA criteria for AD diagnosis[57] and is widely accepted[chan2001pattern, Jong2008, 82]. Furthermore, the evidence suggest that atrophy affects the surrounding structures (Amygdala, Parahippocampal and Fusiform Gyrus) as well[chan2001pa, 82]. Some studies have found significant atrophy in the Thalamus and Putamen in early AD[Jong2008] as well. Generally, in advanced AD, most of the neocortex and grey matter suffer from atrophy[chan2001patterns, Jong2008, 82], which explains why most of the paths that involve the neocortex in Fig. 6.18 obtain accuracy rates around 0.7.

A number of feature maps have been computed as well. These are the result of applying some of the SBM measures to the voxels selected by the HMM paths. Variance and kurtosis have been proved as the most discriminative maps (with accuracy higher than 0.7). This is coherent with the definition of the paths, where the intensity transitions are minimal. Therefore, average would be the less discriminative in this case, being higher order statistics such as variance or more representative of the tissue density distribution of each class.

Regarding texture analysis, we have again discriminative features (with accuracy that surpass the 70%) yet not very powerful. This situation might be due to the definition of the paths as minimum intensity variation paths, being the textural changes along the path minimal.

However the real utility of these texture features could be in its application to longitudinal studies, since texture can be related to evolution of the disease[12]. It is very convenient to use a scalar to characterize a measure (in our case, texture features) in each direction. The texture obtained in each session can be used to construct a function of neurodegeneration that allows the exploration of the different stages of the disease as the changes in the brain texture along the time within a single patient.

Table 6.6 presents some of the best results of our methodology involving HMM paths in this order: the performance of a single path and using the selected paths as features (Section ??), the performance of using projected maps (in this case, variance and kurtosis) like in the SBM paper (Section ??) and the results of computing texture maps using radial GLCM and Haralick Texture Features (Section ??). It is compared with the methods using in the SBM paper[6], the SBM-VRLBP[11], the Voxels As Features (VAF)[70] algorithm and different approaches used in the ADNI database and involving SVM classifiers such as the LVQ-SVM[Ortiz2013] or Spatial Component Analysis (SCA)[Illan2014].

VAF is often used as a baseline when comparing different methodology, as it has been described as a good estimator of the accuracy obtained by means of

Feature	Accuracy	Sensitivity	Specificity
Paths	$0.806 \pm 0.069$	$0.733 \pm 0.073$	$0.878 \pm 0.097$
Selected Paths	$0.828 \pm 0.054$	$0.794 \pm 0.095$	$0.861 \pm 0.039$
Variance	$0.750 \pm 0.064$	$0.633 \pm 0.131$	$0.867 \pm 0.102$
Kurtosis	$0.756 \pm 0.105$	$0.733 \pm 0.165$	$0.778 \pm 0.150$
Texture (Difference Variance)	$0.736 \pm 0.070$	$0.683 \pm 0.098$	$0.789 \pm 0.090$
<b>VAF</b>	$0.768 \pm 0.011$	$0.752 \pm 0.016$	$0.785 \pm 0.016$
<b>SBM-average (GM)</b>	$0.879 \pm 0.005$	$0.897 \pm 0.006$	$0.861 \pm 0.006$
<b>SBM-average (WM)</b>	$0.800 \pm 0.011$	$0.802 \pm 0.013$	$0.798 \pm 0.009$
<b>SBM-VRLBP (GM)</b>	$0.903 \pm 0.010$	$0.890 \pm 0.012$	$0.916 \pm 0.018$
<b>SBM-VRLBP (WM)</b>	$0.909 \pm 0.014$	$0.899 \pm 0.028$	$0.919 \pm 0.018$
LVQ-SVM (GM)	$0.869 \pm 0.101$	$0.822 \pm 0.120$	$0.890 \pm 0.102$
SCA (GM)	$0.880 \pm 0.0^*$	$0.926 \pm 0.0^*$	$0.845 \pm 0.0^*$
SCA (WM)	$0.808 \pm 0.0^*$	$0.817 \pm 0.0^*$	$0.800 \pm 0.0^*$

\* SCA used leave-one-out cross-validation. SD is 0.

**Table 6.6:** Comparison between our algorithm performance values (best values for selected voxels in all paths and texture features) ( $\pm$ SD) and other methods in the bibliography

visual analysis [70]. As we commented before, the raw voxel intensities selected by our DARTEL paths achieve higher accuracy than statistical or texture features, and it is the only strategy that outperforms VAF. Texture and statistical features obtain poorer, although still good, performance (around 75% accuracy). When compared to other methods, the difference is greater, although inside the range of 1 SD. Most of the SBM features proposed in [6] perform better than our DARTEL paths, and the case of [11] even surpass the barrier of 90% accuracy. However, there is a significant difference with these approaches, and it is that these measures used segmented GM and WM images, instead of using the whole MRI. Segmentation, thus, enhances the detection and extraction of features from the images, whereas the tracing of paths over the whole images is a more complex operation. When compared to LVQ-SVM or SCA, the difference in performance is even smaller and still inside the range of 1 SD, which gives us an idea of the ability of our methodology to detect patterns with a significant feature reduction.

Finally, one might argue if a different approach to the path tracing, such as tracing the set of paths in each subject individually might be of use. This strategy would still characterize the individual brain structure; however the way this structure is defined would be different: the spatial location of the nodes and

topology of the paths instead of the intensity distribution. Given the time our algorithm takes to model one single MRI (around 2 hours) it can be extraordinarily computationally expensive, although faster than other methodology like DTI fiber tracing or Freesurfer surface extraction. Consequently, it would be an interesting option to explore in future works.



**Part III**

**INCREASING THE SAMPLE SIZE**



# 7

## SIGNIFICANCE WEIGHTED PRINCIPAL COMPONENT ANALYSIS

Multicentre studies with structural (sMRI) and functional Magnetic Resonance Imaging (fMRI) are increasingly common, allowing for recruitment of larger samples in shorter periods of time. However, the use of images acquired at different sites still poses a major challenge. In addition to logistical difficulties, such as regulatory approvals and data protection, a number of technical and methodological issues can potentially affect the resulting maps, introducing undesired intensity and geometric variance. This issue has been addressed in other neurological conditions, such as Alzheimer's Disease (Jovicich, et al., 2006; Stonnington, et al., 2008), where group differences are well known, and demonstrating that the impact of a correction for site on the resulting neurobiological differences is relatively small. However, these effects have a stronger impact in psychiatric conditions where the atypical radiological signs on MRI are often subtle and require large samples of patients to observe on-average differences relative to control samples. Recent meta-analyses point to differences being inconsistently reported in schizophrenia (Friedman and Glover, 2006; Turner, et al., 2013), psychosis (Clementz, et al., 2016; Wang, et al., 2015), and [ASD](#) (using the multi-centre ABIDE database) [15]

These inconsistencies can arise from a variety of variance sources, ranging from the multi-level (phenotypic, neurobiological, and etiological) heterogeneities of the conditions to technical issues that include differences in scanner make, model, manufacturer, static field strength, field inhomogeneities, slew rates and image reconstruction (Van Horn and Toga, 2009), as well as acquisition problems such as within-acquisition participant head motion. Field inhomogeneities are a source of misinterpretation of the data even when the same MRI system manufacturer and model are used (Van Horn and Toga, 2009). Furthermore, results in (Pearlson, 2009) demonstrate that a single scanner can change with time, which makes some widely used strategies, for example collecting controls first and patients later, a flawed approach. Recent neuroimaging research on [ASD](#) (Haar, et al., 2014) has shown that, while analyses performed on a particular database (acquired on a single platform) could yield coherent regions, the atypical structures are often inconsistent across the wider literature using different databases. Therefore, new methodologies focused on reducing multi-

site variance may be potentially helpful in increasing the power to identify the characteristic neurobiological signature of autism, should there be one.

[1]

## 7.1 Significance Weighted Principal Component Analysis

The Significance Weighted Principal Component Analysis ([SWPCA](#)) is an algorithm to reduce, in this case, undesired intensity variance introduced by multi-site image acquisition. [SWPCA](#) takes any dataset of pre-processed images, spatially normalized, and decomposes them into their variance components to then provide a corrected dataset where these undesired variance components have been reduced. To do so, [PCA](#) was applied to each modality in turn to obtain the component scores and component loadings. Since [PCA](#) is a data-driven approach, it was only used to decompose the source images, and after this procedure, a one-way [ANOVA](#) estimated the relation between each variance component and a given categorical variable, in our case, the acquisition site. The between-site variability in the variance component was then identified by its corresponding *p*-value. Finally, these *p*-values were transformed into a weighting matrix  $\Lambda$  that weighted the influence of each variance component in a final [PCA](#) reconstruction of the corrected maps. The procedure is summarized in Figure [7.1](#).

### 7.1.1 Principal Component Analysis

The first step in the [SWPCA](#) algorithm was to perform a [PCA](#) decomposition of the dataset into a set of orthogonal components that model the variance present in the images.

[PCA](#) is a statistical procedure that uses an orthogonal transformation to convert a set of observations  $\mathbf{X}$  of possibly correlated variables, where  $\mathbf{X}$  is a  $K \times N$  matrix, with  $K$  participants (in this case, with one image per participant) and  $N$  the number of voxels, into a set of  $N$  linearly uncorrelated variables called Principal Components (PC, also known as component loadings or the mixing matrix)  $\mathbf{W}$  of size  $N \times N$  whose linear combination using a vector of component scores  $s_K$  can perfectly recompose each image. The set of these component scores  $\mathbf{S}$  (size  $K \times N$ ) was estimated as:

$$\mathbf{S} = \mathbf{X}\mathbf{W}^\top \quad (7.1)$$

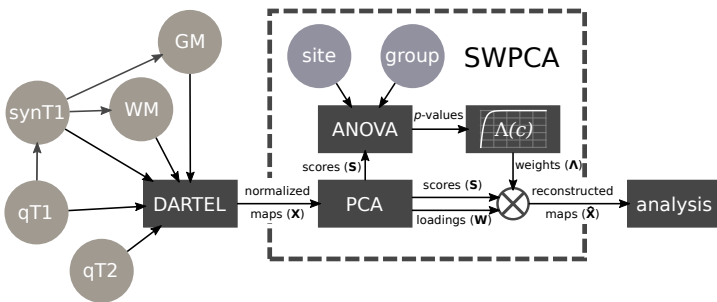


**Figure 7.1:** Summary of the [SWPCA](#) algorithm, along with its context in the pipeline used in this article. Circles represent the input data, both images (green shading) and class (group and acquisition site, purple shading). Rectangles represent the different procedures applied, comprising the DARTEL normalization and registration, the different steps contained in [SWPCA](#), [ANOVA](#) and obtaining the weighting function  $\Lambda(c)$ - and the subsequent analysis.

This transformation computes a sequence of PCs, maximally explaining the variability of the data while maintaining orthogonality between components. [PCA](#) was computed using Singular Value Decomposition ([SVD](#)):

$$\mathbf{X} = \mathbf{U}\Sigma\mathbf{V}^* \quad (7.2)$$

where  $\mathbf{U}$  is an  $K \times K$  orthogonal matrix,  $\Sigma$  is a  $K \times N$  diagonal matrix with non-negative real numbers on the diagonal, and the  $N \times N$  unitary matrix  $\mathbf{V}^*$  denotes the conjugate transpose of the  $N \times N$  unitary matrix  $\mathbf{V}$ . With this decomposition both the component scores and estimates of the set of components loadings  $\mathbf{W}$  were obtained. In this work the truncated form of [SVD](#) was used such that only the first  $C$  components were considered, where most of the variability of the data was concentrated:

$$\mathbf{S}_C = \mathbf{U}_C \Sigma_C = \mathbf{X} \mathbf{W}_C \quad (7.3)$$

where  $\mathbf{S}_C$  is the set of component scores using the first  $C$  components (size  $K \times C$ ). To achieve reasonable performance with minimal information loss, it was assumed that the number of components was the same as the number of images,  $C = K$ . Thus, a partial reconstruction of the original signal could be undertaken:

$$\hat{\mathbf{X}} = \mathbf{S}_C \mathbf{A}_C \quad (7.4)$$

where  $\mathbf{A}_C$  is the pseudoinverse of the truncated matrix of component loadings  $\mathbf{W}_C$ , and  $\hat{\mathbf{X}}$  is the reconstructed set of images.

### 7.1.2 One-Way Analysis of Variance

The estimated PCs effectively model the variability of the image dataset. The next step was to assess each PC as a source of inter-site variance with one-way Analysis Of Variance ([ANOVA](#)). [ANOVA](#) estimates the F-statistic, defined as the ratio between the estimated variance within groups and the variance between groups:

$$F = \frac{MS_{within}}{MS_{between}} = \frac{SS_{within}/(G - 1)}{SS_{between}/(K - G)} = \frac{\sum_i n_i (\bar{Y}_i - \bar{Y})^2 / (G - 1)}{\sum_{ij} (Y_{ij} - \bar{Y}_i)^2 / (K - G)} \quad (7.5)$$

Where  $MS_{within}$  and  $MS_{between}$  are the mean squares within- and between-groups respectively,  $G$  is the number of separate groups (in our case, two),  $\bar{Y}$  is the sample mean of a certain feature (in our case, the sample mean of all  $K$  values of a given component score),  $\bar{Y}_i$  is the sample mean of the features belonging to group  $i = 1 \dots G$ ,  $Y_{ij}$  is the  $j_{th}$  observation of a feature belonging to group  $i$  and  $n_i$  is the number of participants in the  $i_{th}$  group. The F-distribution allows an easy computation of p-values, given the number of groups and degrees of freedom. The F-statistic and p-values were computed independently for each component score and acquisition site, and then used in the [SWPCA](#) algorithm.

### 7.1.3 Weighting Function

To obtain a set of corrected maps, a new signal matrix of all maps of the same modality,  $\hat{X}$ , was estimated with the influence of the PCs with variance related to acquisition site, assessed via the p-values, reduced. To do so, equation [7.4](#) was modified to include a square matrix  $\Lambda$  (dimension  $C \times C$ ) whose diagonal contains a weight  $\lambda_c$  for each component that depends on its p-value; that is,

$$\hat{X} = S \Lambda A \quad (7.6)$$

The computation of each  $\lambda_c$ , for each component, was performed using the Laplace distribution, modified so that the weights were on the interval  $[0, 1]$ :

$$\Lambda_c(p_c, p_{th}) = 1 - e^{\frac{-p_c}{p_{th}}} \quad \forall p_c \in [0, 1] \quad (7.7)$$

where  $p_c$  is the statistical significance of the  $c_{th}$  component with respect to the acquisition site and  $p_{th}$  is the statistical threshold for significance; that is,  $p_{th}=0.05$ . A plot of the univariate weighting function  $\Lambda_c(p_c, p_{th})$  can be found in Figure [7.2](#). This weighting ensured that most of the components of variance that are not related to the acquisition site are kept unchanged, while at the same



**Figure 7.2:** Weighting function  $\Lambda_c(p_c, p_{th})$  used in SWPCA.

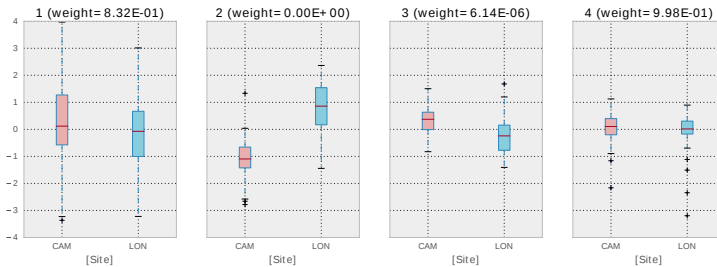


**Figure 7.3:** Box-plot of the distribution of the component scores at each site of the AIMS-MRI dataset (see Sections 7.2 and A.1.2) in the four first components. We assume that bigger differences between distributions imply a bigger influence of the acquisition site on the portion of variance modelled by that component and therefore, to parse out those differences, the resulting weight will be smaller.

time it strongly reduces the influence of components with p-values less than the threshold.

This procedure is illustrated in Figure 7.3, where a boxplot of the distribution of the first four principal component scores is shown. Since we have assumed that substantial differences imply a bigger influence of the acquisition site on the portion of variance modelled by that component, the resulting weight is reduced, and the contribution of that component to the reconstructed signal will be smaller. After computing all weights, most of the sources that are related to the acquisition site (for example, the second and third components) have been parsed out while keeping all other sources of variance.

## 7.2 Results for AIMS-MRI Dataset

To validate the effects of the [SWPCA](#) algorithm on the inter-site variance, experiments were undertaken to assess the reduction of the undesired site variance in the original datasets, and its impact on the between-group signal. Two kind of analysis were performed: a characterization of voxel-wise differences, and a classification analysis.

Voxel-wise differences between groups were characterized using Voxel Based Morphometry ([VBM](#)) [86], comprising preprocessing (registration, smoothing) and mass-univariate t-test on the smoothed maps from each modality. [SWPCA](#) is included (when needed) in this pipeline as a plug in, after the smoothing and before the computation of the test. Permutation testing assessed the significance of the relationship between the tested and target variables. A max-type procedure was used to obtain family-wise, whole-brain corrected  $p$ -values (Freedman and Lane, 1983). Additionally, a Component Based Morphometry ([CBM](#)), based on Source Based Morphometry ([SBM](#)) [[xu2009source](#)] was used. This procedure provided Z-maps for visual inspection comparable to those obtained in [VBM](#), by selecting component loadings  $\mathbf{W}$ , scaling them to unit standard deviation and weighting their contribution to the final map with their statistical significance, computed using the same permutation inference as in [VBM](#).

A classification analysis was undertaken using a common classification pipeline (Khedher, et al., 2015; López, et al., 2009) consisting of preprocessing, feature extraction and classification. [SWPCA](#) is used as a plug-in here as well, after the preprocessing and before the feature extraction step. We used [PCA](#) on the images for feature reduction and a Support Vector Classifier ([SVC](#)) with linear kernel, as implemented in LIBSVM [35], to classify the component scores in both corrected and uncorrected datasets (i.e. with and without [SWPCA](#)).

The classification was validated using stratified 10-fold cross-validation [[Kohavi1995a](#)]. In brief, 9 subsets of the dataset were used for extraction of the PCs and training of the classifier with the remaining subset used for testing. This procedure was repeated for each subset, repeated 10 times to avoid possible bias and random effects of the partitions. The average and standard deviation of the accuracy (acc), sensitivity (sens) and specificity (spec) values for each repetition were recorded.

For each modality independently, the following experiments were performed:

- **Experiment 1:** To demonstrate the ability of the [SWPCA](#) algorithm to reduce undesired effects due to acquisition site, the [PCA](#) + [SVC](#) pipeline was applied to the datasets labelled by acquisition site. Classification accuracy was compared to datasets with and without [SWPCA](#). [VBM](#) was then applied to identify the spatial location of the between-site differences. This

was undertaken on the whole database (ALL), and subgroups containing only **ASD** or **ASD** participants.

- **Experiment 2:** The discrimination ability of each modality, acquired at different sites was assessed by classification performance of individuals from London (LON) and Cambridge (CAM) was separately assessed, using group (**ASD** and **CTL**) as the labels.
- **Experiment 3:** To assess the impact of **SWPCA** on the datasets when characterizing the differences between **ASD** and **CTL** groups, the classification pipeline comprising **PCA + SVC**, as well as **VBM** and **CBM**, were applied to all participants with group as the labels.

### 7.2.1 Experiment 1: Effect of Acquisition Site

The first experiment was to demonstrate the ability of SWPCA to reduce the intensity variance related to acquisition site. To do so, we first performed a **VBM** analysis in all five modalities (**qT<sub>1</sub>**, **qT<sub>2</sub>**, simulated T<sub>1</sub> - weighted Inversion Recovery (**synT<sub>1</sub>**), **GM** and **WM**) separately, with the uncorrected (without applying SWPCA) and the corrected (after applying SWPCA) maps, using the acquisition site as labels.

To illustrate where the sources of variance of the acquisition sites are located, Figure 7.4 shows a brain t-map of significant ( $p < 0.01, |t| > 2.57$ ) **GM** and **WM** between-site differences. The biggest reductions in variance were found in **qT<sub>1</sub>** and **synT<sub>1</sub>** maps, where high variability between acquisition sites, especially in the right hemisphere, was substantially reduced after the application of SWPCA. The reduction in the **qT<sub>2</sub>**, **GM** and **WM** maps was smaller, although noticeable.

To quantify the impact of this variance reduction on the between-groups effects, the classification analysis was undertaken. Higher accuracy values imply that the maps contain site-related patterns that were significant, whereas accuracy close to 0.5 indicates that the site-related variance was low. The test was applied to ALL, and also to the ASD and CTL subgroups. The classification results are presented in Table 7.1.

Performance results indicate clear advantages of using SWPCA, in particular in the case of **qT<sub>1</sub>** and **synT<sub>1</sub>** which were associated with strong site-dependent variance. These results are also consistent with the reduction of significant between-group areas observed in Figure 7.4.

The between-site differences were smaller for **GM** and **WM** maps, possibly due their reduced sensitivity. Since fractional occupancy values are abstract, unitless values derived from each image they are less influenced by the acquisition



**Figure 7.4:** Brain t-map (VBM) of significant ( $p < 0.01, |t| > 2.57$ ) GM and WM between-group differences using **qT<sub>1</sub>**, **qT<sub>2</sub>**, **synT<sub>1</sub>**, **GM** and **WM** modalities after applying **SWPCA** to remove site effects.

site effects. For [qT<sub>2</sub>](#) maps, the site-related differences were greater for the CTL participants than ASD where, according to the classification accuracy, they were nearly indistinguishable. Acquisition site differences were therefore noticeably reduced in the CTL and ALL databases, but not in the ASD.

### 7.2.2 Experiment 2: Within-site Between-Group Differences

In this second experiment, accuracy, sensitivity and specificity in the between-group comparison were recorded for images acquired from each site. This is an estimation of the discrimination ability of the different modalities without the influence of the site effects; Table 7.2. For all modalities, most of the values are close to a random classifier (~50%), indicative of having either no significant differences between groups, or having spatially heterogeneous patterns of sMRI measures across individuals where mass-univariate approaches are sub-optimal in detecting group differences. It is interesting to note that the London sample contained more between-group differences than those acquired in Cambridge.

### 7.2.3 Experiment 3: Effect of SWPCA on Group Differences

Finally, group differences were characterised with and without applying site-effects reduction via SWPCA to the five modalities.

Whole-brain VBM analysis was performed on the corrected and uncorrected maps from each modality. Figure 4 depicts the brain t-maps of significant ( $p < 0.01, |t| > 2.57$ ) [qT<sub>1</sub>](#), [qT<sub>2</sub>](#), [synT<sub>1</sub>](#), [GM](#) and [WM](#) between-group differences, using ALL, with the GM+WM mask, before and after applying SWPCA, so that the reduction of site-related variability can be observed. Some of the highlighted areas after applying SWPCA are inconsistent across modalities, with spurious peaks and noise, including a large area around the ventricles in the [qT<sub>1</sub>](#) and [synT<sub>1</sub>](#) modalities related to some abnormal participants that will be discussed later. However, there were some areas that were consistent across modalities. Significant areas found across at least 4 of the 5 modalities correspond to the Advanced Automated Labelling (AAL) (Tzourio-Mazoyer, et al., 2002) areas of: A) right superior frontal gyrus, Brodmann areas 6 ( $z=60$ ); B) the pars opercularis of the left inferior frontal gyrus, Brodmann areas 44; C) the pars triangularis of the left inferior frontal gyrus, Brodmann areas 45; D) the posterior part of the left middle temporal gyrus ( $z=24$ ); CSF filled spaces on the margins of the ventricles ( $z=-6,4,14,24$ ); and the left crus I of cerebellar hemisphere ( $z=-26$ ).

The complementary CBM (Section 2.4) analysis was performed on the most significant components. The resulting regions, statistically thresholded with

Modality	Mask	ALL		CTL		ASD	
		no-SWPCA	SWPCA	no-SWPCA	SWPCA	no-SWPCA	SWPCA
$qT_1$	GM+WM	0.875 $\pm$ 0.083	0.530 $\pm$ 0.130	0.847 $\pm$ 0.141	0.543 $\pm$ 0.115	0.769 $\pm$ 0.145	0.553 $\pm$ 0.093
	GM	0.849 $\pm$ 0.085	0.535 $\pm$ 0.107	0.835 $\pm$ 0.154	0.501 $\pm$ 0.090	0.712 $\pm$ 0.161	0.575 $\pm$ 0.084
	WM	0.865 $\pm$ 0.082	0.447 $\pm$ 0.071	0.876 $\pm$ 0.128	0.441 $\pm$ 0.058	0.813 $\pm$ 0.127	0.575 $\pm$ 0.153
$qT_2$	GM+WM	0.596 $\pm$ 0.128	0.503 $\pm$ 0.093	0.615 $\pm$ 0.196	0.454 $\pm$ 0.075	0.506 $\pm$ 0.192	0.476 $\pm$ 0.103
	GM	0.596 $\pm$ 0.126	0.493 $\pm$ 0.097	0.549 $\pm$ 0.187	0.478 $\pm$ 0.108	0.497 $\pm$ 0.197	0.425 $\pm$ 0.091
	WM	0.612 $\pm$ 0.131	0.560 $\pm$ 0.128	0.576 $\pm$ 0.195	0.550 $\pm$ 0.146	0.541 $\pm$ 0.185	0.575 $\pm$ 0.172
$synt_1$	GM+WM	0.904 $\pm$ 0.073	0.563 $\pm$ 0.060	0.919 $\pm$ 0.100	0.440 $\pm$ 0.057	0.807 $\pm$ 0.151	0.631 $\pm$ 0.098
	GM	0.879 $\pm$ 0.090	0.576 $\pm$ 0.035	0.899 $\pm$ 0.108	0.526 $\pm$ 0.079	0.800 $\pm$ 0.145	0.587 $\pm$ 0.042
	WM	0.904 $\pm$ 0.076	0.582 $\pm$ 0.047	0.894 $\pm$ 0.111	0.574 $\pm$ 0.038	0.859 $\pm$ 0.112	0.468 $\pm$ 0.101
$GM$	GM+WM	0.595 $\pm$ 0.133	0.586 $\pm$ 0.141	0.582 $\pm$ 0.192	0.566 $\pm$ 0.093	0.481 $\pm$ 0.169	0.468 $\pm$ 0.152
	GM	0.620 $\pm$ 0.141	0.585 $\pm$ 0.078	0.604 $\pm$ 0.227	0.574 $\pm$ 0.038	0.499 $\pm$ 0.188	0.525 $\pm$ 0.114
	WM	0.659 $\pm$ 0.139	0.448 $\pm$ 0.066	0.635 $\pm$ 0.180	0.507 $\pm$ 0.144	0.522 $\pm$ 0.206	0.525 $\pm$ 0.198
$WM$	WM	0.639 $\pm$ 0.124	0.549 $\pm$ 0.072	0.578 $\pm$ 0.194	0.516 $\pm$ 0.126	0.549 $\pm$ 0.160	0.526 $\pm$ 0.136

**Table 7.1:** Between-site classification accuracy ( $\pm$  standard deviation) for different modalities and masks without and with [SWPCA](#) correction.

Modality	Mask	LONDON			CAMBRIDGE		
		acc.	sens.	spec.	acc.	sens.	spec.
<b>qT<sub>1</sub></b>	GM+WM	0.603 ± 0.175	0.512 ± 0.260	0.692 ± 0.237	0.504 ± 0.193	0.492 ± 0.276	0.515 ± 0.307
	GM	0.501 ± 0.157	0.440 ± 0.244	0.565 ± 0.245	0.484 ± 0.201	0.488 ± 0.300	0.480 ± 0.327
	WM	0.505 ± 0.174	0.485 ± 0.248	0.526 ± 0.242	0.451 ± 0.197	0.465 ± 0.297	0.435 ± 0.296
<b>qT<sub>2</sub></b>	GM+WM	0.628 ± 0.168	0.535 ± 0.246	0.719 ± 0.237	0.467 ± 0.181	0.527 ± 0.307	0.417 ± 0.314
	GM	0.539 ± 0.149	0.425 ± 0.220	0.654 ± 0.222	0.491 ± 0.196	0.548 ± 0.316	0.430 ± 0.298
	WM	0.619 ± 0.194	0.585 ± 0.262	0.655 ± 0.250	0.472 ± 0.195	0.448 ± 0.283	0.492 ± 0.290
<b>synTr<sub>1</sub></b>	GM+WM	0.665 ± 0.158	0.578 ± 0.224	0.755 ± 0.238	0.479 ± 0.201	0.478 ± 0.318	0.475 ± 0.316
	GM	0.547 ± 0.159	0.475 ± 0.237	0.622 ± 0.252	0.514 ± 0.218	0.477 ± 0.322	0.555 ± 0.342
	WM	0.515 ± 0.185	0.520 ± 0.288	0.506 ± 0.254	0.509 ± 0.209	0.472 ± 0.317	0.542 ± 0.316
<b>GM</b>	GM+WM	0.513 ± 0.171	0.507 ± 0.252	0.518 ± 0.245	0.488 ± 0.202	0.445 ± 0.318	0.528 ± 0.285
	GM	0.586 ± 0.174	0.610 ± 0.247	0.564 ± 0.270	0.521 ± 0.187	0.522 ± 0.303	0.535 ± 0.289
	WM	0.471 ± 0.181	0.455 ± 0.245	0.488 ± 0.278	0.489 ± 0.206	0.502 ± 0.319	0.483 ± 0.314
<b>WM</b>	GM+WM	0.465 ± 0.174	0.445 ± 0.243	0.484 ± 0.268	0.468 ± 0.210	0.488 ± 0.292	0.448 ± 0.305

**Table 7.2:** Classification accuracy (Acc), sensitivity (Sen) and specificity (Spec) ± standard deviation for each modality and mask using the participants acquired at the LON and CAM sites.

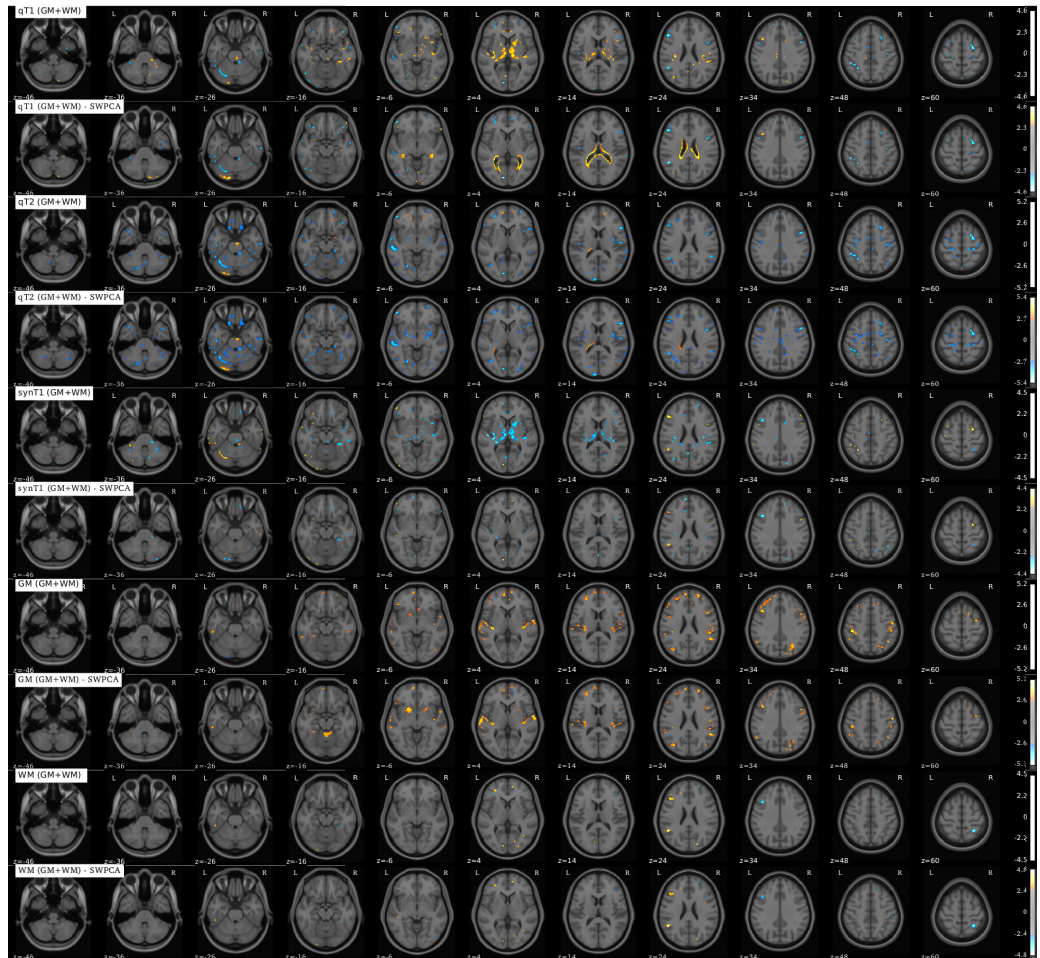


**Figure 7.5:** Brain t-map (VBM) of significant ( $p < 0.01, |t| > 2.57$ ) GM and WM differences in ASD using **qT<sub>1</sub>**, **qT<sub>2</sub>**, **synT<sub>1</sub>**, **GM** and **WM** maps before and after applying **SWPCA** to remove site effects.

$Z > 2.57$  (corresponding to  $p < 0.01$ ), were superimposed on the [MNI](#) template, and are depicted in Figure [7.6](#). A reduction of significant between-group areas after applying SWPCA is evident in most modalities, but particularly noticeable in the [qT<sub>1</sub>](#) and [qT<sub>2</sub>](#). In [WM](#) no significant regions were observed, neither before nor after SWPCA. The significant regions identified in any modality corresponded to the AAL areas of the CSF filled areas around the ventricles (planes  $z=-6, 4, 14, 24$ ), the right middle temporal gyrus (plane  $z=14$ ) and the left crus I of cerebellar hemisphere (plane  $z=-26$ ). However, none of these regions were repeated over more than two of the modalities, except for the large areas around ventricles that were caused by abnormalities in three participants, which will be discussed later.

Performance results for the classification analysis applied to ALL are shown in Table [7.3](#). Between-group results were quite similar before or after applying SWPCA, although reducing between-site variance generally reduced the performance towards a random classifier. The results in this table match the overall effects that were found in Figure 4, where most spurious significance peaks disappeared after applying [SWPCA](#), but some regions were highlighted. These regions, where SWPCA did not seem to eliminate the significant areas but enhanced them, could be responsible for the accuracy increment in the analysis of the [qT<sub>2</sub>](#) modality, and the [GM](#) with GM mask.

#### 7.2.4 Discussion

Brain anatomical and functional differences between ASD participants and controls have been explored by a number of previous studies (Di Martino, et al., 2014; Ecker, et al., 2015; Hernandez, et al., 2015; Lenroot and Yeung, 2013; Zürcher, et al., 2015). Many affected structures have been proposed in each of these studies, however as a recent large-scale study points out (Haar, et al., 2014), these are frequently inconsistent throughout the literature. Researchers argue that most of these structures are database-dependent, and since many studies use multi-site acquisition procedures, the variance introduced by each acquisition site is a probable source of Type I errors.

The technical and logistical drawbacks of multicentre studies are widely documented, including participant recruitment procedures (Pearlson, 2009) and technical effects that range from the usage of different equipment or acquisition parameters (Van Horn and Toga, 2009) to physical changes that affect the performance of [MRI](#) scanners across time (Pearlson, 2009). There is general recognition that standardization is needed to ensure the uniformity of the acquired maps. Different approaches have been used in large-scale studies, such as [ADNI](#) where



**Figure 7.6:** Brain Z-map (CBM) of significant ( $p < 0.01, |t| > 2.57$ ) GM and WM differences using  $qT_1$ ,  $qT_2$ ,  $synT_1$ , GM and WM maps before and after applying SWPCA to remove site effects.

Modality	Mask	NO-SWPCA			SWPCA		
		acc.	sens.	spec.	acc.	sens.	spec.
$\text{qT}_1$	GM+WM	0.564 ± 0.123	0.503 ± 0.179	0.625 ± 0.177	0.435 ± 0.123	0.499 ± 0.181	0.371 ± 0.178
	GM	0.523 ± 0.112	0.468 ± 0.162	0.580 ± 0.192	0.458 ± 0.120	0.477 ± 0.187	0.441 ± 0.210
	WM	0.504 ± 0.131	0.475 ± 0.191	0.533 ± 0.194	0.484 ± 0.123	0.511 ± 0.179	0.456 ± 0.194
$\text{qT}_2$	GM+WM	0.578 ± 0.115	0.487 ± 0.208	0.669 ± 0.178	0.593 ± 0.136	0.546 ± 0.206	0.640 ± 0.194
	GM	0.554 ± 0.135	0.492 ± 0.194	0.614 ± 0.181	0.526 ± 0.144	0.512 ± 0.209	0.543 ± 0.222
	WM	0.516 ± 0.138	0.508 ± 0.198	0.522 ± 0.216	0.499 ± 0.137	0.477 ± 0.209	0.521 ± 0.196
$\text{synT}_1$	GM+WM	0.596 ± 0.132	0.509 ± 0.194	0.680 ± 0.172	0.577 ± 0.130	0.479 ± 0.208	0.676 ± 0.183
	GM	0.587 ± 0.139	0.509 ± 0.210	0.665 ± 0.169	0.483 ± 0.136	0.489 ± 0.218	0.480 ± 0.200
	WM	0.496 ± 0.139	0.500 ± 0.189	0.492 ± 0.194	0.487 ± 0.134	0.513 ± 0.189	0.461 ± 0.211
GM	GM+WM	0.498 ± 0.120	0.486 ± 0.197	0.507 ± 0.203	0.490 ± 0.123	0.514 ± 0.197	0.465 ± 0.182
	GM	0.574 ± 0.121	0.571 ± 0.189	0.579 ± 0.163	0.593 ± 0.127	0.602 ± 0.172	0.587 ± 0.190
WM	GM+WM	0.499 ± 0.132	0.506 ± 0.189	0.487 ± 0.181	0.521 ± 0.129	0.510 ± 0.209	0.532 ± 0.180
	WM	0.506 ± 0.143	0.488 ± 0.219	0.526 ± 0.197	0.507 ± 0.122	0.521 ± 0.165	0.492 ± 0.193

**Table 7.3:** Classification accuracy (Acc), sensitivity (Sen), and specificity (Spec) ± STD for the different modalities and masks using ALL, before and after applying SWPCA.

human “phantoms” were used to perform a preparatory optimisation of MRI scanning platforms (Friedman and Glover, 2006).

There are two major types of site effects, regardless of their source: geometric distortions and intensity inhomogeneities. In this work, we focused on the latter, since much of the geometric distortion has been eliminated during acquisition (see Section 2.1), and the DARTEL normalization and registration acts as a homogenizing step, reducing both between-site and between-subject geometric differences, substantially reducing the impact of the site-related geometric differences.

Regarding intensity correction, in the MRC AIMS database used in this study (Ecker, et al., 2013; Ecker, et al., 2012), a standardization procedure based on quantitative imaging (Deoni, et al., 2008) was used to minimize inter-site variance and improve the signal-to-noise contrast. However, as the between-site analysis in Section 7.2.1 suggests, this strategy still results in variance that makes it easier to distinguish scanning sites than diagnostic groups. For example, when using  $qT_1$  the accuracy for LON vs. CAM classification was >80%, whilst when classifying ASD vs. CTL it was 52%. This marks the substantial effect of site variance on the maps’ intensity distribution, even when the multi-site study employs quantitative imaging protocol on the same model of scanner platform across sites. However, with the inclusion of GM and WM maps, we can observe that the inhomogeneities found on  $qT_1$  or  $synT_1$  barely affected the segmentation procedure.

In this work, the approach we have taken is to perform a multivariate decomposition of each dataset into a number of components that explain different portions of variance. The following step was to identify the components of variance that are due to multi-site acquisition and reduce them. Decomposition was completed using PCA and then, to identify which of the components were linked to acquisition site, we performed an ANOVA on the component scores. Finally, using the weighting function defined in Sec. 7.2.3, we reconstructed the original signal reducing the undesired variance, in what we called Significance Weighted PCA (SWPCA). The method has proven its ability in reducing undesired variance, quantifiable by means of the accuracy obtained in a site vs. site classification. In this case, SWPCA reduced the accuracy from >0.8 to approximately ~0.5, a random classifier, suggesting that most site-related variance was eliminated.

A simpler approach such as applying a voxel-by-voxel ANOVA would also be useful to reduce the acquisition site effects (Suckling, et al., 2012). However, SWPCA is a multivariate approach that still offers major advantages over this voxel-wise algorithm, and similar algorithms have found utility in text document searches (Kriegel, et al., 2008; Tavoli, et al., 2013; Zhang and Nguyen, 2005).

First, PCA models the different sources of variance of the dataset, whereas a simple voxel-wise ANOVA only removes mean site differences, which might result in less statistical power. Secondly, SWPCA is multivariate in nature, where each component contains information that potentially affects all voxels. Together, these two features allow SWPCA to identify the components linked to the undesired effects, and reduce their impact with a weighted reconstruction approach, reducing the general variance related to the acquisition site. However, this increased power reveals a major drawback: SWPCA needs at least a moderate number of participants to work properly. That is the reason why we cannot apply SWPCA to databases such as ADNI (Friedman and Glover, 2006) or ABIDE (Di Martino, et al., 2014), where the number of participants acquired at each site is small, or to the six travelling phantoms used in the calibration of the MRC AIMS study.

There exist a number of similar multivariate methods that model the influence of categorical variables, such as the well-known Partial Least Squares (PLS) algorithm (Vinzi, et al., 2010) or Surrogate Variable Analysis (SVA) (Leek and Storey, 2007). In the first case, both PLS and SWPCA take categorical variables  $\mathbf{Y}$  along with the data  $\mathbf{X}$  as inputs to partition the influence of these into components. However, the most significant difference is the underlying model. Whilst SWPCA estimates the principal components blindly using their variance, which is what we aim to reduce, and performs an ANOVA afterwards, PLS uses the categorical variable in the computation of the covariance matrix and then estimates the components.

On the other hand, SVA, used for gene expression studies (Leek and Storey, 2007), is more comparable to SWPCA. The SVA algorithm uses a number of decomposition and significance estimation steps to construct a set of surrogate variables; that is, variables that account for the unmodeled variance and expression heterogeneity. While similar to SWPCA in the steps used (i.e. SVD decomposition and significance estimation), their approaches are fundamentally different. SVA constructs a higher complexity model that starts by eliminating the contribution of primary variables to produce a number of unknown hidden (surrogate) variables, whereas SWPCA is intended to reduce complexity by producing variance-reduced maps to reduce the influence of previously known, but unconsidered, variables and facilitate a subsequent analysis focused only on the relevant variables.

Focusing on the VBM results, after performing the site-effects removal by SWPCA significant between-group differences were noted in five areas: A) the right superior frontal gyrus; B) the pars opercularis of the left inferior frontal gyrus; C) the pars triangularis of the left inferior frontal gyrus; D) the posterior part of the left middle temporal gyrus; and E) the left crus I of cerebellar hemisphere.

The first three regions are within Brodmann areas 6, 44 and 45. However, when examining the projection of the region D onto the MNI template (see Figure 6), it is also located in the posterior part of the left superior temporal gyrus. Therefore, D corresponds closely with the region between Brodmann areas 22 and 39, the Temporo-Parietal Junction (TPJ), with negative t-value at the left side (containing Wernicke's area) and positive t-value at the right side.

The role of these regions in autism has received much attention. Brodmann areas 44 and 45, that together make the Broca's Area (of importance in speech production and a proposed part of the human mirror neuron system (Nishitani, et al., 2005)), is a region where mirror neuron dysfunction has been consistently reported in ASD-affected children (Dapretto, et al., 2006) and adults (Hadjikhani, et al., 2006; Lopez-Hurtado and Prieto, 2008; Verly, et al., 2014). Wernicke's area, contained in the left TPJ, is also linked to language, and has been associated with ASD in several works (Hadjikhani, et al., 2006; Kriegel, et al., 2008; Verly, et al., 2014). Additionally, the right TPJ has been proposed as related to mentalizing and has been repeatedly implicated in autism (Barnea-Goraly, et al., 2004), including a fMRI study of a subsample of this same AIMS dataset (Lombardo, et al., 2011). The right superior frontal gyrus (region A) is more equivocal, with some studies (Ecker, et al., 2010; Ecker, et al., 2012) reporting abnormalities in this area, while others (Hadjikhani, et al., 2006; Segovia, et al., 2014) report no significant differences. Our analyses reveal no differences in the insula and amygdala, brain structures frequently linked to autism.

Some regions, particularly in qT<sub>2</sub>, synT<sub>1</sub> and segmented GM maps show potentially spurious significance peaks around the ventricles and especially in the left crus I of cerebellar hemisphere (region E). After examining the database, two individuals had appreciable structural abnormalities in the form of abnormal ventricle size and cerebellar atrophy, as can be seen in Figure 7. It is possible that these participants influenced the computation of the t-maps, and therefore are responsible for the significance in region E and areas surrounding the ventricles and, since they are part of the LON subdataset, could also be responsible for the increased classification accuracy of the quantitative T<sub>1</sub> and T<sub>2</sub>, and the synthetic T<sub>1</sub> maps in this sub-dataset.

After observing the influence of these participants on the computation of the t-maps, we can assume that most of the structural differences in ASD are so subtle that the influence of just one or two images can impact on the final results. This, along with the poor performance of the classification pipeline presented in Section 3, dramatically reduces the significance of the aforementioned t-maps. Therefore, the existing evidence leads to the conclusion that ASD presents as either undetectable structural differences or, more likely, with such heterogeneous

differences that are difficult to establish a common pattern even after reducing the variance introduced by acquisition site.

It may be the case that cohorts of individuals examined at different sites are somehow systematically biased towards a specific type of patient (in ways that we cannot see simply based on phenotypic information), then site-related intensity variability is also enriched with important variability about nested autism subgroups. So with any technique trying to remove the site-related inhomogeneity, the subgroup information could also be removed. Together, the evidence supports the claim that defining meaningful subgroups based on different measures, such as genetic profiling, clinical co-morbidities or sensory sensitivities, is the most urgent next step for ASD research (Haar, et al., 2014).

## 7.3 Results for DaTSCAN Datasets

SWPCA	Norm.	Performance		
		acc.	sens.	spec.
no	max	$0.883 \pm 0.030$	$0.855 \pm 0.058$	$0.915 \pm 0.058$
	int	$0.877 \pm 0.035$	$0.849 \pm 0.073$	$0.908 \pm 0.079$
	stable	$0.898 \pm 0.033$	$0.883 \pm 0.057$	$0.915 \pm 0.079$
yes	max	$0.539 \pm 0.100$	$0.527 \pm 0.373$	$0.550 \pm 0.337$
	int	$\pm$	$\pm$	$\pm$
	stable	$0.361 \pm 0.102$	$0.394 \pm 0.295$	$0.322 \pm 0.270$

**Table 7.4:** Performance measures for the combined DaTSCAN dataset found before and after applying SWPCA.



# 8

## SIMULATION OF FUNCTIONAL BRAIN IMAGES

### 8.1 Simulation Procedure



Figure 8.1: Schema of the brain image synthesis algorithm.

#### 8.1.1 Decomposition via PCA

The first step in our simulation algorithm is to project the original dataset to a new space defined by the principal components of the set; that is, the eigenbrain space. In this space, each subject from the original dataset is projected to a point, and we can afterwards use the space basis (the principal components) to reconstruct that particular subject. In this work we will use the first  $N$  components for performance, where  $N$  is the number of subjects that are used in the computation of [PCA](#). For more details about [PCA](#), see Section [7.1.1](#).

#### 8.1.2 Probability Density Modelling using Kernel Density Estimation

Kernel Density Estimation ([KDE](#)) is used here to model the statistical distribution of the projected subjects in the eigenbrain space, and it is applied independently to each [AD](#), [MCI](#) and [CTL](#) class. The [KDE](#) estimates the probability density

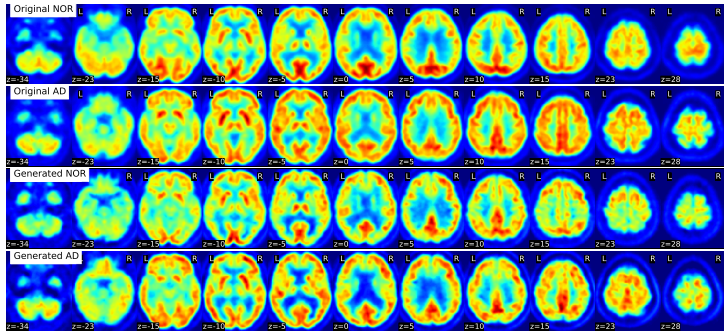


**Figure 8.2:** Comparison between simulated and original images from [AD](#) and [CTL](#) classes.

function  $f$  from a number of independent and identically distributed samples  $(x_1, x_2, \dots, x_n)$ , in the following manner:

$$\hat{f}_h(x) = \frac{1}{n} \sum_{i=1}^n K_h(x - x_i) = \frac{1}{nh} \sum_{i=1}^n K\left(\frac{x - x_i}{h}\right), \quad (8.1)$$

where  $h > 0$  is the bandwidth, a smoothing parameter. The [KDE](#) via diffusion [[Botev2010](#)] used in this article uses a data-driven automatic estimation of the bandwidth, which unlike most methods, does not rely on arbitrary normal reference rules.

### 8.1.3 Probability Density Modelling using Multivariate Gaussian

### 8.1.4 Random Number Generation

### 8.1.5 Brain Image Synthesis

## 8.2 Experimental Setup

To validate the simulated dataset, we have performed two different experiments:

- **Exp. 1:** We have estimated the predictive power of the simulated images by generating new images from the original training set in each cross-validation iteration and using them to predict the original test set.
- **Exp. 2:** We tested that the simulated images are independent from the original ones, although preserving similar characteristics. To do so, following a Voxel as Features (VAF) approach [[70](#)], we extract a small subset

(10 AD and 10 NOR) from the original dataset. Then, we trick the classifier, training it with the whole subset -instead of the training set only-, and testing it against the test set. Therefore, the performance of the tricked system must be close to 1. Then, we generate a new set of simulated images (100 AD and 100 NOR) from the reduced subset and proceed similarly. If our simulated images are independent from the originals, the performance of the system should decrease substantially.

Classification is performed using a Support Vector Machine (SVM) classifier with linear kernel. Estimation of parameter C is performed in an inner cross-validation loop within the training set. Values of accuracy (acc), sensitivity (sens) and specificity (spec) and their standard deviation (SD) are estimated.

## 8.3 Results for ADNI-PET Dataset

### 8.3.1 Experiment 1

The performance results for the proposed experiments are shown in Table 8.1. Exp. 1 is applied to three different scenarios: only AD vs NOR (95 vs 101 subjects), and after incorporating MCI subjects, using them as NOR or AD.

Scenario	acc ( $\pm$ SD)	sens ( $\pm$ SD)	spec ( $\pm$ SD)
AD vs NOR	$0.882 \pm 0.012$	$0.865 \pm 0.091$	$0.901 \pm 0.118$
MCI as NOR	$0.727 \pm 0.119$	$0.769 \pm 0.155$	$0.789 \pm 0.151$
MCI as AD	$0.739 \pm 0.126$	$0.747 \pm 0.147$	$0.845 \pm 0.146$

**Table 8.1:** Baseline performance of the set, using the original dataset.

Scenario	acc ( $\pm$ SD)	sens ( $\pm$ SD)	spec ( $\pm$ SD)
AD vs NOR	$0.801 \pm 0.095$	$0.782 \pm 0.202$	$0.821 \pm 0.191$
MCI as NOR	$0.751 \pm 0.078$	$0.433 \pm 0.201$	$0.851 \pm 0.262$
MCI as AD	$0.712 \pm 0.048$	$0.821 \pm 0.062$	$0.382 \pm 0.248$

**Table 8.2:** Performance of Exp 1, demonstrating the predictive ability of the simulated images over the real dataset.

Scenario	acc ( $\pm$ SD)	sens ( $\pm$ SD)	spec ( $\pm$ SD)
Original	$1.000 \pm 0.000$	$1.000 \pm 0.000$	$1.000 \pm 0.000$
Simulated	$0.839 \pm 0.094$	$0.830 \pm 0.228$	$0.849 \pm 0.206$

**Table 8.3:** Performance of the Exp 3 proves the independence of the simulated images with respect to the originals.

## 8.4 Results for DaTSCAN Datasets

## **Part IV**

### **GENERAL DISCUSSION AND CONCLUSIONS**



# 9

## GENERAL DISCUSSION AND CONCLUSIONS

### 9.1 General Discussion

#### 9.1.1 Discussion on the algorithms

#### 9.1.2 Discussion on the diseases

### 9.2 Conclusions

### 9.3 Future Work

asdf



Part V  
**APPENDIX**



# A | DATASETS

Many dataset are used in this thesis, covering three imaging modalities and three disorders. A summary of these can be found on Table A.1, folowed by a longer description of each one.

Acronym	Origin	Disease	Modality	Drug
ADNI-MRI	ADNI	AD	MRI	-
AIMS-MRI	MRC-AIMS	ASD	MRI	-
ADNI-PET	ADNI	AD	PET	HMPAO!
VDLN-HMPAO	VDLN	AD	SPECT	HMPAO!
VDLN-DAT	VDLN	PKS	SPECT	DaTSCAN
VDLV-DAT	VDLV	PKS	SPECT	DaTSCAN
PPMI-DAT	PPMI	PKS	SPECT	DaTSCAN

**Table A.1:** Summary of the datasets used in this thesis.

## A.1 Magnetic Resonance Imaging

### A.1.1 ADNI-MRI, Alzheimer's Disease Neuroimaging Initiative

AD

### A.1.2 AIMS-MRI, MRC-AIMS Consortium

Structural MRI were analysed from 136 adult, right-handed males (68 with ASD and 68 matched controls) with no significant mean differences in age and full-scale IQ, acquired from the centres contributing to the UK Medical Research Council Autism Imaging Multi-centre Study (MRC AIMS) (Ecker, et al., 2013; Ecker, et al., 2012) and recruited by advertisement. In this work, only participants recruited at the Institute of Psychiatry, King's College London (LON) and

the Autism Research Centre, University of Cambridge (CAM) were included where an equivalent set of images were acquired from each participant.

Participants were excluded from the study if they had a history of major psychiatric disorder or medical illness affecting brain function (e.g. psychosis or epilepsy), or current drug misuse (including alcohol), or were taking antipsychotic medication, mood stabilizers or benzodiazepines.

All participants with ASD were diagnosed according to International Classification of Diseases, 10th Revision (ICD-10) research criteria, and confirmed using the Autism Diagnostic Interview-Revised (ADI-R) (Lord, et al., 1994). Autism Diagnostic Observation Schedule (ADOS) (Lord, et al., 2000) was performed, but the score was not considered as an inclusion criteria. ASD participants, to be included, must have scored above the ADI-R cut-off in the three domains of impaired reciprocal social interaction, communication and repetitive behaviours and stereotyped patterns, although failure to reach cut-off in one of the domains by one point was permitted. Intellectual ability was assessed using the Wechsler Abbreviated Scale of Intelligence (WASI) (Wechsler, 1999), ensuring the participants fell within the high-functioning range on the spectrum defined by a full-scale IQ > 70. The demographics of the participants are shown in detail in Table A.2.

Database	Group	N	Age ( $\mu \pm \sigma$ years)	IQ ( $\mu \pm \sigma$ )
LON	ASD	39	$28.74 \pm 6.52$	$111.28 \pm 13.13$
	CTL	40	$25.30 \pm 6.62$	$104.67 \pm 11.16$
CAM	ASD	29	$26.83 \pm 4.64$	$115.83 \pm 11.88$
	CTL	28	$26.75 \pm 7.32$	$115.25 \pm 13.67$
ALL	ASD	68	$25.90 \pm 6.95$	$109.03 \pm 13.31$
	CTL	68	$27.93 \pm 5.87$	$113.22 \pm 12.81$

Table A.2: Demographics of the AIMS-MRI dataset.

Structural MRI were obtained using Driven Equilibrium Single Pulse Observation of T<sub>1</sub> and T<sub>2</sub> (DESPOT<sub>1</sub>, DESPOT<sub>2</sub>) (Deoni, et al., 2008) at King's College London and University of Cambridge, both with 3T GE Medical Systems HDx scanners. Using multiple Spoilt Gradient Recall (SPGR) acquisitions in the DESPOT<sub>1</sub> sequence and Steady State Free Procession (SSPF) acquisitions in the DESPOT<sub>2</sub> sequence, with different flip angles and repetition times, qT<sub>1</sub> and qT<sub>2</sub> maps were calculated with a custom ImageJ plug-in package. Correction of main and transmit magnetic field (B<sub>0</sub> and B<sub>1</sub>) inhomogeneity effects was performed during the estimation of T<sub>1</sub> and T<sub>2</sub>.

For accurate registration to the standard stereotatic space of the [MNI](#), a [synT<sub>1</sub>](#) images were created based on the [qT<sub>1</sub>](#) maps (Ecker, et al., 2013; Ecker, et al., 2012; Lai, et al., 2012). The [synT<sub>1</sub>](#) images were then segmented using New Segment into [GM](#) and [WM](#) maps, and normalized to the [MNI](#) space using DARTEL in SPM8 (Friston, et al., 2007), with modulation (preserve volume) to retain information of regional/local [GM](#) and [WM](#) volumes, and smoothed with a 3mm FWHM Gaussian Kernel to account for inter-subject mis-registration. The [synT<sub>1</sub>](#), [qT<sub>1</sub>](#) and [qT<sub>2</sub>](#) maps were also registered to the standard [MNI](#) space using the same DARTEL flow fields, but without modulation (preserve concentration) to retain information of regional/local T<sub>1</sub> contrast, T<sub>1</sub> relaxation time, and T<sub>2</sub> relaxation times, and smoothed with a 3mm FWHM Gaussian kernel. Therefore, there were five different modalities: [qT<sub>1</sub>](#), [qT<sub>2</sub>](#), [synT<sub>1</sub>](#) map, [GM](#) and [WM](#) maps, for each every participant, which allows us to observe the impact of our [SWPCA](#) correction of site-related undesired variance on quantitative ([qT<sub>1</sub>](#) and [qT<sub>2</sub>](#)), simulated ([synT<sub>1</sub>](#)) images and probability maps ([GM](#) and [WM](#)).

During the pre-processing of the images, several procedures targeted the reduction of inter-subject and inter-site geometric distortion, amongst them the correction of B<sub>0</sub> and B<sub>1</sub> field inhomogeneity effects and the registration to [MNI](#) space. Many other algorithms have been proposed to help in this task. However, the study of their relative performance lies beyond the scope of this article. Following image registration, it was assumed that only the intensity of the maps was affected between sites.

## A.2 Positron Emission Tomography

### A.2.1 ADNI-PET, Alzheimer's Disease Neuroimaging Initiative

Data used in the preparation of this article were obtained from the Alzheimer's Disease Neuroimaging Initiative (ADNI) database ([adni.loni.usc.edu](http://adni.loni.usc.edu)). The ADNI was launched in 2003 as a public-private partnership, led by Principal Investigator Michael W. Weiner, MD. The primary goal of ADNI has been to test whether serial MRI, PET, other biological markers, and clinical and neuropsychological assessment can be combined to measure the progression of MCI and AD. For up-to-date information, see [www.adni-info.org](http://www.adni-info.org).

Data used in the preparation of this article were obtained from the Alzheimer's Disease Neuroimaging Initiative (ADNI) database ([adni.loni.usc.edu](http://adni.loni.usc.edu)). In this work, the <sup>18</sup>F-FDG PET images, used to estimate the metabolic activity of the brain, are used to generate and validate the simulated images. 95 PET images from AD affected subjects, 207 images from Mild Cognitive Impairment (MCI)

affected subjects and 101 images from Normal Controls (NOR) have been used to construct the original  $N = 403$  set from which the simulation parameters will be obtained.

## A.3 Single Photon Emission Computed Tomography

### A.3.1 VDLN-HMPAO, Virgen de las Nieves

The database is built up of imaging studies of subjects following the protocol of an hospital-based service. First, the neurologist evaluated the cognitive function, and those patients with findings of memory loss or dementia were referred to the nuclear medicine department in the “Virgen de las Nieves” hospital (Granada, Spain), in order to acquire complementary screening information for diagnosis<sup>1</sup>. Experienced physicians evaluated the images visually. The images were assessed using 4 different labels: **CTL** for subjects without scintigraphic abnormalities and mild perfusion deficit (AD1), moderate deficit (AD2) and severe deficit (AD3), to distinguish between different levels of presence of hypoperfusion patterns compatible with AD. In total, the database consists of  $n = 97$  subjects: 41 **CTRL**, 30 **AD1**, 22 **AD2** and 4 **AD3** (see table A.3 for demographic details). Since the patients are not pathologically confirmed, the subject’s labels possesses some degree of uncertainty, as the pattern of hypo-perfusion may not reflect the underlying pathology of AD, nor the different classification of scans necessarily reflect the severity of the patients symptoms. However, when pathological information is available, visual assessments by experts have been shown to be very sensitive and specific labelling methods, in contrast to neuropsychological tests [**jobst\_accurate\_1998**, **dougall\_systematic\_2004**]. Given that this is an inherent limitation of ‘in vivo’ studies, our working-assumption is that the labels are true, considering the subject label positive when belonging to any of the AD classes, and negative otherwise.

### A.3.2 VDLN-DAT, Virgen de las Nieves

SPECT DATSCAN

73 **CTL**, 45 **PD**, 30 **SWEDD**.

---

<sup>1</sup> Clinical information is unfortunately not available for privacy reasons, but only demographic information

	#samples	Sex(M/F)(%)	$\mu$ [range/ $\sigma$ ]
CTRL	41	32.95/12.19	71.51[46-85/7.99]
AD1	29	10.97/18.29	65.29[23-81/13.36]
AD2	22	13.41/9.76	65.73[46-86/8.25]
AD3	4	0/2.43	76[69-83/9.90]

**Table A.3:** Demographic details of the ADNI-PET dataset. CTRL = Normal Controls, AD 1 = possible AD, AD 2 = probable AD, AD 3 = certain AD.  $\mu$  and  $\sigma$  stands for population mean and standard deviation respectively.

### A.3.3 VDLV-DAT, Virgen de la Victoria Hospital

The images were obtained after a period of between 3 and 4 hours after the intravenous injection of 185 MBq (5 mCi) of DaTSCAN, with prior thyroid blocking with Lugol's solution. The tomographic study (SPECT) with Ioflupane/FP-CIT-I-123 was performed using a General Electric gamma camera, Millennium model, equipped with a dual head and general purpose collimator. A 360-degree circular orbit was made around the cranium, at 3-degree intervals, 60 images with a duration of 35 seconds per interval,  $128 \times 128$  matrix. Image reconstruction was carried out using filtered back-projection algorithms without attenuation correction [Shepp82, Vardi1985], application of a Hanning filter (frequency 0.7) and images were obtained with transaxial cuts, following the method proposed in [Ramirez2009].

The images were interpreted by three Nuclear Medicine specialists, with masking of the clinical orientation. Visual assessment was established by exclusively considering the normal/abnormal criterion and after arriving at a consensus report between the three specialists, i.e. whether the FP-CIT SPECT allowed differentiation of a group of conditions with presynaptic involvement from others in which their integrity is assumed, without trying to assign them to different clinical groups within the set of pathological studies. A study was considered to be normal when bilateral, symmetrical uptake appeared in caudate and putamen nuclei, and abnormal when there were areas of qualitatively reduced uptake in any of the striatal structures.

A total of 208 subjects (100 patients and 108 controls), randomly selected from the total studies performed in this center until December 2008 and referred to it because of a movement disorder, were included in the study. Mean age was 70.2 years (41-87) with a standard deviation of 10.2 years (a detailed description of the database can be found in [60]). Clinical diagnosis, a parameter used as 'gold Standard' to establish the existence of PS, was made using the diagnostic

criteria established previously, with an established minimum follow-up period of 18 months. Those patients who were receiving treatment with drugs that had known or suspected effect on the level of the dopaminergic transporters through direct competitive mechanism were excluded. Although PD is the most representative pathology of PS, there are other medical conditions which, though they differ clinically from this, are also expressed by this set of symptoms. Some of them are multisystem atrophy (MSA), progressive supra-nuclear palsy (PSP) and corticobasal degeneration (CBD), in which, unlike PD, as well as involvement of the presynaptic terminal, there is involvement at the post-synaptic level of the nigrostriatal pathway.

#### A.3.4 PPMI-DAT, Parkinson's Progression Markers Initiative

Data used in the preparation of this article were obtained from the Parkinson's Progression Markers Initiative (PPMI) database ([www.ppmi-info.org/data](http://www.ppmi-info.org/data)). For up-to-date information on the study, visit [www.ppmi-info.org](http://www.ppmi-info.org).

The images in this database were imaged 4 + 0.5 hours after the injection of between 111 and 185 MBq of DaTSCAN. Subjects were also pretreated with saturated iodine solution (10 drops in water) or perchlorate (1000 mg) prior to the injection. All subjects had a supplied  $^{57}\text{Co}$  line marker affixed along the canthomeatal line, which will facilitate subsequent image processing and allow the core lab to accurately distinguish left and right in the face of multiple image file transfers. These markers are only evident in the  $^{57}\text{Co}$  window and hence do not contaminate the  $^{123}\text{I}$ -DaTSCAN brain data [PPMI, Initiative2010].

111 CTL, 32 SWEDD and 158 PD

Raw projection data are acquired into a  $128 \times 128$  matrix stepping each 3 degrees for a total of 120 projection into two 20% symmetric photopeak windows centered on 159 KeV and 122 KeV with a total scan duration of approximately 30 - 45 minutes. Other scan parameters (collimation, acquisition mode, etc.) are selected for each site. The images of both the subject's data and the cobalt striatal phantom are reconstructed and attenuation corrected, implementing either filtered back-projection or an iterative reconstruction algorithm using standardized approaches [Initiative2010]. After the processing, the database contains 289 spatially normalized images, 114 from Normal Control subjects and 175 from PD patients, and of a  $91 \times 109 \times 91$  size.

# B

## BACKGROUND ON SUPPORT VECTOR MACHINES

Support Vector Machine ([SVM](#)), introduced in the late 70s [[Vapnik1982](#)], are a set of related supervised learning methods widely used in pattern recognition, voice activity detection (VAD), classification and regression analysis.

We suppose the data to be linearly separable. In this case, a data point is viewed as a p-dimensional vector. Our objective is to separate a set of binary labelled training data with a hyperplane that is maximally distant from the two classes (known as the maximal margin hyper-plane). To do so, we build a function  $f : \Re^n \rightarrow \{\pm 1\}$  using training data that is, p-dimensional patterns  $x_i$  and class labels  $y_i$ :

$$(x_1, y_1), (x_2, y_2), \dots, (x_l, y_l) \in \Re^n \times \{\pm 1\} \quad (\text{B.1})$$

so that  $f$  will correctly classify new examples  $(x, y)$ .

Linear discriminant functions define decision hypersurfaces or hyperplanes in a multidimensional feature space, that is:

$$g(x) = \mathbf{w}^T x + \omega_0 = 0, \quad (\text{B.2})$$

where  $\mathbf{w}$  is known as the weight vector and  $\omega_0$  as the threshold. The weight vector  $\mathbf{w}$  is orthogonal to the decision hyperplane and the optimization task consists of finding the unknown parameters  $\omega_i, i = 1, \dots, n$  defining the decision hyperplane.

Let  $x_i, i = 1, 2, \dots, n$  be the feature vectors of the training set,  $X$ . These belong to either of the two classes,  $\omega_1$  or  $\omega_2$ . If the classes were linearly separable, the objective would be to design a hyperplane that classifies correctly all the training vectors. The hyperplane is not unique, and the selection process is focused on maximizing the generalization performance of the classifier, that is, the ability of the classifier, designed using the training set, to operate satisfactorily with new data. Among the different design criteria, the maximal margin hyperplane is usually selected since it leaves the maximum margin of separation between the two classes. Since the distance from a point  $x$  to the hyperplane is given by  $z = |g(x)|/\|\mathbf{w}\|$ , scaling  $w$  and  $w_0$  so that the value of  $g(x)$  is  $+1$  for the nearest point in  $\omega_1$  and  $-1$  for the nearest points in  $\omega_2$ , reduces the optimization problem to maximizing the margin:  $2/\|\mathbf{w}\|$  with the constraints:

$$\mathbf{w}^T \mathbf{x} + \mathbf{w}_0 \geq 1, \forall \mathbf{x} \in \omega_1 \quad (\text{B.3})$$

$$\mathbf{w}^T \mathbf{x} + \mathbf{w}_0 \leq 1, \forall \mathbf{x} \in \omega_2 \quad (\text{B.4})$$

## BIBLIOGRAPHY

- [1] F.J. Martínez-Murcia et al. "On the Brain Structure Heterogeneity of Autism: Parsing out Acquisition Site Effects With Significance-Weighted Principal Component Analysis". In: *Human Brain Mapping* 38.3 (Mar. 2017), pp. 1208–1223.  
DOI: [10.1002/hbm.23449](https://doi.org/10.1002/hbm.23449).
- [2] Alzheimer's Association et al. "2016 Alzheimer's disease facts and figures". In: *Alzheimer's & Dementia* 12.4 (2016), pp. 459–509.
- [3] Neil R Carlson. *Physiology of behavior*. Pearson, 2016.
- [4] F.J. Martinez-Murcia, J. Górriz, and J. Ramírez. "Computer Aided Diagnosis in Neuroimaging". In: *Computer-aided Technologies - Applications in Engineering and Medicine*. Ed. by Razvan Udroiu. 1st ed. Intech, Dec. 2016. Chap. 7, pp. 137–160. ISBN: 978-953-51-4895-1.  
DOI: [10.5772/64980](https://doi.org/10.5772/64980).
- [5] F.J. Martinez-Murcia, J.M. Górriz, and J. Ramírez. "Feature Extraction". In: *Wiley Encyclopedia of Electrical and Electronics Engineering*. Wiley, 2016, Accepted.  
DOI: [10.1002/047134608X](https://doi.org/10.1002/047134608X).
- [6] F.J. Martinez-Murcia, J.M. Górriz, J. Ramírez, and A. Ortiz. "A Spherical Brain Mapping of MR Images for the Detection of Alzheimer's Disease". In: *Current Alzheimer Research* 13.5 (Mar. 2016), pp. 575–588.  
DOI: [10.2174/1567205013666160314145158](https://doi.org/10.2174/1567205013666160314145158).
- [7] F.J. Martinez-Murcia, J.M. Górriz, J. Ramírez, and A. Ortiz. "A Structural Parametrization of the Brain Using Hidden Markov Models-Based Paths in Alzheimer's Disease". In: *International Journal of Neural Systems* 26.7 (Nov. 2016), p. 1650024.  
DOI: [10.1142/S0129065716500246](https://doi.org/10.1142/S0129065716500246).
- [8] F Segovia, JM Gorriz, J Ramírez, and D Salas-Gonzalez. "Multiclass classification of 18 F-DMFP-PET data to assist the diagnosis of parkinsonism". In: *Pattern Recognition in Neuroimaging (PRNI), 2016 International Workshop on*. IEEE. 2016, pp. 1–4.

- [9] Jeff Sevigny, Ping Chiao, Thierry Bussière, Paul H Weinreb, Leslie Williams, Marcel Maier, Robert Dunstan, Stephen Salloway, Tianle Chen, Yan Ling, et al. "The antibody aducanumab reduces A $\beta$  plaques in Alzheimer's disease". In: *Nature* 537.7618 (2016), pp. 50–56.
- [10] L. Khedher, J. Ramírez, J.M. Górriz, A. Brahim, and F. Segovia. "Early diagnosis of Alzheimer's disease based on partial least squares, principal component analysis and support vector machine using segmented MRI images". In: *Neurocomputing* 151 (Mar. 2015), pp. 139–150. ISSN: 0925-2312.  
DOI: [10.1016/j.neucom.2014.09.072](https://doi.org/10.1016/j.neucom.2014.09.072).
- [11] F.J. Martínez-Murcia, A. Ortiz, J. Manuel Górriz, J. Ramírez, and I.A. Illán. "A volumetric radial LBP projection of MRI brain images for the diagnosis of alzheimer's disease". In: *Artificial Computation in Biology and Medicine*. Vol. 9107. Springer Science + Business Media, 2015, pp. 19–28.  
DOI: [10.1007/978-3-319-18914-7\\_3](https://doi.org/10.1007/978-3-319-18914-7_3).
- [12] Minna Sikiö, Kirsi K Holli-Helenius, Lara CV Harrison, Pertti Ryymin, Hanna Ruottinen, Tiia Saunamäki, Hannu J Eskola, Irina Elovaara, and Prasun Dastidar. "MR image texture in Parkinson's disease: a longitudinal study". In: *Acta Radiologica* 56.1 (2015), pp. 97–104.
- [13] A Di Martino et al. "The autism brain imaging data exchange: towards a large-scale evaluation of the intrinsic brain architecture in autism." In: *Molecular psychiatry* 19 (6 June 2014), pp. 659–667. ISSN: 1476-5578.  
DOI: [10.1038/mp.2013.78](https://doi.org/10.1038/mp.2013.78).
- [14] Christine Ecker and Declan Murphy. "Neuroimaging in autism—from basic science to translational research." In: *Nature reviews. Neurology* 10 (2 Feb. 2014), pp. 82–91. ISSN: 1759-4766.  
DOI: [10.1038/nrneurol.2013.276](https://doi.org/10.1038/nrneurol.2013.276).
- [15] Shlomi Haar, Sigal Berman, Marlene Behrmann, and Ilan Dinstein. "Anatomical Abnormalities in Autism?" In: *Cerebral Cortex* (2014).  
DOI: [10.1093/cercor/bhu242](https://doi.org/10.1093/cercor/bhu242).
- [16] F.J. Martínez-Murcia, J.M. Górriz, J. Ramírez, I. Álvarez Illán, D. Salas-González, and F. Segovia. "Projecting MRI brain images for the detection of Alzheimer's Disease". In: *Studies in Health Technology and Informatics*. Vol. 207. 2014, pp. 225–233.  
DOI: [10.3233/978-1-61499-474-9-225](https://doi.org/10.3233/978-1-61499-474-9-225).

- [17] F.J. Martínez-Murcia, J.M. Górriz, J. Ramírez, I.A. Illán, and A. Ortiz. "Automatic detection of Parkinsonism using significance measures and component analysis in DaTSCAN imaging". In: *Neurocomputing* 126 (Feb. 2014), pp. 58–70.  
DOI: [10.1016/j.neucom.2013.01.054](https://doi.org/10.1016/j.neucom.2013.01.054).
- [18] F.J. Martinez-Murcia, J.M. Górriz, J. Ramírez, M. Moreno-Caballero, and M. Gómez-Río. "Parametrization of textural patterns in  $^{123}\text{I}$ -ioflupane imaging for the automatic detection of Parkinsonism". In: *Medical Physics* 41.1 (2014), p. 012502.  
DOI: [10.1118/1.4845115](https://doi.org/10.1118/1.4845115).
- [19] Anderson M Winkler, Gerard R Ridgway, Matthew A Webster, Stephen M Smith, and Thomas E Nichols. "Permutation inference for the general linear model". In: *Neuroimage* 92 (2014), pp. 381–397.
- [20] Katherine S. Button, John P. A. Ioannidis, Claire Mokrysz, Brian A. Nosek, Jonathan Flint, Emma S. J. Robinson, and Marcus R. Munafò. "Power failure: why small sample size undermines the reliability of neuroscience". In: *Nature Reviews Neuroscience* 14.5 (Apr. 2013), pp. 365–376.  
DOI: [10.1038/nrn3475](https://doi.org/10.1038/nrn3475).
- [21] Christine Ecker et al. "Brain surface anatomy in adults with autism: the relationship between surface area, cortical thickness, and autistic symptoms." eng. In: *JAMA Psychiatry* 70.1 (Jan. 2013), pp. 59–70.  
DOI: [10.1001/jamapsychiatry.2013.265](https://doi.org/10.1001/jamapsychiatry.2013.265).
- [22] F.J. Martínez-Murcia, J.M. Górriz, J. Ramírez, I.A. Illán, and C.G. Puntonet. "Texture Features Based Detection of Parkinson's Disease on DaTSCAN Images". In: *Natural and Artificial Computation in Engineering and Medical Applications*. Vol. 7931 LNCS. PART 2. Springer Science + Business Media, 2013, pp. 266–277.  
DOI: [10.1007/978-3-642-38622-0\\_28](https://doi.org/10.1007/978-3-642-38622-0_28).
- [23] F.J. Martínez-Murcia, J.M. Górriz, J. Ramírez, C.G. Puntonet, and I.A. Illán. "Functional activity maps based on significance measures and Independent Component Analysis". In: *Computer Methods and Programs in Biomedicine* 111.1 (July 2013), pp. 255–268.  
DOI: [10.1016/j.cmpb.2013.03.015](https://doi.org/10.1016/j.cmpb.2013.03.015).
- [24] Michela Pievani, Martina Bocchetta, Marina Boccardi, Enrica Cavedo, Matteo Bonetti, Paul M. Thompson, and Giovanni B. Frisoni. "Striatal morphology in early-onset and late-onset Alzheimer's disease: a preliminary study". In: *Neurobiology of Aging* 34.7 (July 2013), pp. 1728–1739.

- ISSN: 0197-4580.  
DOI: [10.1016/j.neurobiolaging.2013.01.016](https://doi.org/10.1016/j.neurobiolaging.2013.01.016).
- [25] A. Rojas, J.M. Górriz, J. Ramírez, I.A. Illán, F.J. Martínez-Murcia, A. Ortiz, M. Gómez Río, and M. Moreno-Caballero. "Application of Empirical Mode Decomposition (EMD) on DaTSCAN SPECT images to explore Parkinson Disease". In: *Expert Systems with Applications* 40.7 (2013), pp. 2756–2766. ISSN: 0957-4174.  
DOI: [10.1016/j.eswa.2012.11.017](https://doi.org/10.1016/j.eswa.2012.11.017). URL: <http://www.sciencedirect.com/science/article/pii/S0957417412012274>.
- [26] Diego Salas-Gonzalez, Juan M Górriz, Javier Ramírez, Ignacio A Illán, and Elmar W Lang. "Linear intensity normalization of FP-CIT SPECT brain images using the  $\alpha$ -stable distribution." In: *NeuroImage* 65 (Jan. 2013), pp. 449–455. ISSN: 1095-9572.  
DOI: [10.1016/j.neuroimage.2012.10.005](https://doi.org/10.1016/j.neuroimage.2012.10.005).
- [27] Fermín Segovia, JM Górriz, Javier Ramírez, Diego Salas-Gonzalez, and Ignacio Álvarez. "Early diagnosis of Alzheimer's disease based on partial least squares and support vector machine". In: *Expert Systems with Applications* 40.2 (2013), pp. 677–683.
- [28] Nikolaus Weiskopf, John Suckling, Guy Williams, Marta Morgado Correia, Becky Inkster, Roger Tait, Cinly Ooi, Edward T Bullmore, and Antoine Lutti. "Quantitative multi-parameter mapping of R<sub>1</sub>, PD\*, MT, and R<sub>2</sub>\* at 3T: a multi-center validation". In: *Frontiers in neuroscience* 7 (2013), p. 95.
- [29] Christine Ecker, John Suckling, Sean C Deoni, Michael V Lombardo, Ed T Bullmore, Simon Baron-Cohen, Marco Catani, Peter Jezzard, Anna Barnes, Anthony J Bailey, et al. "Brain anatomy and its relationship to behavior in adults with autism spectrum disorder: a multicenter magnetic resonance imaging study". In: *Archives of general psychiatry* 69.2 (2012), pp. 195–209.
- [30] I.A.a Illán, J.M.a Górriz, J.a Ramírez, F.a Segovia, J.M.b Jiménez-Hoyuela, and S.J.b Ortega Lozano. "Automatic assistance to Parkinsons disease diagnosis in DaTSCAN SPECT imaging". In: *Medical Physics* 39.10 (2012), pp. 5971–5980.
- [31] F.J. Martínez-Murcia, J.M. Górriz, J. Ramírez, C.G. Puntonet, and D. Salas-González. "Computer Aided Diagnosis tool for Alzheimer's Disease based on Mann-Whitney-Wilcoxon U-Test". In: *Expert Systems with Applications* 39.10 (Aug. 2012), pp. 9676–9685.  
DOI: [10.1016/j.eswa.2012.02.153](https://doi.org/10.1016/j.eswa.2012.02.153).

- [32] Martin Reuter, Nicholas J Schmansky, H Diana Rosas, and Bruce Fischl. "Within-subject template estimation for unbiased longitudinal image analysis." In: *NeuroImage* 61 (4 July 2012), pp. 1402–1418. ISSN: 1095-9572. DOI: [10.1016/j.neuroimage.2012.02.084](https://doi.org/10.1016/j.neuroimage.2012.02.084).
- [33] F. Segovia, J. M. Górriz, J. Ramírez, I. Álvarez, J. M. Jiménez-Hoyuela, and S. J. Ortega. "Improved Parkinsonism diagnosis using a partial least squares based approach". In: *Medical physics* 39.7 (2012), pp. 4395–4403.
- [34] Clive Ballard, Serge Gauthier, Anne Corbett, Carol Brayne, Dag Aarsland, and Emma Jones. "Alzheimer's disease." In: *Lancet (London, England)* 377 (9770 Mar. 2011), pp. 1019–1031. ISSN: 1474-547X. DOI: [10.1016/S0140-6736\(10\)61349-9](https://doi.org/10.1016/S0140-6736(10)61349-9).
- [35] Chih-Chung Chang and Chih-Jen Lin. "LIBSVM: a library for support vector machines". In: *ACM Transactions on Intelligent Systems and Technology* 2.3 (Apr. 2011), pp. 1–27. ISSN: 2157-6904. DOI: [10.1145/1961189.1961199](https://doi.org/10.1145/1961189.1961199).
- [36] J. M. Górriz, F. Segovia, J. Ramírez, A. Lassl, and D. Salas-Gonzalez. "GMM based SPECT image classification for the diagnosis of Alzheimer's disease". In: *Applied Soft Computing* 11.2 (2011), pp. 2313–2325. ISSN: 1568-4946. DOI: [10.1016/j.asoc.2010.08.012](https://doi.org/10.1016/j.asoc.2010.08.012).
- [37] I. A. Illán, J. M. Górriz, J. Ramírez, D. Salas-Gonzalez, M. M. López, F. Segovia, R. Chaves, M. Gómez-Rio, and C. G. Puntonet. "<sup>18</sup>F-FDG PET imaging analysis for computer aided Alzheimer's diagnosis". In: *Information Sciences* 181 (4 Feb. 2011), pp. 903–916. ISSN: 0020-0255. DOI: [10.1016/j.ins.2010.10.027](https://doi.org/10.1016/j.ins.2010.10.027).
- [38] F.J. Martínez, D. Salas-González, J.M. Górriz, J. Ramírez, C.G. Puntonet, and M. Gómez-Río. "Analysis of Spect Brain Images Using Wilcoxon and Relative Entropy Criteria and Quadratic Multivariate Classifiers for the Diagnosis of Alzheimer's Disease". In: *New Challenges on Bioinspired Applications*. Vol. 6687. Lecture Notes in Computer Science PART 2. Springer Science + Business Media, 2011, pp. 41–48. DOI: [10.1007/978-3-642-21326-7\\_5](https://doi.org/10.1007/978-3-642-21326-7_5).
- [39] David J Towey, Peter G Bain, and Kuldip S Nijran. "Automatic classification of <sup>123</sup>I-FP-CIT (DaTSCAN) SPECT images". In: *Nuclear Medicine Communications* 32.8 (Aug. 2011). PMID: 21659911, pp. 699–707. ISSN: 1473-5628. DOI: [10.1097/MNM.0b013e328347cd09](https://doi.org/10.1097/MNM.0b013e328347cd09). URL: <http://www.ncbi.nlm.nih.gov/pubmed/21659911>.

- [40] Yoav Benjamini. "Simultaneous and selective inference: current successes and future challenges". In: *Biometrical Journal* 52.6 (2010), pp. 708–721.
- [41] Matias Bossa, Ernesto Zacur, Salvador Olmos, Alzheimer's Disease Neuroimaging Initiative, et al. "Tensor-based morphometry with stationary velocity field diffeomorphic registration: application to ADNI". In: *NeuroImage* 51.3 (2010), pp. 956–969.
- [42] Michael P. Fay and Michael A. Proschan. "Wilcoxon-Mann-Whitney or t-test? On assumptions for hypothesis tests and multiple interpretations of decision rules". In: *Statistics Surveys* 4 (2010), pp. 1–39.
- [43] Martin Reuter, H Diana Rosas, and Bruce Fischl. "Highly accurate inverse consistent registration: a robust approach." In: *NeuroImage* 53 (4 Dec. 2010), pp. 1181–1196. ISSN: 1095-9572.  
DOI: [10.1016/j.neuroimage.2010.07.020](https://doi.org/10.1016/j.neuroimage.2010.07.020).
- [44] J. M. Górriz, A. Lassl, J. Ramírez, D. Salas-Gonzalez, C. G. Puntonet, and E. W. Lang. "Automatic selection of ROIs in functional imaging using Gaussian mixture models". In: *Neuroscience Letters* 460.2 (2009), pp. 108–111.
- [45] Trevor Hastie, Robert Tibshirani, and Jerome Friedman. "The Elements of Statistical Learning". In: Springer New York, Aug. 26, 2009. Chap. 7. ISBN: 978-0-387-84858-7.
- [46] Gabor T. Herman. "Filtered Backprojection for Parallel Beams". In: *Fundamentals of Computerized Tomography*. Springer, Jan. 2009. ISBN: 978-1-85233-617-2.  
DOI: [10.1007/978-1-84628-723-7\\_8](https://doi.org/10.1007/978-1-84628-723-7_8).
- [47] Chandan Misra, Yong Fan, and Christos Davatzikos. "Baseline and longitudinal patterns of brain atrophy in MCI patients, and their use in prediction of short-term conversion to AD: Results from ADNI". In: *NeuroImage* 44.4 (Feb. 2009), pp. 1415–1422. ISSN: 1053-8119. URL: <http://www.sciencedirect.com/science/article/B6WNP-4TVHSN7-9/2/5cc8f8f25da785653bfcef199a129979>.
- [48] Diego Salas-Gonzalez, Juan M Górriz, Javier Ramírez, Miriam López, Ignacio A Illan, Fermín Segovia, Carlos G Puntonet, and Manuel Gómez-Río. "Analysis of SPECT brain images for the diagnosis of Alzheimer's disease using moments and support vector machines." In: *Neuroscience letters* 461 (1 Sept. 2009), pp. 60–64. ISSN: 1872-7972.  
DOI: [10.1016/j.neulet.2009.05.056](https://doi.org/10.1016/j.neulet.2009.05.056).

- [49] Phoebe G. Spetsieris, Yilong Ma, Vijay Dhawan, and David Eidelberg. "Differential diagnosis of parkinsonian syndromes using functional PCA-based imaging features". In: *Neuroimage* 45.4 (May 2009), pp. 1241–52. ISSN: 1053-8119. URL: <http://www.sciencedirect.com/science/article/B6WNP-4VCH6WN-1/2/fbde9dd344d47cc00f6923a23af3796a>.
- [50] Li Wang, Chunming Li, Quansen Sun, Deshen Xia, and Chiu-Yen Kao. "Active contours driven by local and global intensity fitting energy with application to brain MR image segmentation". In: *Computerized Medical Imaging and Graphics* 33.7 (2009), pp. 520–531.
- [51] H.C. Chen, M. Goldberg, M. Magdon-Ismail, and W.A. Wallace. "Reverse Engineering a Social Agent-Based Hidden Markov Model - ViSAGE". In: *International Journal of Neural Systems* 18.06 (2008), pp. 491–526.
- [52] Milos D Ikonomovic et al. "Post-mortem correlates of in vivo PiB-PET amyloid imaging in a typical case of Alzheimer's disease." In: *Brain : a journal of neurology* 131 (Pt 6 June 2008), pp. 1630–1645. ISSN: 1460-2156. DOI: [10.1093/brain/awn016](https://doi.org/10.1093/brain/awn016).
- [53] Carl Philips, Daniel Li, Daniela Raicu, and Jacob Furst. "Directional Invariance of Co-occurrence Matrices within the Liver". In: *International Conference on Biocomputation, Bioinformatics, and Biomedical Technologies* (2008), pp. 29–34. DOI: [10.1109/BIOTECHNO.2008.24](https://doi.org/10.1109/BIOTECHNO.2008.24).
- [54] GN Srinivasan and G Shobha. "Statistical texture analysis". In: *Proceedings of world academy of science, engineering and technology*. Vol. 36. 2008, pp. 1264–1269.
- [55] Klaus Tatsch. "Extrapyramidal syndromes: PET and SPECT". In: *Diseases of the Brain, Head & Neck, Spine*. Springer, 2008, pp. 234–239.
- [56] Federico De Martino, Francesco Gentile, Fabrizio Esposito, Marco Balsi, Francesco Di Salle, Rainer Goebel, and Elia Formisano. "Classification of fMRI independent components using IC-fingerprints and support vector machine classifiers". In: *Neuroimage* 34.1 (Jan. 2007), pp. 177–194. ISSN: 1053-8119.
- [57] Bruno Dubois et al. "Research criteria for the diagnosis of Alzheimer's disease: revising the NINCDS–ADRDA criteria". In: *The Lancet Neurology* 6.8 (Aug. 2007), pp. 734–746. ISSN: 1474-4422. DOI: [10.1016/s1474-4422\(07\)70178-3](https://doi.org/10.1016/s1474-4422(07)70178-3).

- [58] Thomas Eckert and Christine Edwards. "The application of network mapping in differential diagnosis of parkinsonian disorders". In: *Clinical Neuroscience Research* 6.6 (2007). Neural Networks in the Imaging of Neuropsychiatric Diseases, pp. 359–366. ISSN: 1566-2772.  
DOI: [10.1016/j.cnr.2007.05.001](https://doi.org/10.1016/j.cnr.2007.05.001). URL: <http://www.sciencedirect.com/science/article/pii/S1566277207000023>.
- [59] K.J. Friston, J. Ashburner, S.J. Kiebel, T.E. Nichols, and W.D. Penny. *Statistical Parametric Mapping: The Analysis of Functional Brain Images*. Academic Press, 2007.
- [60] S.J. Ortega Lozano, M.D. Martínez del Valle Torres, J.M. Jiménez-Hoyuela García, A.L. Gutiérrez Cardo, and V. Campos Arillo. "Diagnostic accuracy of FP-CIT SPECT in patients with Parkinsonism". In: *Revista Española de Medicina Nuclear (English Edition)* 26.5 (2007), pp. 277–285. ISSN: 1578-200X.  
DOI: [10.1016/S1578-200X\(07\)70062-1](https://doi.org/10.1016/S1578-200X(07)70062-1). URL: <http://www.sciencedirect.com/science/article/pii/S1578200X07700621>.
- [61] J Puñal Riobóo, L Varela Lema, A Serena Puig, and A Ruano-Ravina. "Effectiveness of  $^{123}\text{I}$ -ioflupane (DaTSCAN) in the diagnosis of Parkinsonian syndromes. A systematic review". In: *Revista Española De Medicina Nuclear* 26.6 (Dec. 2007). PMID: 18021694, pp. 375–384. ISSN: 0212-6982.
- [62] Yvan Saeys, Iñaki Inza, and Pedro Larrañaga. "A review of feature selection techniques in bioinformatics." eng. In: *Bioinformatics* 23.19 (Oct. 2007), pp. 2507–2517.  
DOI: [10.1093/bioinformatics/btm344](https://doi.org/10.1093/bioinformatics/btm344). URL: <http://dx.doi.org/10.1093/bioinformatics/btm344>.
- [63] Guoying Zhao and Matti Pietikainen. "Dynamic Texture Recognition Using Local Binary Patterns with an Application to Facial Expressions". In: *IEEE Transactions on Pattern Analysis and Machine Intelligence* 29.6 (June 2007), pp. 915–928. ISSN: 0162-8828.  
DOI: [10.1109/TPAMI.2007.1110](https://doi.org/10.1109/TPAMI.2007.1110).
- [64] Yun Zhou, Susan M. Resnick, Weiguo Ye, Hong Fan, Daniel P. Holt, William E. Klunk, Chester A. Mathis, Robert Dannals, and Dean F. Wong. "Using a reference tissue model with spatial constraint to quantify  $[^{11}\text{C}]$ Pittsburgh compound B PET for early diagnosis of Alzheimer's disease". In: *Neuroimage* 36.2 (June 2007), pp. 298–312. ISSN: 1053-8119. URL: <http://www.sciencedirect.com/science/article/B6WNP-4N8M886-1/2/de5a061a0cf2d3250bcac48cc4f77be2>.
- [65] John Rice. *Mathematical statistics and data analysis*. Nelson Education, 2006.

- [66] Gary J Kelloff, John M Hoffman, Bruce Johnson, Howard I Scher, Barry A Siegel, Edward Y Cheng, Bruce D Cheson, Joyce O'Shaughnessy, Kathryn Z Guyton, David A Mankoff, et al. "Progress and promise of FDG-PET imaging for cancer patient management and oncologic drug development". In: *Clinical Cancer Research* 11.8 (2005), pp. 2785–2808.
- [67] Christoph Scherfler, Klaus Seppi, Eveline Donnemiller, Georg Goebel, Christian Brenneis, Irene Virgolini, Gregor K Wenning, and Werner Poewe. "Voxel-wise analysis of [<sup>123</sup>I]beta-CIT SPECT differentiates the Parkinson variant of multiple system atrophy from idiopathic Parkinson's disease." In: *Brain* 128 (Pt 7 July 2005), pp. 1605–1612. ISSN: 1460-2156.  
DOI: [10.1093/brain/awh485](https://doi.org/10.1093/brain/awh485).
- [68] Chadwick W. Christine and Michael J. Aminoff. "Clinical differentiation of parkinsonian syndromes: Prognostic and therapeutic relevance". In: *The American Journal of Medicine* 117.6 (2004), pp. 412–419. ISSN: 0002-9343.  
DOI: [10.1016/j.amjmed.2004.03.032](https://doi.org/10.1016/j.amjmed.2004.03.032). URL: <http://www.sciencedirect.com/science/article/pii/S0002934304003626>.
- [69] Stephen M Smith et al. "Advances in functional and structural MR image analysis and implementation as FSL." In: *NeuroImage* 23 Suppl 1 (2004), S208–S219. ISSN: 1053-8119.  
DOI: [10.1016/j.neuroimage.2004.07.051](https://doi.org/10.1016/j.neuroimage.2004.07.051).
- [70] J. Stoeckel, N. Ayache, G. Malandain, P. M. Koulibaly, K. P. Ebmeier, and J. Darcourt. "Automatic Classification of SPECT Images of Alzheimer's Disease Patients and Control Subjects". In: *Medical Image Computing and Computer-Assisted Intervention - MICCAI*. Vol. 3217. Lecture Notes in Computer Science. Springer, 2004, pp. 654–662.
- [71] Rigoberto Pérez de Alejo, Jesús Ruiz-Cabello, Manuel Cortijo, Ignacio Rodriguez, Imanol Echave, Javier Regadera, Juan Arrazola, Pablo Avilés, Pilar Barreiro, Domingo Gargallo, et al. "Computer-assisted enhanced volumetric segmentation magnetic resonance imaging data using a mixture of artificial neural networks". In: *Magnetic resonance imaging* 21.8 (2003), pp. 901–912.
- [72] Walter Daelemans, Véronique Hoste, Fien Meulder, and Bart Naudts. "Combined Optimization of Feature Selection and Algorithm Parameters in Machine Learning of Language". In: *Machine Learning: ECML 2003* (Jan. 1, 2003).  
DOI: [10.1007/978-3-540-39857-8\\_10](https://doi.org/10.1007/978-3-540-39857-8_10). URL: [http://dx.doi.org/10.1007/978-3-540-39857-8\\_10](http://dx.doi.org/10.1007/978-3-540-39857-8_10).

- [73] Peter Dixon. "The p-value fallacy and how to avoid it." In: *Canadian journal of experimental psychology = Revue canadienne de psychologie expérimentale* 57 (3 Sept. 2003), pp. 189–202. ISSN: 1196-1961.
- [74] I. Guyon and A. Elisseeff. "An Introduction to Variable and Feature Selection". In: *Journal of Machine Learning Research* 3 (2003), pp. 1157–1182.
- [75] Aapo Hyvärinen and Yutaka Kano. "Independent component analysis for non-normal factor analysis". In: *New developments in psychometrics*. Springer, 2003, pp. 649–656.
- [76] A Winogrodzka, P Bergmans, J Booij, E A van Royen, J C Stoof, and E C Wolters. "[<sup>123</sup>I]beta-CIT SPECT is a useful method for monitoring dopaminergic degeneration in early stage Parkinson's disease". In: *Journal of Neurology, Neurosurgery & Psychiatry* 74.3 (2003), pp. 294–298.  
DOI: [10.1136/jnnp.74.3.294](https://doi.org/10.1136/jnnp.74.3.294).
- [77] David A Clausi. "An analysis of co-occurrence texture statistics as a function of grey level quantization". In: *Canadian Journal of remote sensing* 28.1 (2002), pp. 45–62.
- [78] Bruce Fischl et al. "Whole brain segmentation: automated labeling of neuroanatomical structures in the human brain." In: *Neuron* 33 (3 Jan. 2002), pp. 341–355. ISSN: 0896-6273.
- [79] Andrew Newberg, Abass Alavi, and Martin Reivich. "Determination of regional cerebral function with FDG-PET imaging in neuropsychiatric disorders". In: *Seminars in nuclear medicine*. Vol. 32. 1. Elsevier. 2002, pp. 13–34.
- [80] N Saeed and BK Puri. "Cerebellum segmentation employing texture properties and knowledge based image processing: applied to normal adult controls and patients". In: *Magnetic resonance imaging* 20.5 (2002), pp. 425–429.
- [81] Marti J Anderson and John Robinson. "Permutation tests for linear models". In: *Australian & New Zealand Journal of Statistics* 43.1 (2001), pp. 75–88.
- [82] J. C. Baron, G. Chételat, B. Desgranges, G. Perchey, B. Landeau, V. de la Sayette, and F. Eustache. "In vivo mapping of gray matter loss with voxel-based morphometry in mild Alzheimer's disease." eng. In: *Neuroimage* 14.2 (Aug. 2001), pp. 298–309.  
DOI: [10.1006/nimg.2001.0848](https://doi.org/10.1006/nimg.2001.0848).

- [83] M Jenkinson and S Smith. "A global optimisation method for robust affine registration of brain images." In: *Medical image analysis* 5 (2 June 2001), pp. 143–156. ISSN: 1361-8415.
- [84] Vassili A Kovalev, Frithjof Kruggel, H-J Gertz, and D Yves von Cramon. "Three-dimensional texture analysis of MRI brain datasets". In: *Medical Imaging, IEEE Transactions on* 20.5 (2001), pp. 424–433.
- [85] J Mazziotta et al. "A probabilistic atlas and reference system for the human brain: International Consortium for Brain Mapping (ICBM)." In: *Philosophical Transactions of the Royal Society of London. Series B, Biological Sciences* 356 (1412 Aug. 2001), pp. 1293–1322. ISSN: 0962-8436.  
DOI: [10.1098/rstb.2001.0915](https://doi.org/10.1098/rstb.2001.0915).
- [86] John Ashburner and Karl J Friston. "Voxel-based morphometry—the methods". In: *Neuroimage* 11.6 (2000), pp. 805–821.
- [87] R. P. W. Duin. "Classifiers in almost empty spaces". In: *Proceedings of the 15th International Pattern Recognition Conference*. Vol. 2. 2000, pp. 1–7.  
DOI: [10.1109/ICPR.2000.906006](https://doi.org/10.1109/ICPR.2000.906006).
- [88] A. Hyvärinen and E. Oja. "Independent component analysis: algorithms and applications". In: *Neural Networks* 13.4-5 (2000), pp. 411–430. ISSN: 0893-6080.  
DOI: [10.1016/S0893-6080\(00\)00026-5](https://doi.org/10.1016/S0893-6080(00)00026-5).
- [89] D. Kogure, H. Matsuda, T. Ohnishi, T. Asada, M. Uno, T. Kunihiro, S. Nakano, and M. Takasaki. "Longitudinal Evaluation of Early Alzheimer Disease Using Brain Perfusion SPECT". In: *The Journal of Nuclear Medicine* 41.7 (2000), pp. 1155–1162. URL: <http://jnm.snmjournals.org/cgi/content/abstract/41/7/1155>.
- [90] A M Dale, B Fischl, and M I Sereno. "Cortical surface-based analysis. I. Segmentation and surface reconstruction." In: *NeuroImage* 9 (2 Feb. 1999), pp. 179–194. ISSN: 1053-8119.  
DOI: [10.1006/nimg.1998.0395](https://doi.org/10.1006/nimg.1998.0395).
- [91] A. Hyvärinen. "Fast and Robust Fixed-Point Algorithms for Independent Component Analysis". In: *IEEE Transactions on Neural Networks* 10.3 (1999), pp. 626–634.
- [92] L-K Soh and Costas Tsatsoulis. "Texture analysis of SAR sea ice imagery using gray level co-occurrence matrices". In: *Geoscience and Remote Sensing, IEEE Transactions on* 37.2 (1999), pp. 780–795.

- [93] P Szatmari. "Heterogeneity and the genetics of autism." In: *Journal of psychiatry & neuroscience : JPN* 24 (2 Mar. 1999), pp. 159–165. ISSN: 1180-4882.
- [94] Sergios Theodoridis and Konstantinos Koutroumbas. *Pattern Recognition*. New York: Academic Press, 1999. ISBN: 9781597492720.
- [95] Andrew P Bradley. "The use of the area under the ROC curve in the evaluation of machine learning algorithms". In: *Pattern recognition* 30.7 (1997), pp. 1145–1159.
- [96] A. Hyvärinen and E. Oja. "A fast fixed-point algorithm for independent component analysis". In: *Neural Computation* 9 (1997), pp. 1483–1492.
- [97] Vladimir Vapnik, Steven E Golowich, Alex Smola, et al. "Support vector method for function approximation, regression estimation, and signal processing". In: *Advances in neural information processing systems* (1997), pp. 281–287.
- [98] S Arndt, T Cizadlo, D O'Leary, S Gold, and N C Andreasen. "Normalizing counts and cerebral blood flow intensity in functional imaging studies of the human brain." In: *NeuroImage* 3 (3 Pt 1 June 1996), pp. 175–184. ISSN: 1053-8119.  
DOI: [10.1006/nimg.1996.0019](https://doi.org/10.1006/nimg.1996.0019).
- [99] Timo Ojala, Matti Pietikäinen, and David Harwood. "A comparative study of texture measures with classification based on featured distributions". In: *Pattern Recognition* 29.1 (Jan. 1996), pp. 51–59. ISSN: 00313203.  
DOI: [10.1016/0031-3203\(95\)00067-4](https://doi.org/10.1016/0031-3203(95)00067-4).
- [100] Yoav Benjamini and Yosef Hochberg. "Controlling the false discovery rate: a practical and powerful approach to multiple testing". In: *Journal of the royal statistical society. Series B (Methodological)* (1995), pp. 289–300.
- [101] R Kohavi. "A study of cross-validation and bootstrap for accuracy estimation and model selection." In: *Proceedings of International Joint Conference on AI*. 1995, pp. 1137–1145. URL: <http://citeseer.ist.psu.edu/kohavi95study.html>.
- [102] Juliet Popper Shaffer. "Multiple hypothesis testing". In: *Annual review of psychology* 46.1 (1995), pp. 561–584.
- [103] J. J. Claus, F. van Harskamp, M. M. B. Breteler, E. P. Krenning, I. de Koning abd J. M. van der Cammen, A. Hofman, and D. Hasan. "The diagnostic value of SPECT with Tc 99m HMPAO in Alzheimer's disease. A population-based study". In: *Neurology* 44.3 (1994), pp. 454–461.  
DOI: [10.1159/000051283](https://doi.org/10.1159/000051283).

- [104] Karl J Friston, Andrew P Holmes, Keith J Worsley, J-P Poline, Chris D Frith, and Richard SJ Frackowiak. "Statistical parametric maps in functional imaging: a general linear approach". In: *Human brain mapping* 2.4 (1994), pp. 189–210.
- [105] RM Haralick and LG Shapiro. *Robot and Computer Vision (vols. 1 and 2)*. 1992.
- [106] J Talairach and P Tournoux. *Co-Planar Stereotactic Atlas of the Human Brain*. 1988.
- [107] M J de Leon, S H Ferris, A E George, B Reisberg, D R Christman, I I Kricheff, and A P Wolf. "Computed tomography and positron emission transaxial tomography evaluations of normal aging and Alzheimer's disease". In: *Journal of Cerebral Blood Flow and Metabolism: Official Journal of the International Society of Cerebral Blood Flow and Metabolism* 3.3 (Sept. 1983). PMID: 6603463, pp. 391–4.
- [108] "Handbook of Statistics". In: ed. by R. R. Krishnaiah and L. N. Kanal. North-Holland, 1982. Chap. Dimensionality and sample size considerations in pattern recognition practice, pp. 825–855.
- [109] R. Haralick, K. Shanmugam, and I. Dinstein. "Textural features for image classification". In: *IEEE Transactions on Systems, Man and Cybernetics* 3.6 (1973), pp. 610–621.